Theoretical analysis, design and fabrication of nano-opto-mechanical systems (NOMS)

Yefeng Yu

UNIVERSITÉ PARIS-EST

Ecole Doctorale

Mathématiques, Sciences de l'Information et de la Communication (MSTIC)

THÈSE

pour obtenir le grade de

Docteur de l'Université Paris-Est

Spécialité : Electronique, Optronique et Systèmes

présentée et soutenue publiquement par

Yefeng YU

le 18 novembre 2011

Analyse théorique, Conception et Réalisation De Systèmes Nano-Opto-Mécaniques

Theoretical Analysis, Design and Fabrication of Nano-Opto-Mechanical System (NOMS)

Directeurs de thèse

Tarik BOUROUINA et Ai-Qun LIU

Jury

Franck CHOLLET, Professeur, Université de Franche-Comté CNRS FEMTO	Rapporteur
Abderrahim RAMDANE, Directeur de Recherche, LPN CNRS	Rapporteur
Anne-Laure BILLABERT, Maître de Conférences, CNAM	Examinateur
Elodie RICHALOT, Maître de Conférences, UPEMLV	Examinateur
Tarik BOUROUINA, Professeur, ESIEE Paris	Examinateur
Ai-Qun LIU, Professeur, Nanyang Technological University, Singapour	Examinateur

Première Partie

RÉSUMÉ LONG

Résumé Long

Dans cette thèse, un système nano-opto-mécanique (*Nano Opto Mechanical System* –NOMS) est exploré et deux dispositifs nano-opto-mécaniques sont conçus, analysés, simulés et réalisés. Tout d'abord, un générateur de moment cinétique (*Angular Moment Generator* –AMG) constitué d'un résonateur en anneau, d'un guide d'onde et d'un groupe de nano-plots est conçu, analysé théoriquement et simulé. L'analyse théorique et les résultats numériques montrent qu'une série de champs optiques tournants (*Rotating Optical Field* –ROF) sont générés lorsque différentes longueurs d'onde de résonance sont couplées dans le générateur. Par la suite, la force optique, le potentiel optique et le couple optique du ROF généré sont analysés théoriquement, simulés numériquement et discutés. La distribution de la force optique est influencée par le ROF avec différents ordres angulaires et différents objets. Les couples optiques sont analysés et discutés pour différents nano-objets, c'est-à-dire une nano-particule sphérique, un nano-fil et un nano-rotor. Enfin, un système accordable de transparence induite par résonateurs couplés (*Coupled-Resonator-Induced Transparency* –CRIT), qui est contrôlé par la force optique entre le résonateur en anneau et le substrat, est conçu, analysé théoriquement, simulé, fabriqué et testé. Le système CRIT accordable se compose d'un guide d'onde et de deux résonateurs en anneaux couplés, parmi lesquels l'un est libre de se mouvoir tandis que l'autre est fixe. Différentes puissances d'entrée produisent différentes forces optiques sur l'anneau libre, ce qui produit à la fin différentes déformations, changeant ainsi le champ optique résultant, induisant également un décalage du spectre de transmission ainsi qu'une variation du retard de groupe.

Cette thèse est divisée en six chapitres:

Le premier chapitre est l'introduction incluant l'exposé des motifs, l'objectif, les contributions majeures ainsi que l'organisation de la thèse. Une première section relative aux motivations explique les raisons ayant conduit à la réalisation de cette thèse. La section suivante explique les objectifs visés. Enfin, la dernière section liste nos principales contributions, innovations et découvertes.

Le chapitre deux donne une revue de l'état de l'art sur le résonateur optique en anneau, le moment cinétique optique, la force optique et le système CRIT. Ce chapitre présente les bases physiques nécessaires à l'étude du résonateur optique en anneau et du système CRIT. Il clarifie également les concepts de base du moment cinétique optique et de la force optique, et illustre les applications correspondantes.

Le troisième chapitre présente les principes de fonctionnement de l'AMG conçu, illustre les distributions typiques du champ optique, discute de l'efficacité de génération et les effets des nano-plot pour la génération de moment cinétique. Le § 3.1 donne l'analyse théorique qui comprend la conception, les propriétés d'un anneau seul, les effets des nano-plots sur couplage de la lumière ainsi que la génération du moment cinétique. Le § 3.2 illustre les résultats numériques sur les effets des nano-plots sur le couplage de la lumière et sur la génération de moment cinétique. Le § 3.3 traite de l'efficacité de génération, les effets des nano-plot sur la génération et la distribution 3D du champ optique. Le § 3.4 résume ce chapitre.

Le chapitre quatre traite de la force optique, du potentiel optique et du couple des champs optique tournants (ROFs) générés, pour le piégeage et la rotation de nano-particules. Le § 4.1 donne une analyse théorique des distributions de la force optique, du

potentiel optique et du couple. Le § 4.2 présente les résultats numériques sur les distributions de la force optique, du potentiel optique et du couple. Les effets de nano-rotor et d'ordre angulaire sur la distribution de la force optique ainsi que les effets de différents nano-objets (nano-particules, nano-fils ou nano-rotor) sur les couples optiques sont également discutés. Le § 4.3 résume ce chapitre.

Le chapitre cinq démontre la faisabilité d'un système CRIT accordable entraîné par la force optique entre un anneau libéré et le substrat. Le § 5.1 présente l'analyse théorique du système de CRIT accordable. Il comprend la conception, les propriétés du CRIT basé sur des résonateurs en anneau, la force optique entre un anneau libéré et le substrat, la détermination d'un point stable et le ratio d'accordabilité. Le § 5.2 montre les résultats numériques et les discussions sur le système CRIT accordable. Il comprend les calculs de l'indice de réfraction effectif, le facteur d'atténuation, le coefficient de couplage, la naissance du champ optique, la transmitivité, le retard de groupe, la détermination du point stable, le ratio d'accordabilité et la plage d'accord. Le § 5.3 illustre les procédés de fabrication en vue de la réalisation du système CRIT accordable. Le § 5.4 donne les résultats expérimentaux ainsi que leur discussion et enfin, le § 5.5 résume ce chapitre.

Le chapitre six présente les conclusions de cette thèse ainsi que plusieurs recommandations pour les travaux futurs.

Chapitre un: Introduction

La principale motivation de cette thèse est d'étudier des NOMS (*Nano Opto Mechanical Systems*) et apporter une percée majeure dans ce domaine interdisciplinaire. Augmenter l'intégrabilité d'un nano-rotor constitue une première motivation de cette thèse. Explorer les propriétés optiques et mécaniques d'un système accordable CRIT (*Coupled-Resonator-Induced Transparency)* –à base de résonateurs en anneau, constitue l'autre motivation de cette thèse.

L'objectif principal de cette thèse est de clarifier les concepts de base, effectuer des analyses théoriques et d'obtenir les résultats numériques sur la force optique, le moment cinétique optique et le système CRIT accordable. Sur la base de la force optique, deux dispositifs NOMS ont du être développés pour des applications différentes. Le premier dispositif est conçu pour générer une ROF pour le piégeage des nanoparticules et produire leur rotation. Le deuxième dispositif est un système CRIT accordable, qui est conçu pour modifier la distribution du champ optique, le décalage du spectre de transmission et pour faire varier le retard de groupe.

La première contribution de cette thèse est la conception, l'analyse et la simulation d'un AMG pour la génération de ROFs. Tous les ROFs générés présentent des moments cinétiques (angulaires) mais pas de moments linéaires le long de l'axe de rotation, ce qui offre la possibilité d'obtenir un nano-rotor avec auto-alignement et une bonne intégrabilité. La deuxième contribution est l'analyse et la simulation de la distribution de la force optique, des potentiels optiques ainsi que les couples optiques. Sur la base des résultats numériques, les comportements d'une nanoparticule, d'un nanofil, ou d'un nanorotor peuvent être prédits. Enfin, l'organisation de cette thèse est introduite.

Chapitre deux: étude bibliographique

Dans ce chapitre, les concepts de base du résonateur optique en anneau, le moment cinétique optique, la force optique et le système CRIT sont présentés et discutés. Dans la première section, la cavité optique est introduite, suivie par les concepts de base et les applications du résonateur optique en anneau. Dans la deuxième section, la génération, les caractéristiques et les applications de la force optique sont présentés et discutés. Dans la troisième section, les concepts de base et les méthodes de génération du moment cinétique optique sont introduits. Dans la dernière section, les concepts de base et les applications du système CRIT sont présentés et discutés.

Le résonateur en anneau optique est une cavité optique spéciale, qui consiste en un guide d'ondes en boucle fermée avec un guide supplémentaire ou plus, de type guide bus, couplé(s) à cette boucle. C'est le cas le plus simple parmi toutes les sortes de WGCs, et ses modes ne sont décrits que par l'ordre modal *n*. Dans les résonateurs en anneau, les nœuds de l'onde stationnaire ne sont pas fixes à certains endroits de l'espace, mais décalés d'un endroit à l'autre de façon continue. Le circuit du résonateur optique en anneau présente d'importants facteurs de qualité Q (10^3 ~ 10^6), une bonne intégrabilité et résulte de procédés de fabrication matures. Par conséquent, il est largement utilisé en tant que filtre optique à fine largeur de raie, laser à seuil bas, modulateur de phase sensible, commutateur optique, canal de propagation optique lente et enfin de stockage optique.

Les forces optiques, y compris la force de pression de radiation optique et la force de gradient de champ optique résultent de la force de Lorentz. Le changement de la quantité de mouvement optique et le gradient d'intensité conduisent à la génération de la force de pression de radiation optique et à la force de gradient optique, respectivement.

Un champ évanescent peut également être utilisé pour la génération de forces de gradient optique. Les forces optiques sont très petites (10^{-12} ~ 10^{-7} N); elles ne peuvent pas être utilisées dans les systèmes mécaniques traditionnels, mais applicables dans des systèmes micro- ou nano-mécanique. La force de gradient optique est limitée par la distance alors que la force de radiation ne l'est pas. En combinant la force de gradient et la force de radiation, le transport de particules peut être obtenu sur des distances allant de quelques micromètres jusqu'à 1 mètre.

Un champ optique s'accompagne d'une quantité de mouvement ainsi que d'un moment cinétique. La pression de radiation est causée par le transfert de quantité de mouvement du champ optique à un objet, et la rotation optique est causée par le transfert de moment cinétique du champ optique à un objet. Un faisceau de lumière polarisée circulairement porte un moment cinétique de spin, et un faisceau laser de mode LG d'ordre élevé porte un moment cinétique orbital. Un faisceau Bessel ou HG d'ordre élevé, porte également le moment cinétique orbital. Il existe plusieurs méthodes pour produire un faisceau LG d'ordre élevé, qui comprennent la méthode *"spiral phaseplate"*, la méthode par élément diffractif en phase binaire et la méthode de la SLM. Un faisceau LG d'ordre élevé portant donc un moment cinétique orbital peut être utilisé dans de nombreux domaines, notamment le piégeage d'atomes et la rotation des particules.

La transparence induite par résonateur couplé (CRIT) est le phénomène qui se manifeste dans un système de résonateurs optiques couplés, qui est analogue à la transparence induite électromagnétiquement (EIT) dans les systèmes atomiques. Il n'y a qu'un seul faisceau d'entrée de lumière dans le système CRIT, alors que dans le système de l'IET, il y a un autre faisceau de commande en plus de la sonde de lumière. Le trajet

multiple de la lumière introduit une dégénérescence de mode dans le système CRIT. Les CRIT attirent l'attention de plusieurs chercheurs en raison de ses caractéristiques remarquables, comme la propagation extrêmement lente de la lumière, de transmission à fort taux d'extinction et une sensibilité du spectre de sortie. Il existe plusieurs méthodes pour accorder le système CRIT, qui comprennent la méthode optique non linéaire, la méthode de jonctions P.I.N., etc.

Chapitre trois: générateur optique de moment cinétique

Dans ce chapitre, un générateur de moment cinétique (AMG) utilisant un résonateur en anneau entouré par un ensemble de nano-plots est proposé. Les champs évanescents de la lumière circulant dans le résonateur en anneau sont diffusés par les nano-plots et génèrent un champ optique tournant (ROF), qui porte un moment cinétique orbital. Tout d'abord, le modèle théorique de l'AMG est analysé. Ensuite, les résultats numériques sont illustrés. Enfin, les rendements de production, les effets des nano-plots ainsi que les distributions 3D de champs sont discutés.

Le § 3.1 donne l'analyse théorique qui comprend la conception, les propriétés d'un anneau seul, les effets des nano-plots pour couplage de la lumière et la génération du moment cinétique. L'architecture comprend un résonateur optique en anneau entouré d'un ensemble de nano-plots circulairement périodiques, et un coupleur anneau-guide. La lumière qui traverse l'AMG provoque deux effets. Tout d'abord, la lumière injectée à partir du guide d'onde est couplée dans le résonateur en anneau à travers le champ évanescent. Lorsque la longueur d'onde de la lumière d'entrée coïncide avec celle du mode de résonance de l'anneau, le champ circulant dans l'anneau est renforcé et le champ en sortie du guide d'onde est diminué de manière spectaculaire. Deuxièmement, l'onde évanescente de la lumière confinée dans l'anneau est diffusée par les nano-plots disposés à proximité de ce dernier; les ondes diffusées constituent à nouveau un champ optique à l'intérieur de l'anneau. La circulation de la lumière diffusée dans l'anneau produit une rotation du champ optique.

Pour simplifier l'analyse de l'AMG, l'analyse théorique est divisée en trois sections. Dans le § 3.1.1, les réponses de phase de l'intensité de circulation, de

transmission, et la différence de phase par rapport au résonateur en anneau seul sont discutés. Lorsque la phase totale recueillie sur l'anneau est égal à $2m\pi$, le résonateur en anneau seul a les maxima locaux de circulation d'intensité, et les transmissions minimales. Dans le § 3.1.2, les effets des nano-plots sur le coefficient de couplage de la lumière et sur le facteur d'atténuation du champ sont analysés. Les nano-plots affectent le coefficient de couplage anneau-guide, et de diminuent le facteur d'atténuation du champ sur l'anneau Dans le § 3.1.3, la génération du moment cinétique dans l'anneau est présenté. Lorsque la différence entre l'ordre n des modes de gallerie (WGM) et le numéro N du nano-plot est égal à l, les ondes évanescentes aux positions de deux nano-plots voisins arbitraires ont une différence de phase de $2l\pi/N$, ce qui entraîne une symétrie de rotation d'ordre l pour la distribution du champ optique à l'intérieur le résonateur en anneau. Cette distribution a la même forme que le mode WGM d'ordre l (angulaire), dans le plan perpendiculaire à la direction de propagation du faisceau. Il a également la fréquence de rotation f_r, qui est égale à la fréquence de la lumière f divisé par l'ordre l (i.e. $f_r = \frac{f}{l}$). Par conséquent, le domaine optique correspondant est appelé l'ordre de rotation du champ optique tournant (*Rotating Optical Field* –ROF). Le ROF n'a pas la quantité de mouvement, mais seulement un moment cinétique selon l'axe de rotation.

Le § 3.2 illustre les résultats numériques des effets des nano-plot dans le couplage de la lumière et la génération de moment cinétique. Dans le § 3.2.1, les effets des nano-plots sur le couplage de la lumière et l'intensité de circulation sont discutés. En comparaison avec le coupleur exempt de nano-plots, le coupleur anneau-guide avec un nano-plot a un coefficient de couplage plus important. Lorsque le rayon des nano-plots est augmenté, le l'intensité de circulation relative est diminuée. Lorsque le nano-plot est

approché du guide d'ondes, le champ de circulation relatif est augmenté. Dans le § 3.2.2, les résultats numériques du 1er au 4ème ordres sont illustrés pour les ROF, montrant un très bon accord avec les résultats théoriques. La relation entre les fréquences de rotation ($f_r = \frac{f}{l}$) est également vérifiée par les résultats de simulations à différentes échelles de temps. Les résultats numériques montrent également que les sens de rotation est opposée au sens de circulation de la lumière lorsque $n < N$, alors qu'ils ont le même sens lorsque $n > N$.

Le § 3.3 traite de l'efficacité de la génération, les effets des nano-plots sur la génération et la distribution 3D du champ optique. Dans le § 3.3.1, l'efficacité de la production de ROF par l'AMG est discutée. L'efficacité de la production de ROF d'ordre l est la même que l'intensité maximale des champs optiques d'ordre l. Lorsque la longueur d'onde diminue, l'intensité du champ évanescent au voisinage du résonateur optique en anneau est diminuée. Ceci réduit l'amplitude de la lumière diffusée ainsi que l'efficacité de la production. Lorsque la longueur d'onde augmente, le facteur d'atténuation de champ sur le résonateur optique en anneau est diminué. Ceci réduit l'intensité de la lumière de circulation, l'amplitude du champ évanescent, la lumière diffusée ainsi que l'efficacité de la production. Par conséquent, la longueur d'onde doit être dans la gamme appropriée de l'efficacité de production élevée. Cette gamme est déterminée par l'indice de réfraction, l'écart nano-plot - anneau et le nombre de nano-plots. Dans le § 3.3.2, les effets des nano-plot pour la génération de ROF sont discutés. Lorsque l'indice de réfraction de l'anneau est de 1,6 et N va de 24 à 37, l'efficacité de la production tend à augmenter, alors que lorsque N > 37, l'efficacité de la production tend à diminuer. Lorsque l'indice de réfraction de l'anneau est de 2,6 et 3,476, cette tendance est modifiée à N = 28 et 24, respectivement. Dans le § 3.3.2, la distribution du champ

optique 3D de la ROF générée est brièvement discutée. Puisque les structures de l'AMG sont symétriques par rapport au plan horizontal, la distribution du champ optique est également symétrique par rapport à ce plan.

Chapitre quatre: Force optique, potentiel et couple pour le piégeage et la rotation des nanoparticules

Dans ce chapitre, la distribution de la force optique, le potentiel optique, et le couple optique de ROF générés sont tout d'abord calculés en utilisant le tenseur des contraintes de Maxwell. Ensuite, les résultats numériques correspondants ont illustrés. Enfin, les effets des différentes formes des nano-objets (par exemple des nanoparticules, nanofils, et nanorotor) ainsi que les effets de l'ordre angulaire sont évalués par le calcul et discutés.

Le § 4.1 donne une analyse théorique des distributions de la force optiques, le potentiel optique et le couple optique. L'analyse théorique de la distribution de la force optique et du couple optique sur le nano-rotor, ainsi que le potentiel optique sont présentés dans cette section. Dans le § 4.1.1, la force optique sur une unité de volume avec la distribution de charge inconnue est établie d'après la force de Lorenz et l'équation de Maxwell, et elle comprend deux termes. Le premier terme est représenté par la divergence du tenseur des contraintes de Maxwell, et le second terme traduit la variation de flux d'énergie, qui peut être représentée par la dérivée temporelle du vecteur de Poynting. La force totale optique sur une cible est égale à l'intégration des forces optiques. Dans le § 4.1.2, la notion de potentiel optique est introduite pour le piégeage des particules. Une nano-particule à un point arbitraire dans le ROF correspond à une force d'optique et l'ensemble des forces optiques en tout point forment un champ de forces. Aux nano-particules dans ce champ de force est associée une énergie potentielle, qui est nommée "potentiel optique". Le travail accompli par la force optique est égal à la variation d'énergie potentielle. Les nano-particules sont conduites par la force optique à

des minima locaux dans le potentiel optique, et s'arrêtent à ces points minima locaux ou oscillent autour de ces points.

Le gradient de potentiel autour de ces minima locaux détermine la capacité de piégeage de la ROF. Dans le § 4.1.3, la notion du couple optique est introduite pour la rotation des particules. Le couple optique est égal au produit vectoriel du vecteur déplacement et du vecteur de la force optique. Il est généralement dépendant du temps parce que la force optique est dépendante du temps. Lorsque le rotor est un cylindre et dont l'axe est le même que l'axe de rotation de la ROF généré, le couple total devient indépendant du temps en raison de la symétrie de rotation de la ROF.

Le § 4.2 présente les résultats numériques des distributions de la force optique, du potentiel optique et du couple optique. Les effets de l'ordre angulaire de nano-rotor et sur la distribution de la force optique ainsi que les effets de différents objets (nano-particules, nano-fils ou nano-rotor) sur les couples optiques sont également discutés.

Dans le § 4.2.1, les distributions de la force optique des ROF générés sont présentées. Premièrement, les distributions de champ électrique et les distributions de champ magnétique de la ROF générés d'ordre l sont illustrés dans les détails quand la lumière incidente est en mode TE. La ROF d'ordre l peut être caractérisée par E_x, E_z et H_y. Ensuite, les distributions du vecteur de Poynting de la ROF d'ordre l sont obtenues. Le vecteur de Poynting (ie. flux d'énergie ou intensité optique) a des valeurs plus élevées dans un cylindre qui a un rayon de 200 nm et a un axe tel que l'axe y que dans d'autres configurations. Troisièmement, les distributions de la force optique de la ROF d'ordre l sont illustrées et discutées. Le premier terme (divergence du tenseur des contraintes de Maxwell) de la force optique est 6 ordres de grandeur plus élevé que le second terme (la

dérivée temporelle du vecteur de Poynting). Les effets du nano-rotor sur la distribution de la force optique sont discutés dans le § 4.2.1.1. En comparant la ROF avec le nano-rotor à la ROF sans nano-rotor, les valeurs maximales des E_x, H_y, E_z et S_T sont augmentées, l'espace entre deux maxima voisins radiaux de E_x, H_y and E_z est réduit, le gradient de E_x, H_y, E_z et S_T le long de l'axe y est augmenté, et le rayon du cylindre, pour lequel le vecteur de Poynting (flux d'énergie ou intensité optique) a les plus grandes valeurs, est passé de 200 nm à 180 nm. Le champ de force optique a une variation similaire.

Les effets de l'ordre angulaire pour les distributions de la force optique sont discutés dans le § 4.2.1.2. Lorsque l'ordre angulaire l est augmenté, la zone centrale sans champ optique est élargie. Les courbes d'iso-amplitude de la distribution d'amplitude du champ optique dans le plan horizontal constituent une série de cercles concentriques où les distributions du champ optique ne varient pas en fonction du temps dans une période de rotation. Les ROF d'ordres 1 et 3 sont stables dans le temps.

Toutefois, le ROF d'ordre 2 est fonction du temps en raison de l'effet de rétrodiffusion. La force résultante est introduite pour la discussion. Lorsque l est augmenté de 0 à 3, la force résultante maximale dans le plan horizontal passe de 6.2×10^6 $pNW^{-1}\mu m^{-3}$ à 3.8×10^6 $pNW^{-1}\mu m^{-3}$.

Dans le § 4.2.2, les potentiels optiques sont illustrés. Le potentiel optique est calculé sur la base de la force résultante. Le potentiel optique minimum a la plus petite valeur à $l = 0$, c'est à dire le domaine optique correspondant a une capacité plus élevée de piégeage de particules. En outre, des particules seront piégées sur un cercle de rayon 213

nm pour l = 0, 181 nm pour l = 1, 358 nm pour l = 2 et 380 nm pour l = 3, qui sont les mêmes positions que les régions à plus forte intensité de la lumière.

Dans le § 4.2.3, le couple optique est discuté en fonction de l'objet. Tout d'abord, le couple optique sur une nano-particules est analysé dans § 4.2.3.1. Lorsque l = 0, le champ optique ne tourne pas, donc, une nanoparticule à l'intérieur du champ ne peut pas avoir de couple optique ni de rotation. Lorsque l = 1, le couple optiques entraine la nano-particule dans un mouvement de rotation dans le sens horaire, à l'intérieur d'un cercle de rayon allant de 0 à 220 nm, et en sens anti-horaire si le rayon est compris entre 220 à 440 nm. Puis, le couple optique sur un nano-fil est présenté dans le § 4.2.3.2. Lorsque l = 1, le couple optique, se traduit par une rotation dans le sens horaire lorsque la moitié de sa longueur est comprise entre 0 nm et 300 nm ou entre 560 nm et 600 nm et dans le sens anti-horaire dans l'intervalle entre 300 nm et 560 nm. Lorsque le nano-fil a une longueur de 880 nm, le nano-fil est entraîné avec la plus grande efficacité. Enfin, le couple optique sur un nano-rotor est discuté en § 4.2.3.3.

Lorsque l = 1 et que le rayon est d'environ 0,44 µm, il y a un maximum de couple optique total. Lorsque le nano-rotor conçu a un rayon de 0,5 um, la ROF d'ordre 3 a la plus haute efficacité d'entraînement. Toutefois, la ROF d'ordre 3 devient inefficace pour entraîner un petit nano-rotor dont le rayon est inférieur à 0,3 um. Mais pour le ROF d'ordre 1, le rayon de seuil est abaissé à 0,1 um. Le ROF d'ordre 2 a une capacité d'entraînement entre les ROF ordre 1 et 3.

Chapitre cinq: La force optique comme moyen d'accord de la transparence induite par résonteurs couplés (Coupled-Resonator-Induced Transparency –CRIT)

Dans ce chapitre, un système accordable au moyen de la force optique de la transparence induite par résonateurs couplés (CRIT) est conçu, fabriqué et démontré. Il se compose d'un guide d'onde et de deux résonateurs en anneaux couplés, dans lesquels un anneau est libéré et maintenu par des rayons et un piédestal. Les différentes puissances d'entrée produisent différentes forces optiques, qui correspondent à différentes accumulations de champ optique, différentes décalages du spectre d'émission et différents retards. Tout d'abord, l'analyse théorique du CRIT accordable est discutée. Ensuite, les résultats de la simulation numérique sont illustrés. Par la suite, les procédés de fabrication nanophotonique sont développés. Enfin, les résultats expérimentaux sont discutés.

Le § 5.1 présente l'analyse théorique du système de CRIT accordable. Tout d'abord, la conception du système CRIT accordable est présentée au § 5.1.1. Le système CRIT accordable se compose d'un guide d'onde, d'un résonateur en anneau libre de se mouvoir (anneau 1) et d'un résonateur en anneau fixe (anneau 2). L'anneau fixe est fabriqué sur une couche de SiO2 et l'anneau libre est soutenu par un piédestal et quatre rayons. Deux sources de lumière sont couplées dans le système CRIT à travers le guide d'onde: (a) la lumière de la sonde, qui est utilisée pour détecter le phénomène CRIT, et (b) la lumière de contrôle, qui est utilisée pour régler le phénomène CRIT. La lumière de la sonde peut être soit une source de faible puissance à large bande ou une source de lumière laser de faible puissance, de sorte que la force optique produite par la lumière de la sonde soit négligeable. Le laser de contrôle est injecté avec une grande énergie à résonance optique de l'anneau 1. La force optique correspondante entre l'anneau libre et

le substrat déforme les rayons. En raison de cette déformation, l'indice de réfraction effectif de l'anneau 1 est modifié, ce qui déplace la bande de transmission, et induit des changements du temps de groupe ainsi que l'accumulation du champ optique dans l'anneau 1. Deuxièmement, les propriétés du système CRIT à double résonateur en anneau couplés sont discutées au § 5.1.2. L'accumulation du champ optique dans l'anneau 1 traduit une capacité de stockage d'énergie. La transmitivité illustre la transmission de ce système, qui est une caractéristique importante pour cet interrupteur optique. Le retard de groupe traduit la dispersion du système, et un retard de groupe plus grand, signifie une plus petite vitesse de groupe. Troisièmement, la force optique entre l'anneau 1 et le substrat est analysée au § 5.1.3 sur la base de la loi de conservation de l'énergie. La force optique est associée à la longueur d'onde de la lumière, l'indice de réfraction effectif, l'écart anneau-substrat et la puissance d'entrée. Par la suite, la détermination du point stable est discutée au § 5.1.4. Lorsque l'anneau 1 est finalement arrêté à un point (ie. point stable), les conditions de stabilité sont: (a) la somme de toutes les forces extérieures sur l'anneau 1 est nulle, et (b) L'énergie potentielle de l'anneau 1 est au niveau local minimum. Enfin, le rapport de réglage est défini au § 5.1.5, qui comprend deux termes. Le premier terme est le rapport entre le changement du X versus la déformation et le second terme est la déformation à produire par unité de puissance d'entrée, où X représente l'accumulation de champ optique, la transmitivité et le retard de groupe.

Le § 5.2 montre les résultats numériques et les discussions du système CRIT accordable. Les résultats numériques de l'indice de réfraction effectif, le facteur d'atténuation et le coefficient de couplage sont illustrés au § 5.2.1. Les trois paramètres sont les paramètres nécessaires pour calculer l'accumulation de champ optique, la

transmitivité et le retard de groupe. L'indice de réfraction effectif diminue lorsque la longueur d'onde est augmentée l'écart étant fixe. Le facteur d'atténuation est diminué lorsque la longueur d'onde augmente l'écart étant fixe. Le facteur d'atténuation minimum ne figure ni à l'écart maximum ni minimum, mais l'écart à un écart de 0,13 um. Le coefficient de couplage anneau-anneau diminue lorsque la déformation est augmentée, la longueur d'onde étant fixe. D'autre part, lorsque la longueur d'onde est augmentée et la déformation est fixée, le coefficient de couplage anneau-anneau est augmenté. Les résultats numériques de l'accumulation de champ optique, la transmitivité et le retard de groupe sont présentés au § 5.2.2. L'accumulation de champ optique initial possède deux pics dus au couplage anneau-anneau, qui sont asymétriques en raison de la différence de phase collectés entre l'anneau 1 et l'anneau 2. Les pics de l'accumulation optique se décalent vers les hautes longueurs d'onde (*redshift*) lorsque le gap est diminué, et les valeurs maximales sont variées en conséquence. De même, les pics de transmitivité subissent un décalage dans le même sens lorsque le gap est réduit, et le minimum de transmitivité est varié en conséquence. Le retard de groupe présente le taux de variation du déphasage par rapport à la fréquence angulaire, et présente les temps de transit nécessaire pour la puissance optique de se propager à travers le CRIT. Le temps de retard le plus long à G = 0,3 um et à G = 0,05 um a une valeur de 2,16 ps et 153,41 ps, respectivement. Dans le § 5.2.3 la détermination du point de stabilité est discutée. La déformation finale (ΔG_f) correspondant au point stable de l'anneau 1 est déterminée par le minimum local du potentiel optomécanique, qui est égal au travail total effectué par la résultante des forces. Il y a 11 points de passage entre la courbe de la force optique et la courbe de la force mécanique lorsque la longueur d'onde de contrôle est 1,50061 um et la

puissance d'entrée est 50mW. Sur la base de la méthode graphique, la somme de toutes les forces extérieures sur l'anneau 1 est nulle en ces points. Il y a 6 points des 11 points correspondent aux minima locaux sur la courbe du potentiel, c'est à dire les 6 points sont des points stables et les 5 autres points sont des points instables. En supposant que le processus d'accord commence toujours à partir de l'état initial, l'anneau 1 ne n'a pas d'énergie supplémentaire pour passer à travers la barrière de potentiel entre le premier et le deuxième point stable lorsque la puissance d'entrée n'est pas très élevée. Par conséquent, le premier point stable est le seul point stable que l'anneau 1 peut atteindre et s'arrêtera là. Le ratio d'accord et la plage d'accordabilité sont discutés au § 5.2.3. Les bandes des plages d'accordabilité de la déformation finale sont 58,6, 19,3 et 4,2 nm à Go = 300, 200 et 100 nm, respectivement. Les résultats numériques montrent que le ratio d'accord de l'accumulation de champ optique atteint 4.1×10^{4} W^{-1}, le ratio de mise au point de transmitivité atteint -3.6×10^{3} W^{-1} lorsque l'écart initial est de 300 nm et le rapport de réglage du temps de groupe atteint 1.7 μsW^{-1} lorsque l'écart initial est de 200 nm.

Le § 5.3 illustre le flux des procédés de fabrication. Le système CRIT accordable est fabriqué en utilisant les procédés de fabrication de nanophotonique sur silicium, qui comprennent photolithographie, gravure sèche et humide, le dépôt chimique en phase vapeur (CVD) et de dépôt par pulvérisation. La gravure ionique réactive (RIE) est utilisée pour la technologie de gravure, qui a le mérite d'une haute sélectivité, anisotropie, est simple et compatible avec les processus CMOS. Des plaquettes de silicium sur isolant (SOI) sont utilisées pour la fabrication; elles consistent en une couche supérieure de silicium, une couche d'oxyde enterré (SiO_2) et une couche de substrat en silicium. La

couche supérieure de silicium d'épaisseur de 220 nm est utilisée comme la couche de structure. Le guide d'ondes, les résonateurs en anneaux, et les rayons sont tous deux fabriqués par cette couche supérieure de silicium. La couche d'oxyde a une épaisseur de 2 µm, qui est partiellement éliminée par gravure chimique humide au moyen du HF. La couche d'oxyde restante a trois fonctions. La première fonction est de soutenir l'anneau non libéré et le guide d'onde. La deuxième fonction du piédestal restant est de soutenir l'anneau à travers les rayons. Et la dernière fonction est d'agir comme le substrat, qui a une force optique attractive avec la partie libérée et empêche la lumière de pénétrer dans le substrat de silicium.

Le § 5.4 présente les résultats expérimentaux et discussions. Les dispositifs fabriqués et le dispositif expérimental sont introduits au § 5.4.1. Le système CRIT accordable est fabriqué par procédé de fabrication RIE, et se compose d'un guide d'onde, d'un résonateur en anneau libéré et d'un résonateur en anneau fixe. Dans le dispositif expérimental, le système d'alignement automatique de fibre est utilisé pour l'entrée et la sortie de la lumière. Cet équipement peut faire l'alignement entre la fibre conique et le guide le guide d'onde intégré sur la puce. Dans les expériences, une fibre conique est utilisée pour l'entrée de lumière et une autre fibre conique est utilisée pour la détection en sortie. Les résultats des mesures transmitivité du résonateur à anneau unique et celles du résonateur en double anneaux couplés sont présentés au § 5.4.2. Pour le résonateur en anneau seul, le facteur de qualité Q du pic d'absorption est de 4.5×10^3. Pour le résonateur à double anneaux couplés, le facteur Q est tombé à 2.6×10^3 en raison du chemin optique de propagation sur les anneaux plus long, ce qui cause une perte plus élevée. Après la gravure humide, les pics dégénérés du système CRIT accordable sont

devenus asymétriques du fait de la différence entre les résonateurs en anneaux couplés. Les résultats d'accordabilité du CRIT accordable sont présentés au § 5.4.3. Les résultats expérimentaux montrent que le système CRIT fabriqué est accordé avec succès par la puissance d'entrée par le biais de la force optique. Un rapport de d'accordabilité de la transmitivité d'une valeur de 1.7×10^2 W^{-1} à λ = 1569 nm et $P_{in} = 4{,}5\ mW$ est atteint. La force du système optique CRIT accordable a des applications potentielles dans la commutation optique, le stockage optique et la lumière lente.

Chapitre six: Conclusions et recommandations.

Dans ce chapitre, les conclusions de cette thèse sont présentées et des recommandations pour les travaux futurs sont répertoriées.

Le § 6.1 conclut cette thèse. Les systèmes de nano-opto-mécaniques (NOMS) sont explorés et deux dispositifs NOMS sont conçus, analysés théoriquement et modélisés. Le générateur de moment cinétique (AMG) est conçu pour le piégeage des nanoparticules et leur mise en rotation. Le système accordable de transparence induite par résonateurs couplés (*Coupled-Resonator-Induced Transparency* –CRIT) est conçu pour le réglage de l'accumulation de champ optique, la transmitivité et le retard de groupe.

Le § 6.2 donne des recommandations pour les travaux futurs. (a) Une description précise théorique de la diffusion de la lumière à partir des plots nano est souhaitable; (b) l'effet de réseau de Bragg peut être considéré et le rayon de l'anneau peut être encore optimisé; (c) D'autres analyses théoriques et expérimentales de l'AMG sont recommandées en vue d'applications dans le domaine biologique; (d) Un CRIT à accord optique peut être conçu dans d'autres systèmes CRIT ; (e) L'effet thermo-quantique peut être mesurée sur le système CRIT accordable par les points de la stabilité multiples.

CONTENTS

LIST OF FIGURES

LIST OF TABLES

CHAPTER 1

INTRODUCTION

1.1 Motivation

One trend of the machining development is to decrease the size of machines. The development of Microelectromechanical Systems (MEMS) brings the machines to micrometer scale [1-4]. Today, researches are targeting on nanoelectromechanical system (NEMS) [5] and nanooptoelectromechanical system (NOEMS) [6-8], which can bring the machines to nanometer scale. When the scale decreases from micrometer to nanometer, many physical properties become different. For instance, the electrical force becomes inefficient for nanostructure driving, but the optical force becomes relatively strong and can drive these small structures. Therefore, an electric free nano-opto-mechanical system (NOMS) is possible to be achieved. The nanomachines also have their specific mechanical properties in nano scales, e.g., the quantum understanding [9] and limitations [10]. On the other hand, recent developments of fabrication technologies enable researches to design and fabricate nanostructures with high quality and good repeatability. Finally, the nanomachines have merits of low power cost, high efficiency, ultrahigh sensitivity and good integratibility, which promise potential applications in environmental science, biological engineering, drug industry and medical treatment. Therefore, the research of NOMS will bring a major breakthrough in these areas. It's an important motivation of this thesis.

Nanorotor or nanomotor is one of the basic components for NOMS. There are several nanorotors being designed and tested [11-14]. However, all of them are driven by the orbital angular momentum of a focused beam. The focused beam is efficient to drive these rotors, but it also faces the difficuties of alignment and integration. A nanorotor with self alignment and good integratibility is desired.

The fast development of on-chip optical circuits decreases the size of optical device and has potential applications in optical computing and storage [15-16]. By combining the optomechanical components with the optical circuits, a new research topic is created, which introduces a new active unit into the passive device (optical circuits). For example, coupled-resonator-induced transparency (CRIT) is one typical phenomenon of the coupled ring resonator system (a passive device) and the release ring resonator is an efficient optomechanical component. When they are combined together, the differences of the optical and mechanical properties require further exploration.

1.2 Objective

The main objective of this PhD thesis is to clarify the basic concepts, perform theoretical analysis and obtain the numerical results of optical force, optical angular momentum and tunable CRIT system. Based on the optical force, two NOMS devices need to be developed for different applications. The first device is designed to generate a rotating optical field (ROF) for nanoparticle trapping and rotation. The second device is a tunable CRIT system, which is designed to change the optical field buildup, shift the transmission spectrum and vary the group delay.

The optical force and the optical torque are usually generated by a well-focused Laguerre-Gaussian (LG) beam. Due to the existence of optical intensity gradient, the gradient optical force is generated for small particle trapping. Due to the existence of orbital angular momentum, the optical torque is produced for particle rotation. However, the focused LG beam has poor integratibility. In this PhD thesis, a new device is designed to generate a ROF, which not only has optical intensity gradient and orbital angular momentum, but also has good integratibility. The design, the working principles and the numerical results are performed, demonstrated and discussed.

However, the generated ROF cannot directly predict the mechanical behaviors of a small particle inside it. Therefore, the optical force, the optical potential and the optical torque are required to be further explored. The optical force distributions, the optical potentials as well as the optical torques of the generated ROF are investigated and discussed in this PhD thesis.

CRIT has merits of large dispersion, high sensitivity and short response time. On the other hand, the optical force between a ring resonator and the substrate is strong enhanced. Therefore, a ring-based CRIT system can be efficiently tuned by the optical force. In this PhD thesis, the tunable ring-based CRIT system is designed, analyzed, simulated, fabricated and demonstrated.

1.3 Major contributions

In this PhD thesis, the NOMS is explored and two nano-opto-mechanical devices are designed, theoretically analyzed, simulated and fabricated.

First, an *angular momentum generator* (AMG) consisting of a ring resonator, a waveguide and a group of nano-rods is designed, analyzed and simulated for rotating optical field (ROF) generation. The nanorod's effects on light coupling are discussed. The generation of angular momentum is theoretically analyzed and numerically simulated. The theoretical analysis and numerical results show that a series of ROFs are generated when different resonant wavelengths are coupled into the generator. Except the 0-order ROF, all other ROFs have angular momenta but no linear momenta along the axis of rotation. The generation efficiency, the effects of nanorod on generation and the 3D optical field distribution are discussed.

Secondly, *the optical force distributions, the optical potentials and the optical torques* of the generated ROFs are analyzed, simulated and discussed. The force distributions are affected by the OF with different angular orders different objects. The optical potential indicates that the 0-order ROF has highest particle trapping capability. In addition, small particle will be trapped on a circle with radius of 213 nm at $l = 0$, 181 nm at $l = 1$, 358 nm at $l = 2$ and 380 nm at $l = 3$, which are the regions with the highest light intensity. The optical torques are analyzed and discussed for different objects, i.e. spherical nano-particle, nano-wire and nano-rotor. For the nano-particle, the optical torque drives it to rotate along a circular orbit. For the nano-wire, the optical torque

drives it to rotate when the rotating axis is at axis of the ring resonator. For the nano-rotor, there is a continuous optical torque on it.

Finally, *a tunable ring-based CRIT system* driven by the optical force is designed, theoretically analyzed, numerically simulated, fabricated and experimented. The tunable CRIT system consists of a bus waveguide and two coupled ring resonators, in which one is the released ring and the other is the fixed ring. Different input powers produce different optical forces on the released ring, which produce different final deformations, change the optical field buildup, shift the transmission spectrum, and vary the group delay. Numerical results show that the tuning ratio of optical field buildup reaches 4.1×10^{4} W^{-1}, the tuning ratio of transmittivity reaches -3.6×10^{3} W^{-1} when the original gap is 300 nm and the tuning ratio of group delay reaches 1.7 $\mu s W^{-1}$ when the original gap is 200 nm. The experimental results show that the fabricated tunable CRIT system is successfully tuned by the input power through the optical force. A tuning ratio of the transmittivity with a value of 1.7×10^{2} W^{-1} is achieved at λ = 1569 nm and P_{in} = 4.5 mW.

1.4 Organization of the thesis

This thesis is focused on the design, analysis and experiment of the ring-based NOMS devices. It is divided into six chapters:

Chapter one is the introduction including the motivation, objective, major contributions and organization of the thesis. The motivation section states why the PhD thesis is carried out. The objective section explains the targets of this thesis. The contribution section lists the innovations and findings.

Chapter two gives the literature survey on the optical ring resonator, the optical angular momentum, the optical force and the CRIT system. This chapter introduces the physical background for the optical ring resonator and the CRIT system, clarifies the basic concepts of the optical angular momentum and the optical force, and illustrates the corresponding applications.

Chapter three presents the working principles of the designed AMG, illustrates the typical optical field distributions, discussed the generation efficiencies and the nanorod effects for the angular momentum generation. §3.1 gives the theoretical analysis which includes design, single ring's properties, the effects of the nanorod for light coupling and the generation of angular momentum. §3.2 illustrates the numerical results of the nanorod effects for light coupling and the generation of angular momentum. §3.3 discusses the generation efficiency, the nanorod effects for the generation and the 3D optical field distribution. §3.4 summarizes this chapter.

Chapter four discusses the optical force, the optical potential and the optical torque of the generated ROFs for nano-particle trapping and rotation. §4.1 gives a

theoretical analysis of the optical force distributions, optical potential and optical torque. §4.2 presents the numerical results of optical force distributions, optical potential and optical torque. The effects of nano-rotor and angular order on the optical force distributions as well as the effects of different objects (nano-particle, nano-wire or nano-rotor) on the optical torques are also discussed. §4.3 summarizes this chapter.

Chapter five demonstrates a tunable CRIT system driven by the optical force between a released ring and the substrate. §5.1 presents the theoretical analysis of the tunable CRIT system. It includes the design, the properties of the ring-resonator-based CRIT, the optical force between a released ring and the substrate, the stable point determination and the tuning ratio. §5.2 shows the numerical results and the discussions of the tunable CRIT system. It includes the effective refractive index, the attenuation factor, the coupling coefficient, the optical field buildup, the transmittivity, the group delay, the stable point determination, the tuning ratio and the tuning range. §5.3 illustrates the fabrication processes flow for the tunable CRIT system. §5.4 gives the experimental results and discussions and §5.5 summarizes this chapter.

Chapter six gives the conclusions of this thesis and lists several recommendations for the future work.

CHAPTER 2
LITERATURE SURVEY

In this chapter, the basic concepts of the optical ring resonator, the optical angular momentum, the optical force and the coupled-resonator-induced transparency (CRIT) system are introduced and discussed. The optical ring resonator is the simplest case among different Whispering Gallery cavities (WGCs), and its modes are only described by the mode order *n*. The optical ring resonator not only has the function of wavelength selection, but also has feature of high Q-factor, which can be used for narrow linewidth optical filter, low threshold lasing, sensitive phase modulator and optical switch, etc. A circularly polarized light beam carries *spin angular momentum,* and laser beam with high order LG modes carries *orbital angular momentum*. Because most laser beam are cylindrically symmetric, researchers prefer to use the high order Laguerre-Gaussian (LG) beam to obtain the orbital angular momentum. High order LG beam with orbital angular momentum can be applied in many areas, which include atom trapping and particle rotation. Optical force is originated from the Lorentz force, which consist of two types, i.e., the optical gradient force generated by the intensity gradient and the radiation force generated by the change of the Poynting vector. Optical force is very tiny (10^{-12} ~ 10^{-7} N) and cannot be used in traditional mechanical system, but it is applicable in the micro- or nano- areas. CRIT is the phenomenon in coupled optical resonator system, which is analogous to electromagnetically induced transparency (EIT) in atomic systems. CRIT attracts more researchers' attention due to its attractive features, such as high extinction ratio transmission and sensitive output spectrum, etc.

2.1 Optical ring resonator

In this section, the optical cavity is introduced, followed by the basic concepts and the applications of the optical ring resonator.

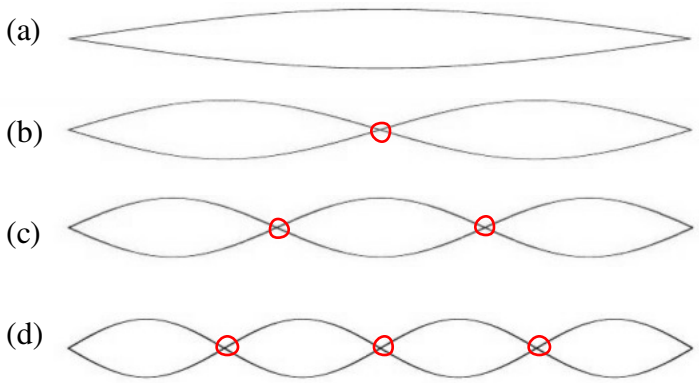

Figure 2.1: The modes of the FP cavity with (a) 0; (b) 1; (c) 2; and (d) 3 nodes.

2.1.1 Optical cavity

Optical cavity is a useful component in optical system. The typical optical cavity is the Fabry-Pérot (FP) cavity, which consists of two opposing flat mirrors. However, it is rarely used in large equipment, because the alignment of the two flat mirrors is very difficult. When the scale is decreased to hundreds of micrometers, the importance of the alignment is reduced, and it can be used, e.g. to measure the refractive index of a single cell [17]. Besides the micro FP cavity and the optical ring cavity, other micro cavities are reported recently [18], such as micropost [19], photonic crystal [20-21], microsphere [22], microdisk [23], capillary [24] and microtoroid [25].

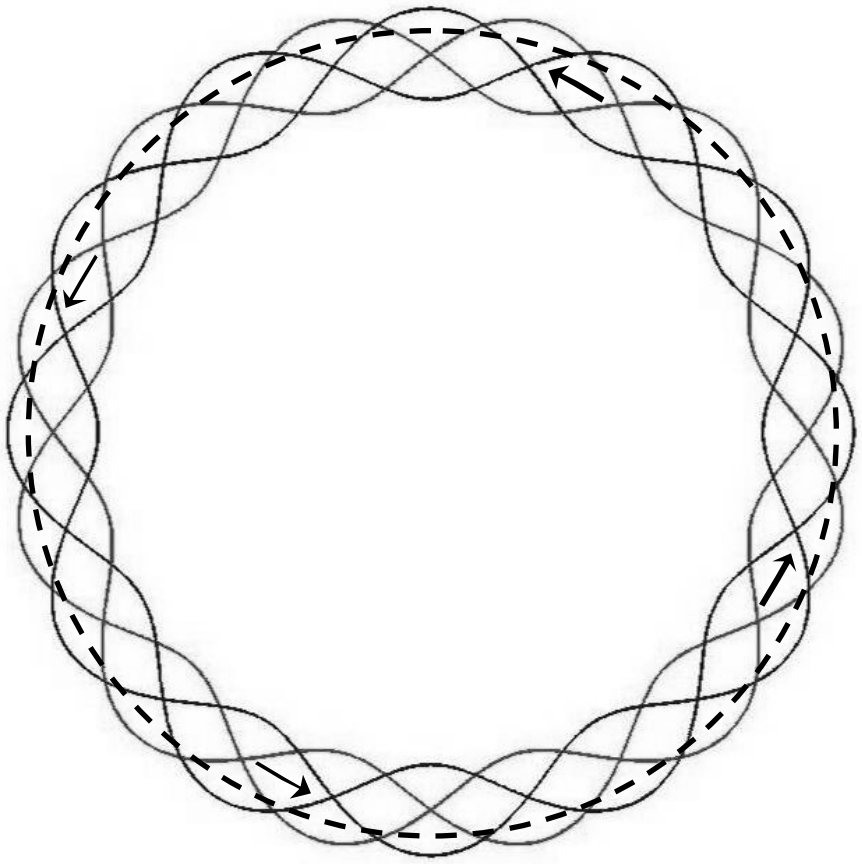

Figure 2.2: The Whispering Gallery modes inside the Whispering Gallery cavity

For an optical cavity, the produced standing wave patterns are the basic features, which are called the modes of the cavity. Based on the cavity modes, these cavities can be separated into three types. The first type is called FP liked optical cavity, such as micro FP cavity and micropost cavity. This kind of cavity has the nodes on their modes, at the points where the amplitude is always zero as shown in Fig. 2.1. The second type is the photonic crystal based optical cavity, which uses defects inside a photonic crystal to confine light, and its modes are related to the particular designs. The third type is named

as the Whispering Gallery cavity (WGC) [26], in which the optical modes are Whispering Gallery modes (WGM). One special feature of these modes is travelling, i.e. the nodes of the standing wave are not fixed at certain locations, but shifted from one position to the other continuously as shown in Fig. 2.2. The optical ring, toroid, capillary, disk and sphere are this kind of cavities.

The spherical cavity is the most general WGC and its WGM should be described by three parameters including the mode order (n), the mode number (l) and the azimuthal mode order (m), which indicates the angular intensity variation, the radial intensity variation and the spatial degeneracy respectively [27].

2.1.2 Basic concepts of optical ring resonator

Optical ring resonator is a special optical cavity, which consists of a closed waveguide loop and one or more bus waveguides coupled to this loop as shown in Fig. 2.3. When light of the appropriate wavelength is guided by the bus waveguide, it is partially coupled into the waveguide loop, and the intensity inside the loop is enhanced after multiple circulations due to constructive interference.

When $m = n$, the modes of the spherical cavity are same as the modes in a disk. In other word, the disk is a simplified case of the spherical cavity. When $l = 1$, the modes of the disk are same as the modes in a ring. Therefore, the optical ring resonator is the simplest case among all kinds of WGCs, and its modes are only described by the mode order n. The capillary and the toroid are also optical ring resonators when the spatial degeneracy is ignored.

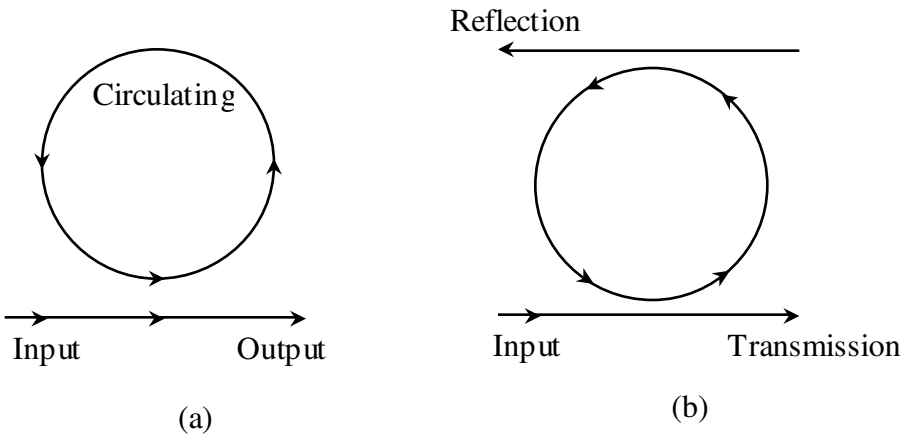

Figure 2.3: The schematic of optical ring resonator with (a) one bus waveguide; and (b) two bus waveguides.

Earlier optical ring resonator is also called fiber resonator [28-31], in which the waveguide loop is directly formed by a single mode fiber, and the idea is based on the light coupling between the fibers [32-33]. The design of fiber resonator was proposed twenty year ago. However, after ten years, limited experimental results of the fiber ring resonator presented. This is due to the two difficulties in experiments. First, the coupling coefficient between the two single mode fibers is very weak. The coupling coefficient is determined by the optical fields' overlap of the coupled fibers [32]. When the diameter of the optical fiber is larger than 10 μm, the coupling coefficient becomes very small. Secondly, it's really hard to create a stable small fiber loop. If the fiber loop is too large, the free spectrum range (FSR) becomes too small and the Q-factor becomes extremely high, such that the resonant peak cannot be detected. Recently, the fiber tapering technologies have a great improvement, which permits researchers to obtain a tapered fiber with diameter less than 3μm. Due to the increase of the coupling coefficient

between two fibers and the precise control mechanism, more experimental results are reported recently [34-35]. Even though the fiber resonator is successful fabricated and has several merits such as high Q-factor, low loss and convenient experiment, its shortages are still vital including low stability, poor repeatability and integratibility.

Besides the fiber tapering method, the optical circuits fabricated by semiconductor technologies can also improve the ring-waveguide coupling coefficient. The fabricated waveguide could have a width of 200 nm or smaller [36-38]. In earlier time, the on-chip silicon ring resonator has poor Q-factor caused by the "fused" ring and the bus waveguide section [16]. In other words, the ring-waveguide nano-gap is too small to be etched using technologies at that time. Today, this limitation doesn't exist, and the Q-factor is increased to 10^3 – 10^6 [36, 39-40]. The Q-factor is also affected by surface roughness [38], ring's radius [41] and fabricating materials [40, 42].

However, the Q-factor of the on-chip optical ring resonator is still not high enough for some applications, e.g., single bio-molecular detection, or single atom distinction. A new fabrication process is demonstrated and the fabricated ring resonator is known as toroid [43]. In this fabrication process, a CO_2 illumination step is introduced to smoothen the surface of the ring resonator. By this method, the resonator with Q-factor of 10^8, and the label-free single-molecular detection [25] as well as the single atom distinction [44-45] are achieved. However, the major drawback of the toroid cavity is the use of tapered fiber coupling method, which gives up the on-chip device integratibility and limits its commercialization.

On the other hand, the light input/output is the key issue for the applications of the on-chip ring resonator. Recently, the light input/output issue has been well solved by

tapered fiber aligner [46] or grating light coupling method [36, 47], such that the optical circuits based ring resonator is widely used in applications.

2.1.3 Applications of optical ring resonator

The optical ring resonator not only has the function of wavelength selection, but also has feature of high Q-factor, which can be used for narrow linewidth optical filter [15, 48], low threshold lasing [49-50], optical switch [51-52] and slow light [53-54].

A single ring resonator as shown in Fig. 2.3 (b) has the basic function of optical filter, in which the light with desired wavelength comes out from the reflection port when a multi-wavelength light is injected from the input port [16]. The coupled ring resonator provides passbands with sharper rolloff and flatter tops [55] and the two-dimensional ring resonator array has a boxlike filter response [56].

Due to the light circulating and the enhancement caused by interference, the ring resonator can also be used as a laser cavity. When a quantum-dot gain medium is employed in the ring resonator, the lasing which occurs in the telecommunication wavelength range is observed [57]. The gain medium GaInAsP-InP also can be used for the lasing [49].

By tuning the optical spectrum, the optical filter is converted into optical switch. The p-i-n based tuning provides blue-shifts at a rate of 1 nm/mA [52]. The coupled nonlinear optical ring resonator has low switching threshold [51].

The coupled ring resonator has also a large dispersion, which provides an ultra-slow group velocity in light propagation [53, 58]. The slowed light can store the optical signals [59] or can be used as optical buffer during optical computing [60].

Besides wavelength selection and high Q-factor, another feature of the WGM is the traveling standing wave. It could be scattered by the Rayleigh scatterers such as the defects in the materials [61-62], the roughness on the surface [38, 63], the designed nanostructures [64-67] and the attached nanoparticles [68].

Rayleigh scattering introduces a counterpropagating wave into the WGC and produces mode degeneration. In other words, one resonant peak in the frequency domain is split into two peaks. However, the peak splitting is usually very small, which can be covered by the low Q-factor peak. Thus, the ultra high Q-factor WGC is necessary for the observation of mode degeneration. For instance, a microsphere with Q-factor approximately 8×10^7 is used to observe the splitting of 29MHz which is produced by a single Rayleigh scatterer [62]. A microtoroid with Q-factor in order of 10^8 is used to observe the splitting around 100MHz, which is produced by an attached nanoparticle and can be used for sizing [68].

To increase the splitting produced by on Rayleigh scattering, a notch is introduced on to the ring resonator, which partially converted the forward travelling wave into backward traveling wave [66].

When the number of the Rayleigh scatterers is increased, other interesting phenomena appear besides the backscattering and the mode splitting. For instance, a grating with the same period as one WGM of a microdisk will suppress other WGMs, which is useful for lasing [67].

Besides the increase of number, increase of size is the alternative way to increase the scattering intensity. When the size is increased to a value which is larger than the wavelength, the Rayleigh scattering theory cannot be used. When the scatterer is another

WGC, the scattering problem is converted into cavity-cavity coupling, which can also produce the mode splitting [69-71].

2.2 Optical force

In this section, the generation, the features and the applications of optical force are introduced and discussed.

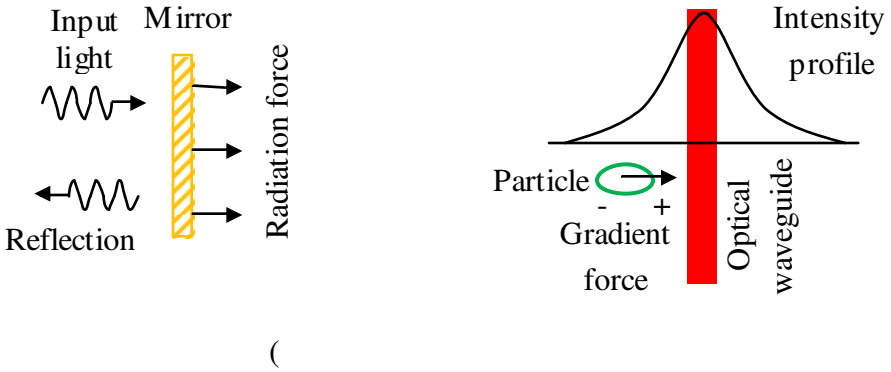

(

Figure 2.4: The schematic of (a) optical radiation force; and (b) optical gradient force.

2.2.1 Optical force generation

Optical force includes optical radiation force and optical gradient force. The optical radiation force is produced by the change of optical momentum. Optical momentum can be changed through optical reflection or scattering by an object, which results an optical radiation (scattering) force on the object. For instance, when a light beam shines on a fixed mirror, the input light is reflected by the mirror, and the direction of the optical momentum is changed, which results in the radiation force on the mirror as shown in Fig. 2.4 (a). The optical gradient force is also known as optical dipole force. When a small particle is in an optical field, e.g. the evanescent field of a sub-wavelength

optical waveguide, the particle can be treated as a dipole, and there is an optical gradient force to draw the particle to higher intensity area as shown in Fig. 2.4 (b).

Optical force originates from the Lorentz force, which is the force on a charged particle due to optical fields. It is in terms of the electric and magnetic fields and can be expressed as

$$\vec{F} = q\left(\vec{E} + \frac{d\vec{r}}{dt} \times \vec{B} \right) \tag{2.1}$$

where q is the electric charge of the particle and $\vec{r}$ is the displacement from the origin to the particle. The optical force on a large target can be treated as the resultant force of the Lorentz forces on each unit volume and it can be calculated by the surface integration of time averaged Maxwell stress tensor and expressed as [72]

$$\vec{F} = \left\langle \int_S T \cdot \vec{n} dS \right\rangle \tag{2.2}$$

where T is the Maxwell stress tensor and can be given as

$$T_{ij} \equiv \varepsilon_0 \left(E_i E_j - \frac{1}{2} \delta_{ij} E^2 \right) + \frac{1}{\mu_0} \left(B_i B_j - \frac{1}{2} \delta_{ij} B^2 \right), \tag{2.3}$$

where ε_0 and μ_0 are the permittivity and permeability of the vacuum respectively, δ_{ij} is Kronecker's delta. In an arbitrary point of the optical field, the optical force is determined by the gradient of the intensity as well as the change of Poynting vector [73], which correspond to optical gradient force and radiation force respectively. Optical gradient force can be generated by the intensity gradient and radiation force can be generated by the change of the Poynting vector.

A mirror can reflect a light beam back, which directly change the Poynting vector's direction and obtains a high radiation force [74]. A microparticle can change the Poynting vector's direction and value by light scattering, and also suffers an optical radiation force [75-76]. Refractive index variation is always associated with Poynting vector change, either by refraction or by reflection, which shows the existence of the radiation force.

A Gaussian beam has intensity gradient in the plane vertical to the propagation direction, and a well-focused Gaussian beam also has large intensity gradient along the propagation direction. Thus, a 3D distributed gradient force field is generated on a small particle for trapping [77]. The Gaussian beam can be replaced by the LG beam [78], HG beam [79], optical lattices [80] or any other beams with different intensity spatial distributions. The method to generate the intensity gradient is still by beam focusing.

There is another generating method, which is based on the evanescent field. The intensity of an evanescent field exhibits exponential decay with the distance from the boundary at which the field is formed [81]. An internal total reflection can generate the evanescent field on the external side, which consequently generate the optical gradient force [81]. The evanescent fields around a sub-micro-waveguide [7, 82], a ring resonator [8, 83] or the photonics crystal cavities [84-85] can also generate the optical force. In short, the well confined optical field provides larger intensity gradient as well as optical gradient force.

2.2.2 Applications of optical force

Optical force is very tiny, e.g., the radiation force on a in-water polystyrene sphere with radius of 100 nm is around 1 fN when the laser beam has a wavelength of 514.5 nm, a spot radius of 5μm and a power of 100 mW [75]. Even the optical gradient force is enhanced by the high Q-factor (10^7) optical WG cavity, it is still in the order of 100 nN [86], which is equal to the gravity of 10 μg mass. This feature determines the optical force cannot be used in traditional mechanical system, but applicable in the micro- or nano- areas [6, 87-88].

One of the famous applications is the optical tweezers. It's introduced by Ashkin and his colleagues, and plays a major role in single particle studies in physics, chemistry and biology [77, 88]. The optical tweezers use a strongly focused light beam to trap small objects [89]. When the small objects are atoms, a lot of interesting effects can be observed, including the saturation of the scattering force [90], 3D stable atom cooling [91] and trapping [92]. Small objects as well as the large biological materials, e.g., viruses and bacteria can be optically manipulated [93], mechanical stress is introduced in DNA or RNA fragment [94], a molecular motor based on adenosine-5'-triphosphate (ATP) is also studied [95]. ATP is the most important coenzyme in cells. It transfers energy between cells, and also transports chemical energy within cells for metabolism. Researchers try to convert the optical energy directly into chemical energy, which will bring a new revolution into the biological area.

Optical gradient force is limited by the distance due to the fact that the intensity gradient cannot exists at large range with a large value. Well-focused beam has a large intensity gradient but in a small volume, and unfocused beam has low intensity gradient

in a large volume. Therefore, the working distances of the designed devices are usually smaller than 1 μm [7, 96-97]. However, the optical gradient force based mechanical devices attract more and more attentions [98]. An attractive force between a nanowaveguide and the substrate is used for nanomechanical system [7]. The gradient force between two parallel nanowaveguides can resulting in both attractive and repulsive force, which is theoretical predicted at 2005 [82] and experimental verified at 2009 [99]. Besides the parallel nanowaveguides, the parallel ring resonators system exists also the attractive and repulsive force [8]. The WGC [97] as well as photonic crystal cavity [100] can be used to enhance the gradient force. On the other hand, the radiation force is not limited by the distance. When the radiation force is combined with the gradient force, the particle transportations are achieved on the distance from several micrometers [46, 83, 101-102] to 1 meter [103]. The radiation force is also used to cool [104] or enhance [105] the mechanical oscillation through the photon-phonon coupling. The optomechanical oscillation also can have a coupling the optical resonator, which produces a transparency in frequency domain, and is named as the optomechanically induced transparency [106].

2.3 Optical angular momentum

The basic concepts and the generation methods of optical angular momentum are introduced in this section.

2.3.1 Basic concepts of optical angular momentum

As discussed in the last section, the optical field carries linear momentum $\vec{P}$, which can be expressed as [107]

$$\vec{P} = \varepsilon_0 \vec{E} \times \vec{B} \tag{2.4}$$

where ε_0 is the vacuum permittivity, $\vec{E}$ is the electric field and $\vec{B}$ is the magnetic field. When the optical field is a transverse plane wave, $\vec{P}$ is in the direction of propagation. The optical radiation force is generated by the linear momentum change due to reflection or scattering of an object [108].

The angular momentum $\vec{\tau}$ of the optical field can be expressed as [107]

$$\vec{\tau} = \vec{r} \times \vec{P} = \varepsilon_0 \vec{r} \times \left(\vec{E} \times \vec{B} \right) \tag{2.5}$$

where $\vec{r}$ is the position from origin. The generated rotation is due to the linear momentum transfer from optical field to an object. Eq. (2.2) indicates that there is no component of angular momentum in the direction of propagation for a transverse plane wave. However, the fields of a laser beam are not strictly transverse and have small components in the direction of propagation. Thus, the angular momentum has a small component in the direction of propagation. The value of this small component is affected by the spatial intensity distributions of the laser beam.

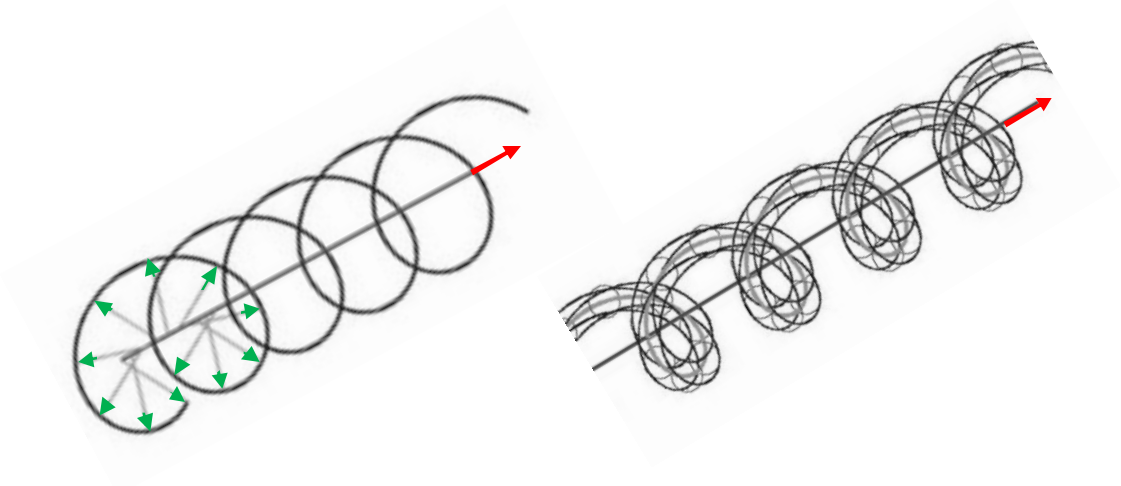

Figure 2.5: The schematic of optical (a) spin angular momentum carried by a circular polarized beam; and (b) orbital angular momentum carried by a Laguerre-Gaussian beam.

A circularly polarized light beam carries an angular momentum of $P\lambda/2\pi$, as suggested by Poynting in 1906 [109], where λ is the wavelength of light. This is verified by the experimental observation in 1936 [110]. A light beam with *l*-order Laguerre-Gaussian (LG) mode carries angular momentum of $Pl\lambda/2\pi$, which is pointed out by Allen in 1992 [107]. The angular momentum associated with the polarization is called *spin angular momentum* as shown in Fig. 2.5 (a) and the angular momentum associated with the intensity spatial distribution is named *orbital angular momentum* as shown in Fig. 2.5 (b). The spin angular momentum of a light beam is always intrinsic, and the orbital angular momentum is intrinsic only when the interaction with matter is about an axis where there is no net transverse momentum [111].

2.3.2 Generation methods of optical angular momentum

The spin angular momentum is obtained from the circular polarized light beam. There are many mature methods to obtain a circular polarized beam. Therefore, the generation methods of orbital angular momentum are majorly discussed in this section.

A high order LG beam carries orbital angular momentum. Therefore, the methods to generate a LG beam can generate orbital angular momentum.

LG beam refers to a laser beam has LG mode, which is described by Laguerre polynomials in cylindrical coordinates. It can be expressed by the vector potential as

$$A = u_{pl}(r,\theta,y)e^{-jky} \tag{2.6}$$

where

$$u_{pl}(r,\theta,y) = \frac{A_{pl}^{LG}}{w(z)}\left(\frac{r\sqrt{2}}{w(z)}\right)^{l} L_{pl}\left(\frac{2r^2}{w^2(z)}\right)\exp\left(\frac{-r^2}{w^2(z)}\right)\exp\left(\frac{ikr^2}{2R(z)}\right) \times\exp(-il\theta)\exp\left(-i(2p+l+1)\zeta(z)\right), \tag{2.7}$$

$w(z)$ is the radius of the beam, L_{pl} is the associated Laguerre polynomial, A_{pl}^{LG} is a constant. Because most laser beam is cylindrically symmetric, researchers prefer to use the high order LG beam to obtain the orbital angular momentum [112-113].

There are several methods to produce a high order LG beam. Researchers found that a spiral phaseplate with a step discontinuity in one period of helix can convert a HG mode into a LG mode [114]. Alternatively, a binary-phase diffractive element was reported for multimode LG mode generation [115]. Thereafter, a liquid crystal based spatial light modulator (SLM) [116-117] is used for the LG mode generation. Due to the computer programmable SLM system [118], it becomes very convenient to generate a

desired LG mode or a laser beam with arbitrary spatial intensity distribution and the researches in this area is increased fast.

The high order LG beam with orbital angular momentum can applied in many areas. A blue-detuned LG laser beam can be used to capture rubidium atoms with lifetime of 1.5 s for pulsed polarization gradient cooling [119]. By overlapping of LG beams, a dark ring-lattice can be generated for trapping cold and quantum degenerate atomic samples [120]. The torque of a focused LG beam on the absorbing sphere is analyzed for rotation [121]. The LG beam induced rotation on small absorptive particles is firstly observed [122-123]. The rotation on transparent particles is observed subsequently by using high order LG beam [111, 123]. The rotation is originated by the transfer of orbital angular momentum.

There are also several different types of light beam carry orbital angular momentum, such as a high-order Bessel beam [124] and a Hermite-Gaussian (HG) beam [79]. Therefore, the methods to generate a Bessel beam or a HG beam can also generate orbital angular momentum.

2.4 Coupled resonator induced transparency (CRIT)

In this section, the basic concepts, the features and applications of the CRIT system are introduced and discussed.

Table 1: the analogy between the ring resonator, the driven spring-mass oscillator and the multi-level atom-light interaction and the corresponding absorptions in frequency domain.

Ring resonator	Mass spring oscillator	Light-atom interaction	Absorption peak
Single resonator	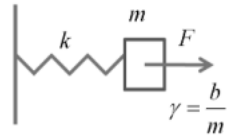	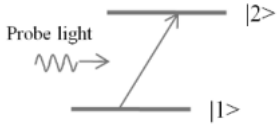	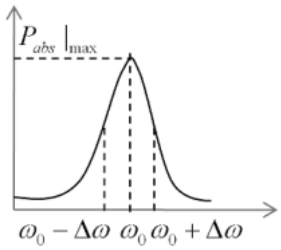
Coupled resonators	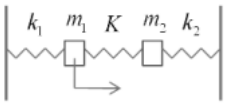	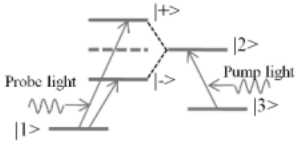	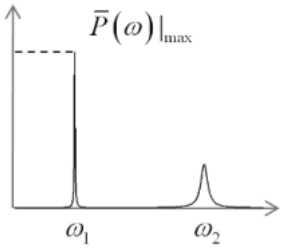

2.4.1 Basic concepts of CRIT

Coupled-resonator-induced transparency (CRIT) is the phenomenon in coupled optical resonator system, which is analogous to electromagnetically induced transparency (EIT) in atomic systems [58, 125-127]. EIT is a coherent optical nonlinearity in which transparency exists over a narrow spectral range within the absorption line of a medium. EIT phenomenon is originated from light atom interaction based on the destructive

interference of the transition probability between atomic states. Existence of EIT involves two light beams, which are tuned to interact with three quantum states of a material. When a medium absorbs a probe light beam with certain frequency in the two energy levels of the atomic system, the absorption in frequency domain has Lorentzian line shape. When a much stronger "coupling" field is tuned near resonance at a different transition, the presence of the coupling field creates a spectral "window" of transparency at the frequency of the probe light beam. Subsequently, the medium become transparent for the probe light beam. Consequently, the absorption peak is splitted into two peaks, which has the same line shape as Fano resonance [128-129]. It's found that the working principle of the EIT phenomenon is the interference/interaction of arbitrary two resonances, and it is not limited to optical systems [130]. The most recent representative case is the interaction between an optical ring resonator and a mechanical oscillator, which is known as optomechanically induced transparency [106].

The EIT-like phenomenon has also been demonstrated in coupled-resonator system. The analogy between the ring resonator, the driven spring-mass oscillator, and the multi-level atom-light interaction and the corresponding absorptions in frequency domain are shown in Table 1. The light absorption of a single ring resonator or the energy absorption of a single ring-mass oscillator has Lorentzian line shape, which is analogous to the adsorption of the probe light in a medium. When two ring resonators are coupled, a cancellation of absorption occurs on resonance due to mode splitting and classical destructive interference [125], such that the absorption of double coupled ring resonators or double coupled ring-mass oscillators has the same line shape as Fano resonance in EIT.

There is only one input light beam in CRIT system, but in the EIT system, there is another control beam besides the probe light. In CRIT system, the input light beam acts as the probe beam as well as the control beam. Due to the internal coupling, the input beam is divided several parts. One part of the light comes out directly, the others finally comes out after running of different optical paths through the coupled resonators system. In these different processes, the corresponding losses and phase changes are different, and the difference causes the resonant mode degeneration. The multi-paths light traveling introduces a mode splitting, which is EIT-like phenomenon and known as CRIT [131].

2.4.2 Applications of optical CRIT

CRIT attracts more researchers' attention due to its attractive features, such as extremely slow light [58], high extinction ratio transmission [51] and sensitive output spectrum [132].

In the CRIT system, the mode splitting is produced by the internal light coupling between the resonators but not the control light. The splitting can be tuned by changing the geometric design, e.g., the splitting in the transmission spectrum of DCRR is increased by decreasing the gap between two ring resonators [133]. Tuning of the mode splitting is achieved by changing the coupling coefficient in the two coupled fiber resonators system [132]. On the other hand, the tuning of splitting also means the tuning of light group velocity at certain wavelength.

Another method to tune the CRIT system is by varying the effective refractive index. There are different methods in tuning the effective refractive index. Based on the nonlinear effect, the effective refractive index is tuned for lower power switching [51]. In

this case, the effective refractive is tuned by the light intensity change in the nonlinear material. Thermo-optic tuning is reported for a tunable polymer ring laser [134]. For polymer, the thermo-optic coefficient has order of -10^{-4}/°C. Due to the free-carrier plasma dispersion effect, the refractive index is also changed when the voltage on p-i-n diodes changes [135].

2.5 Summary

In this chapter, the basic concepts of the optical ring resonator, the optical force, the optical angular momentum and the CRIT are introduced and discussed. In the first section, the optical cavity is introduced, followed by the basic concepts and the applications of the optical ring resonator. In this section, the generation, the features and the applications of the optical force are introduced and discussed. In the third section, the basic concepts and the generation methods of optical angular momentum are introduced. In the last section, the basic concepts, the features and applications of the CRIT system are introduced and discussed.

The optical ring resonator is a special optical cavity which consists of a closed waveguide loop and one or more bus waveguides coupled to this loop. It is the simplest case among all kinds of WGCs, and its modes are only described by the mode order *n*. In optical ring resonator, the nodes of the standing wave are not fixed at certain locations, but shifted from one place to the other continuously. The optical circuit based ring resonator has a large Q-factor range (10^3 ~ 10^6), good integratibility and mature fabrication processes. Therefore, it is widely used for narrow linewidth optical filter, low threshold lasing, sensitive phase modulator, optical switch, slow light and light storage.

Optical forces including optical radiation force and optical gradient force are originated from the Lorentz force. The change of optical linear momentum and the intensity gradient leads to the generation of optical radiation force and optical gradient force, respectively. An evanescent field can also generate gradient force. Optical force is very tiny (10^{-12} ~ 10^{-7} N). It cannot be used in the traditional mechanical system, but

applicable in the micro- or nano- areas. Optical gradient force is limited by the distance, but the radiation force is not. Combining the gradient force and the radiation force, the particle transportations are achieved in the distance from several micrometers to 1 meter.

An optical field carries linear momentum as well as angular momentum. The radiation pressure is caused by the linear momentum transfer from the optical field to an object, and the optical rotation is caused by the angular momentum transfer from the optical field to an object. A circularly polarized light beam carries spin angular momentum, and laser beam with high order LG modes carries orbital angular momentum. A high-order Bessel, or HG beam also carries orbital angular momentum. There are several methods to produce a high order LG beam, which include the spiral phaseplate method, the binary-phase diffractive element method and the SLM method. The high order LG beam with orbital angular momentum can be applied in many areas, which include atom trapping and particle rotation.

Coupled-resonator-induced transparency (CRIT) is the phenomenon in the coupled optical resonator system, which is analogous to electromagnetically induced transparency (EIT) in atomic systems. There is only one input light beam in CRIT system, but in the EIT system, there is another control beam besides the probe light. The multi-paths light traveling introduces a mode splitting in CRIT system. CRIT attracts more researchers' attention due to its attractive features, such as extremely slow light, high extinction ratio transmission and sensitive output spectrum. There are several methods to tune the CRIT system.

CHAPTER 3

OPTICAL ANGULAR MOMENTUM GENERATOR

The angular momentum carried by optical field includes spin angular momentum and orbital angular momentum, which corresponds to beam's circular polarization and intensity spatial distribution, respectively. The orbital angular momentum is usually obtained from Laguerre-Gaussian (LG) beam. However, this method requires particular experimental equipments and has poor integratibility. On the other hand, the on-chip optical circuits, e.g. the on-chip ring resonators, have been well developed recently, and have features of good integratibility, mature fabrications and high Q-factor. It provides a possibility to design a new angular momentum generator which is based on the ring resonator and has all the merits of the optical circuits.

In this chapter, an angular momentum generator (AMG) using a ring resonator surrounded by a group of nano-rods is proposed. The evanescent fields of the circulating light in the ring resonator are scattered by the nano-rods and generate a rotating optical field (ROF), which carries orbital angular momentum. Firstly, the theoretical model of the AMG is analyzed. Then, the numerical results are illustrated. Finally, the generation efficiencies, the effects of the nanorods as well as the 3D field distributions are discussed.

3.1 Theoretical analysis

The design of the angular momentum generator (AMG) is shown in Figure 3.1(a). It consists of a ring resonator surrounded by a group of circularly-periodical nano-rods, and a waveguide coupler. The light traveling through the AMG has two steps. First, the light is input from the waveguide and coupled into the ring resonator through evanescent field [48]. When the wavelength of the input light coincides with the resonant mode of the ring, the circulating field in the ring is enhanced and the output field at the end of the waveguide is dramatically decreased. Second, the evanescent wave of the confined light in the ring is scattered by the nano-rods and the scattered waves form an optical field inside the ring. The circulation of the scattered light in the ring causes a rotation of the optical field.

The parameters of the generator include the ring radius $R_{ring,}$ the ring width W_r, the number of the nano-rods N, the rod radius R_{rod}, the waveguide width W_w, the refractive index n_r, the input wavelength λ, the gap between the ring and the rods G_{rr}, the gap between the waveguide and the rod G_{wr}. With these parameters, the external radius of the ring is $R_e = R_{ring} + W_r/2$ and the internal radius of the ring is $R_{in} = R_{ring} - W_r/2$. The centers of rods are positioned at $(R_s, j\theta_0)$, where $R_s = R_e + G_{rr} + R_{rod}$, $\theta_0 = 2\pi/N$ and $j = 1, 2, \ldots, N$. The gap between the waveguide and the ring is $G = 2R_{rod} + G_{rr} + G_{wr}$ as shown in Fig. 3.1 (b).

To simplify the analysis of the AMG, the theoretical analysis is separated into three sections. First, the phase responses of the circulating and transmission intensities,

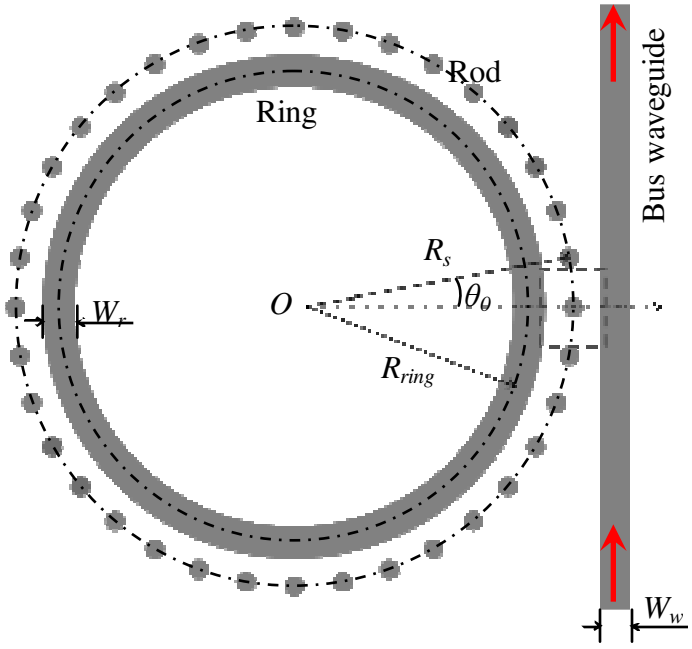

(a)

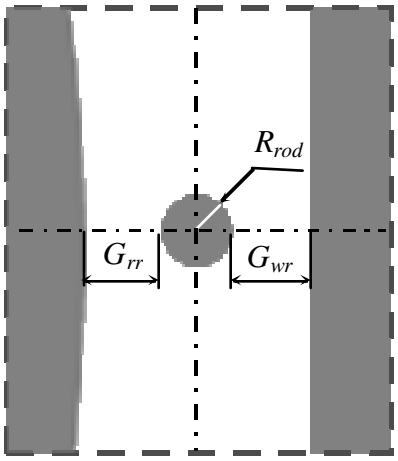

(b)

Figure 3.1: (a) Design of the angular momentum generator using a ring resonator surrounded by a group of nano-rods and (b) magnified view of the coupling region of the generator.

effective phase difference of a single ring resonator are discussed. Then, the effects of nanorod on light coupling coefficient and the field attenuation factor are analyzed. Finally, the generation of the angular momentum in the ring is presented.

3.1.1 Single ring resonator

Single ring resonator is a closed waveguide loop (ring) coupled to one or more input/output waveguides as shown in Fig. 3.2. Considering the single ring resonator with one waveguide, the light inputted from one end of the waveguide is partially coupled into the ring at the coupling region and subsequently circulating in the ring. Then, the circulating light is partially coupled out through the coupler again and mixed with the light directly propagating from the waveguide. When the coupling is lossless, this coupling process in a matrix is expressed as [136]

$$\begin{bmatrix} A_4 \\ A_3 \end{bmatrix} = \begin{bmatrix} \vec{r} & \vec{t} \\ -\vec{t}\,* & \vec{r}\,* \end{bmatrix} \begin{bmatrix} A_2 \\ A_1 \end{bmatrix}, \tag{3.1}$$

where A_i are the complex amplitudes of fields in which their squared magnitudes is corresponding to the powers. The coupler can be treated as a partially transmitting mirror with constant transitivity $\vec{t}$ and reflectivity $\vec{r}$ [137]. According to the coupling mode theory, the imaginary part of the reflectivity and the real part of the transitivity are both zero [138] such that the Eq. (3.1) can be rewritten as

$$\begin{bmatrix} A_4 \\ A_3 \end{bmatrix} = \begin{bmatrix} r & -jt \\ -jt & r \end{bmatrix} \begin{bmatrix} A_2 \\ A_1 \end{bmatrix}, \tag{3.2}$$

where r and t are the amplitudes of the reflectivity and the transitivity, respectively, which satisfy the relation $r^2 + t^2 = 1$; j is the imaginary unit. Based on Eq. (3.2), when light is coupled once either from waveguide to ring or from ring to waveguide, there is a $\pi/2$ phase delay.

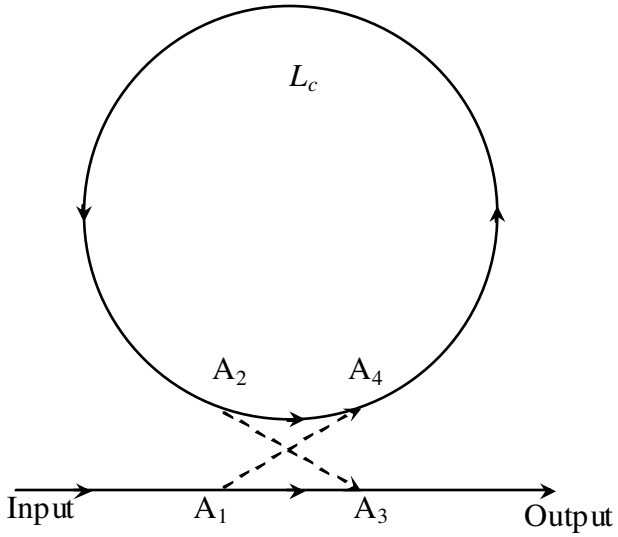

Figure 3.2: The schematic of single ring resonator with a waveguide.

Inside the ring resonator, the optical fields A_2 and A_4 are related by

$$A_2 = A_4 a_0 e^{-j\beta L_c}, \tag{3.3}$$

where $a_0 = e^{-\alpha L_c/2}$ is the field attenuation factor, L_c is the circumference of the ring, α is the power loss coefficient, β is the propagation constant and the βL_c is the collected phase caused by light propagation. When there is no gain medium in the ring, α is positive and a_0 is less than 1. When the input power is 1, i. e. $A_1 = 1$, based on Eqs. (3.2 – 3.3), the circulating field A_4 and the transmission field A_3 are given as

$$A_4 = \frac{-jt}{1 - r a_0 e^{-j\beta L_c}}, \tag{3.4}$$

$$A_2 = \frac{-jt a_0 e^{-j\beta L_c}}{1 - r a_0 e^{-j\beta L_c}}, \tag{3.5}$$

and

$$A_3 = \frac{r - a_0 e^{-j\beta L_c}}{1 - r a_0 e^{-j\beta L_c}}. \tag{3.6}$$

The total collected phase can be expressed as

$$\beta L_c = 2m\pi + \Delta\varphi, \tag{3.7}$$

where m is a positive integer and $\Delta\varphi$ is the relative collected pahse ($-\pi < \Delta\varphi < \pi$). Substituting Eq. (3.7) into Eqs. (3.4 – 3.6), the optical fields can be re-expressed as

$$A_2 = \frac{-jta_0 \cos\Delta\varphi - ta_0 \sin\Delta\varphi}{1 - ra_0 \cos\Delta\varphi + (ra_0 \sin\Delta\varphi)\, j}, \tag{3.8}$$

$$A_4 = \frac{-jt}{1 - ra_0 \cos\Delta\varphi + (ra_0 \sin\Delta\varphi)\, j}, \tag{3.9}$$

and

$$A_3 = \frac{r - a_0 \cos\Delta\varphi + (a_0 \sin\Delta\varphi)\, j}{1 - ra_0 \cos\Delta\varphi + (ra_0 \sin\Delta\varphi)\, j}. \tag{3.10}$$

Thus, the effective phase difference between the circulating optical field A_4 and the input optical field A_1 can be expressed as

$$\Phi(A_4) = -\tan^{-1}\left(\frac{ra_0 \sin\Delta\varphi}{1 - ra_0 \cos\Delta\varphi}\right) - \frac{\pi}{2}, \tag{3.11}$$

and the effective phase difference between the output optical field A_3 and the input optical field A_1 can be expressed as

$$\Phi(A_3) = -\tan^{-1}\left(\frac{ra_0 \sin\Delta\varphi}{1 - ra_0 \cos\Delta\varphi}\right) + \tan^{-1}\left(\frac{a_0 \sin\Delta\varphi}{r - a_0 \cos\Delta\varphi}\right). \tag{3.12}$$

Based on Eq. (3.8 – 3.9), the circulating intensities before (I_b) and after (I_a) the coupler can be expressed as

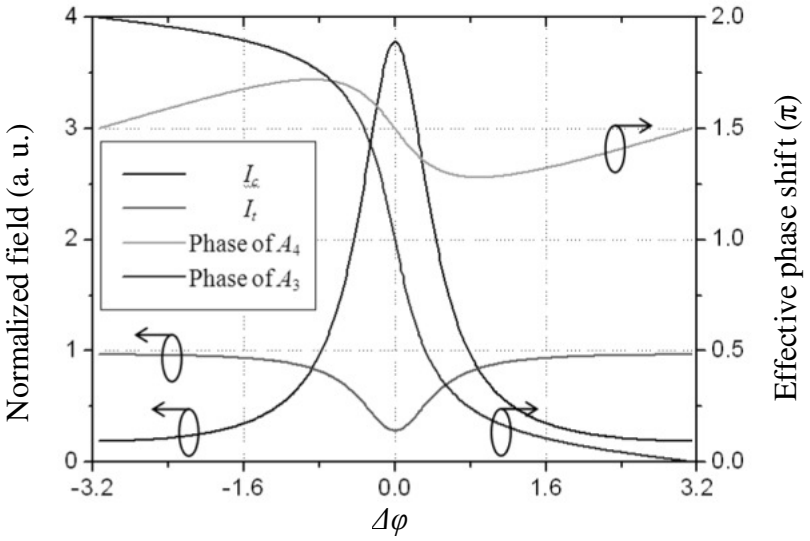

Figure 3.3: The phase responses of the circulating and transmission intensities, effective phase differences of A_4 and A_3.

$$I_b = |A_2|^2 = \frac{t^2 a_0^2}{1 + r^2 a_0^2 - 2ra_0 \cos\Delta\varphi}, \tag{3.13}$$

and

$$I_a = |A_4|^2 = \frac{t^2}{1 + r^2 a_0^2 - 2ra_0 \cos\Delta\varphi}. \tag{3.14}$$

When $\Delta\varphi = 0$, the maximum value of circulating intensity is given as

$$I_b|_{\max} = t^2 a_0^2 / (1 - ra_0)^2, \tag{3.15}$$

and

$$I_a|_{\max} = t^2 / (1 - ra_0)^2. \tag{3.16}$$

The corresponding effective phase difference is equal to –π/2 (i.e. $\varphi(A_4) = 1.5\pi$), and this

condition is defined as the resonant condition. On the other hand, the propagation constant can be expressed as

$$\beta = \frac{2\pi}{\lambda} N_{eff} = \frac{\omega}{c} N_{eff}, \tag{3.17}$$

where λ is light wavelength, ω is the light angular frequency, c is the light speed in the vacuum, and N_{eff} is effective refractive index of the ring. Combining Eq. (3.8) with Eq. (3.15), the resonant wavelength is expressed as

$$\lambda_m = N_{eff} L_c / m. \tag{3.18}$$

Based on Eq. (3.10), the transmission is

$$I_t = |A_3|^2 = 1 - \frac{(1-r^2)(1-a_0^2)}{1 + r^2 a_0^2 - 2ra_0 \cos\Delta\varphi}. \tag{3.19}$$

When it is at the resonant condition $\Delta\varphi = 0$, the I_{t} has minimum value is

$$I_t|_{\min} = \left(\frac{r - a_0}{1 - ra_0} \right)^2. \tag{3.20}$$

When $r = a_0$, the minimum transmission is equal to zero (i.e. $I_t|_{\min} = 0$), which means the energy of the input light is totally coupled into the ring resonator and there is no output from the end of the waveguide. This condition is known as the critical coupling condition, which includes two criteria: (a) the total collected phase on ring $\beta L_c = 2m\pi$ and (b) the reflectivity $r = a_0$.

When $a_0 = 0.9$ and $t^2 = 0.5$, the phase responses of the circulating and transmission intensities, effective phase difference of A_4 and A_3 are shown in Fig. 3.3.

3.1.2 The effects of the nanorod for light coupling

When the energy coupling coefficient of the waveguide-ring, K, is introduced into

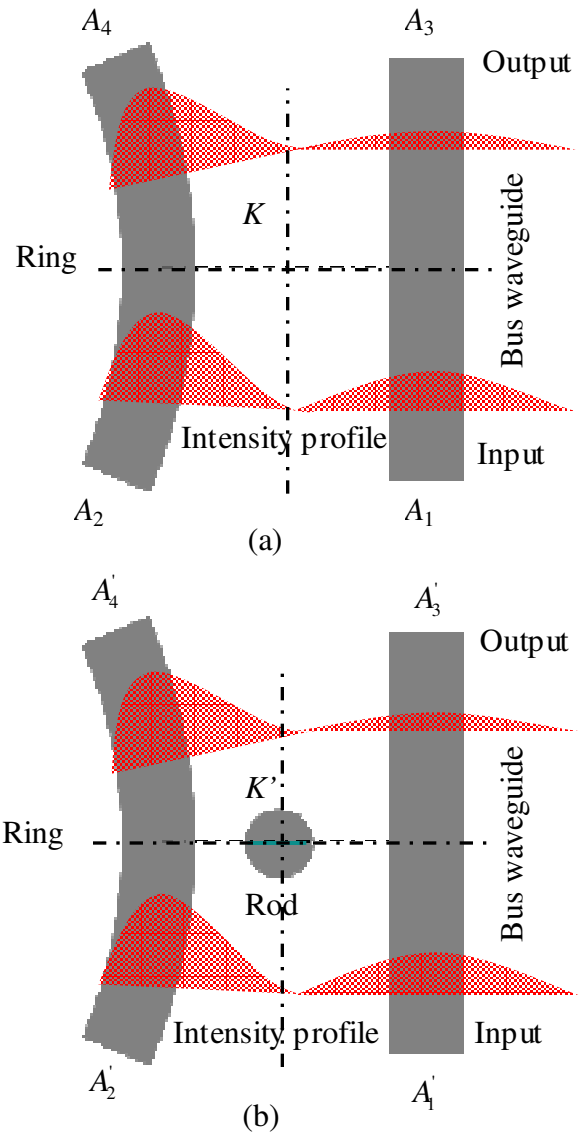

Figure 3.4: The light coupling process in the waveguide-ring coupler (a) without, and (b) with a rod between the waveguide and the ring.

the analysis, the amplitudes of the reflectivity and the transitivity can expressed as

$$t = \sqrt{K}, \tag{3.21}$$

and

$$r = \sqrt{1-K}. \tag{3.22}$$

When the minimum transmission is equal to zero (i.e. $I_t|_{\min} = 0$), it requires that the reflectivity equal to the field attenuation factor, i.e. $r = a_0$. Based on Eq. (3.22), this equation can be rewritten as $\sqrt{1-K} = a_0$, i.e. $K = 1-a_0^2$. Based on Eqs. (3.15) – (3.16), the intensity difference between I_a and I_b equals can be expressed as

$$\Delta I = I_a|_{\max} - I_b|_{\max} = \frac{t^2\left(1-a_0^2\right)}{\left(1-ra_0\right)^2}. \tag{3.23}$$

Substituting Eqs. (3.21)– (3.22) into Eq. (3.23), the intensity difference has a value of 1 (i.e. $\Delta I = 1$), which means that the total energy of input light is coupled into the ring resonator. The function of the waveguide-ring coupler can be replaced by a light source, which is located in the ring resonator, when the critical coupling condition is met. Under this condition, the theoretical analysis and the numerical simulation are dramatically simplified. However, before taking this simplification, the effects of the nanorod have to be analyzed.

Considering the light coupling process between the ring and the waveguide as shown in Fig. 3.4, the optical fields are directly coupled into each other without any rod between the waveguide and the ring as shown in Fig. 3.4 (a). When a rod is put in between the waveguide and the ring as shown in Fig. 3.4 (b), two effects are observed as, (a) the optical fields are partially scattered and (b) the penetration depth is enlarged. Scattering decreases the coupling coefficient (K), but the enlargement of the penetration

depth increases it. Hence, the total effect should be studied by numerical simulation using finite difference time domain (FDTD) method.

When the circulating field before the coupler is equal to zero (i.e. $A_2 = 0$), the coupling coefficient (K) can be expressed as

$$K = t^2 = \frac{|A_4|^2}{|A_1|^2}, \tag{3.24}$$

which provides a method to calculate the coupling coefficient (K) numerically.

The nanorod affects not only the coupling coefficient K, but also the field attenuation factor a_0. Comparing to the ring without any rods around it, the field attenuation factor a_0 is decreased. In order to satisfy the critical coupling condition, the coupling coefficient K should be increased correspondingly. One efficient way is to decrease the ring-waveguide gap. The details will be discussed in later section.

3.1.3 Generation of angular momentum

The intensity profile of the circulating light on the ring has much wider distribution outside the ring than that inside the ring as shown in Fig. 3.4 (b). Therefore, the nano-rods are designed to be positioned outside the ring so as to scatter light more efficiently. At a point with arbitrary radius r and angle θ in the polar coordinate system as shown in Fig. 3.5 (b), the amplitude of the scattered light $u(r, \theta)$ from one rod can be expressed as [139]

$$u(r,\theta) = s(\theta)\frac{e^{-ikr}}{ikr}u_o, \tag{3.25}$$

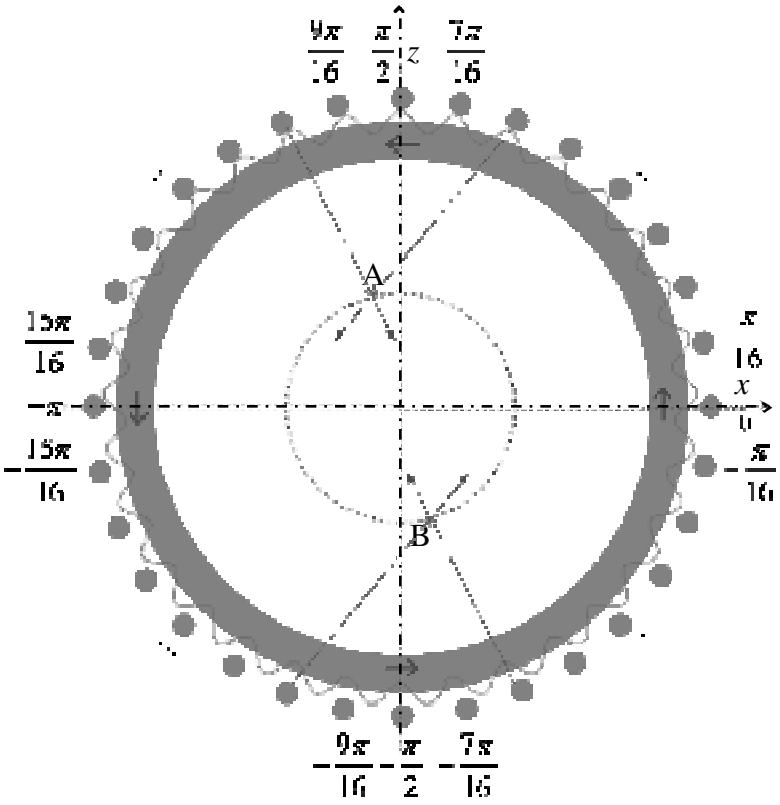

(a)

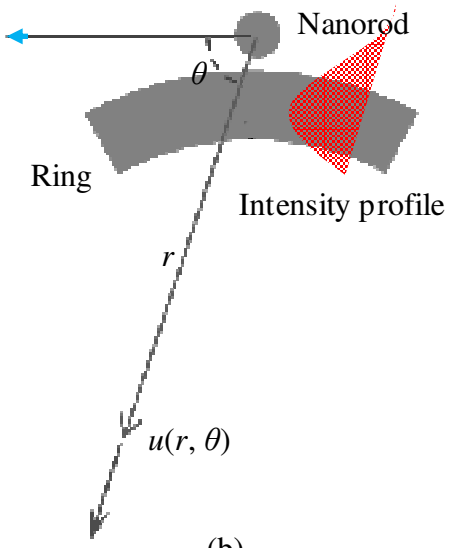

(b)

Figure 3.5: (a) electrical field inside the ring when the number of rods $N = 32$ and the order of WGM $n = 33$; and (b) Light scattered by a single rod in the evanescent field of a ring.

where $s(\theta)$ is the amplitude scattering factor, k is the wave vector and u_o is the amplitude of the evanescent wave. It is assumed that the scattered lights from the neighboring rods to a particular rod are negligible as compared to the evanescent wave of the circulating light. Thus, the multiple scattering effects can be neglected. Based on the superposition principle and Eq. (3.25), the optical field at an arbitrary point A can be written as

$$u_A = \sum_{j=1}^{N} u_j^A = \sum_{j=1}^{N} s\left(\theta_j^A\right) \frac{\exp(-ikr_j^A)}{ikr_j^A} u_o^j, \tag{3.26}$$

where subscript j corresponds to the j^{th} rod and θ_j^A refers to the angle between the light propagation direction and the light scattering direction in the polar coordinate system that uses the j^{th} rod as the origin.

When the number of the rods N is equal to the WGM order n (i.e. l = 0), the optical field distribution inside the ring resonator becomes a series of concentric circles. Such distribution is close to the pattern of the 0^{th} order Laguerre-Gaussian mode (LGM) in the plane perpendicular to the beam's propagation direction. When l = 1, the field distribution is same as the pattern of the 1^{st} order LGM in the plane perpendicular to the beam's propagation direction and its rotation frequency f_r is equal to the light frequency. Two special cases for l = 0 and l = 1 are studied here so as to exemplify the features of the optical field.

When $n = N$ = 32 (correspondingly l = 0), the circumference of the ring is 32 times of the effective wavelength λ_{eff}, and thus the evanescent waves scattered by different rods (u_o^j) have same phases. Therefore, the optical field on a concentric circle of the ring should be exactly the same when observed from the position of any rod. In other

words, the optical field on any concentric circle of the ring has a 32-fold rotational symmetry. In addition, it has mirror symmetry to any radial axis that passes one of the rods. With such a high level of symmetry, the optical field has little difference at different points on the concentric circle and thus presents to have a uniform distribution on the whole concentric circle. As a result, the optical field distribution inside the ring resonator becomes a series of concentric circles. Such distribution is close to the pattern of the 0^{th} order LGM in the plane perpendicular to the beam's propagation direction.

Considering another special case when l is 1 (i. e., $l = n - N = 1$, $n = 33$ and $N = 32$), there is a phase difference of $\frac{\pi}{16}$ between the two evanescent waves scattered by the j^{th} rod and the $(j + 1)^{th}$ rod. If the phase of the evanescent wave scattered by the 32^{nd} rod is set as 0, the other phases of the evanescent waves scattered by the 1^{st} to 31^{st} rods are shown in Fig. 3.5 (a). Point A and point B are on the same concentric circle of the ring, and they are symmetrical to the origin. Based on Eq. (3.26), the optical fields at the points A and B can be expressed as

$$u_A = \sum_{j=1}^{32} u_j^A = \sum_{j=1}^{32} s\left(\theta_j^A\right) \frac{\exp(-ikr_j^A)}{ikr_j^A} u_o^j, \tag{3.27}$$

and

$$u_B = \sum_{j=1}^{32} u_j^B = \sum_{j=1}^{32} s\left(\theta_j^B\right) \frac{\exp(-ikr_j^B)}{ikr_j^B} u_o^j. \tag{3.28}$$

Considering the contribution of the scattering from the 6^{th} and 10^{th} rods to point A, it has

$$u_6^A + u_{10}^A = s\left(\theta_6^A\right) \frac{\exp(-ikr_6^A)}{ikr_6^A} u_o^6 + s\left(\theta_{10}^A\right) \frac{\exp(-ikr_{10}^A)}{ikr_{10}^A} u_o^{10}. \tag{3.29}$$

The phase difference between the evanescent waves scattered by the j^{th} rod and the 32^{nd} rod is $\frac{j\pi}{16}$ ($u_o^j = u_o^{32}\exp\left(i\left(\frac{j\pi}{16}\right)\right)$), and then Eq. (3.29) is expressed as

$$u_6^A + u_{10}^A = u_o^{32}\left[s\left(\theta_6^A\right)\frac{\exp(-ikr_6^A)}{ikr_6^A}\exp\left(i\frac{6\pi}{16}\right) + s\left(\theta_{10}^A\right)\frac{\exp(-ikr_{10}^A)}{ikr_{10}^A}\exp\left(i\frac{10\pi}{16}\right)\right]. \qquad (3.30)$$

Based on the geometrical relationship as shown in Fig. 3.5 (b), $r_6^A = r_{22}^B$, $r_{10}^A = r_{26}^B$, $\theta_6^A = \theta_{22}^B$ and $\theta_{10}^A = \theta_{26}^B$. Then, Eq. (3.30) can be rewritten as

$$u_6^A + u_{10}^A = u_o^{32}\left[s\left(\theta_{22}^B\right)\frac{\exp(-ikr_{22}^B)}{ikr_{22}^B}\exp\left(i\frac{-10\pi}{16}\right) + s\left(\theta_{26}^B\right)\frac{\exp(-ikr_{26}^B)}{ikr_{26}^B}\exp\left(i\frac{-6\pi}{16}\right)\right]\exp(i\pi)$$

$$= \left(u_{22}^B + u_{26}^B\right)\exp\left(i\pi\right), \qquad (3.31)$$

which means the contribution of the scattered lights from the 6^{th} and 10^{th} rods to point A is same as that from the 22^{th} and 26^{th} rods to point B, except for a π phase difference. Considering the rotational symmetry of the generator, the total optical fields at the points A and B should have a π phase difference ($u_A = u_B\exp\left(i\pi\right)$), which means the optical field distribution inside the ring resonator is symmetric to the origin but has different directions. This distribution is same as the pattern of the 1^{st}-order LGM in the plane perpendicular to the beam's propagation direction.

When the light on the ring propagates by $\frac{\lambda_{eff}}{32}$, the 0-phase rod and ±π phase rod are shifted to the next rods, and the *x*-axis and *z*-axis have a $\frac{\pi}{16}$ rotation around the *y*-axis. As a result, the optical field distribution inside the ring has a rotation of π/16. Therefore, the rotation frequency f_r is equal to the light frequency (i.e. $f_r = f$).

Similarly, when the difference between n and N is equal to l ($l = |n - N|$), the optical field distribution inside the ring resonator has an l-fold rotational symmetry. This distribution is same as the pattern of the l-order (angular order) LGM. The corresponding optical field distribution has the rotation frequency f_r, which is equal to the light frequency f divided by the order l (i.e. $f_r = \frac{f}{l}$). Hence, the corresponding optical field is called rotating optical field (ROF).

The linear momentum P and angular momentum J of the ROF can be calculated as [107]

$$\vec{P} = \vec{E} \times \vec{B}, \tag{3.32}$$

and

$$\vec{J} = \varepsilon_0 \int \vec{r} \times (\vec{E} \times \vec{B}) d\vec{r}, \tag{3.33}$$

where ε_0 is the vacuum permittivity. Since the light propagates only in the xz-plane, the linear momentum on the y-direction is zero (i.e. $P_z = 0$). Consider the rotation around the y-axis (i. e. $r_y = 0$), the angular momentum carried by the ROF only exists in the y direction (i.e. $J_y \neq 0$, $J_x = 0$, $J_z = 0$). Thus, along the y-axis there is no linear momentum but only angular momentum.

3.2 The results of numerical simulation

Based on the FDTD method, a series of ROFs are simulated, and the considered parameters include R_{ring}, W_r, N, R_{rod}, G_{rr}, G_{wr}, W_w, n_r and λ. In order to simplify the simulation, the light coupling effect and the angular momentum generation will be discussed separately.

3.2.1 The nanorod effects for light coupling

The relative intensity in the ring is directly related to the ring radius R_{ring}, the intensity loss and the ring's field loss. The intensity loss is associated with the R_{rod}, G_{rr}, G_{wr} and n_r, whereas the ring's field loss is associated with W_r and λ.

It's already known that when the gap is decreased, the coupling coefficient (K) is increased [15]. In order to study the influence of the nano-rod on the light coupling, the value of R_{ring} is set as a constant. Simulation shows that under the conditions $|A_2| = |A_2'| = 0$ and $|A_1| = |A_1'|$, the coupler with a rod has higher coupling coefficient ($K' > K$), which is concluded from the calculated results at the beginning ($|A_4| < |A_4'|$) as shown in Fig. 3.6 (a) and (c). When the rod radius R_{rod} is increased, the relative circulating field $\frac{|A_4|}{|A_1|}$) is reduced. When there is a rod inside the coupler, the amplitude of circulating field ($|A_4|$) is decreased as shown in Fig. 3.6 (b) and (d).

Based on Eqs. (3.16), (3.21) and (3.22), the relative circulating field at the resonant condition ($\frac{|A_4|}{|A_1|}$, i.e. $(I_a|_{max})^{1/2}$) is affected by the ring-waveguide coupling

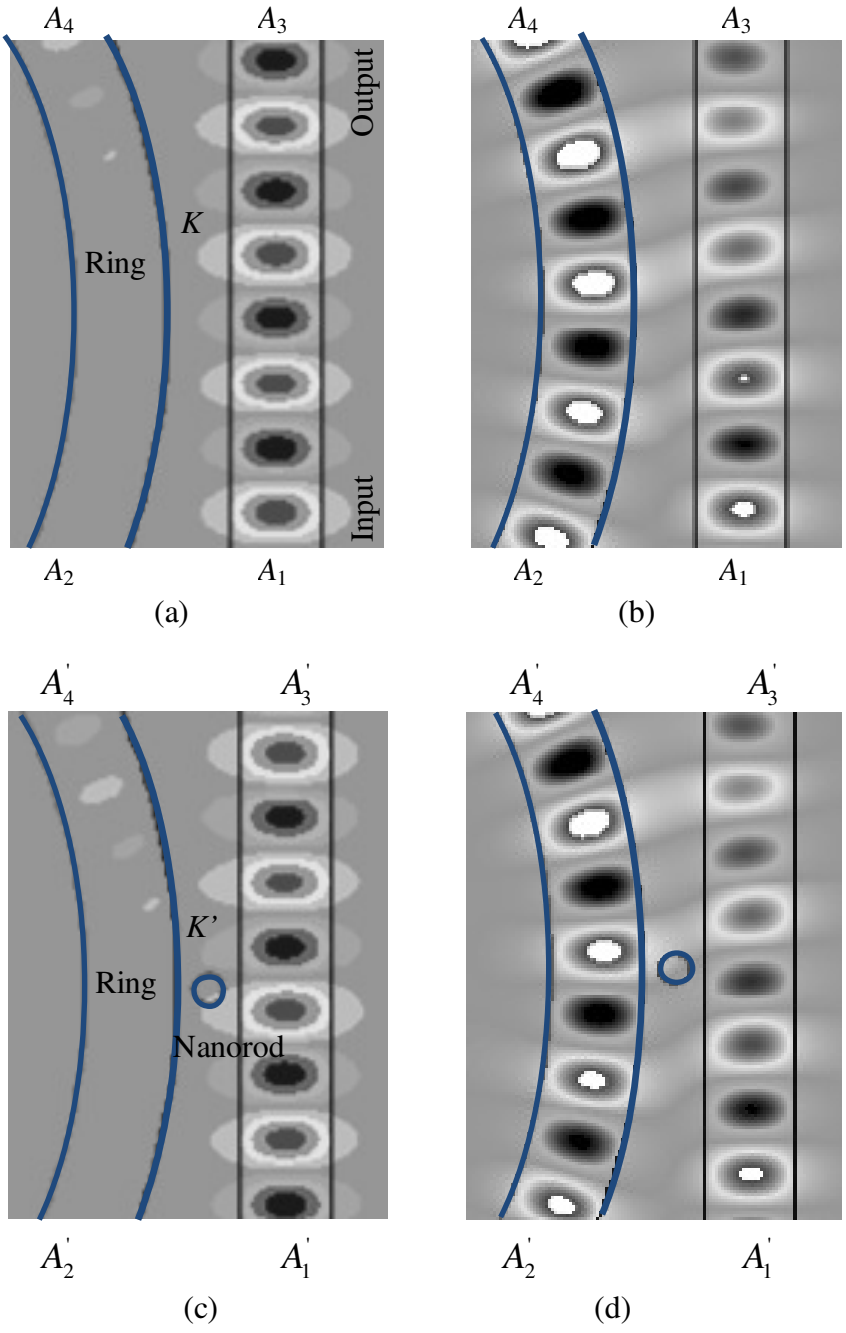

Figure 3.6: The light coupling between the ring and the waveguide (a) without a rod and at the beginning; (b) without a rod and in the stable state; (c) with a rod and at the beginning; and (d) with a rod and in the stable state.

coefficient (K) and the field attenuation factor (a_0). K is a function of the wavelength λ, the ring-waveguide gap G, the radius of nanorod (R_{rod}) and the locations of nanorod (G_{rr}/G_{wr}). The a_0 is a function of the wavelength λ, the radius of nanorod (R_{rod}) and the locations of nanorod (G_{rr}). The relative circulating field at the resonant condition is varied when the G is increased, as shown in Fig. 3.7 (a). It can be seen that when the wavelength is increased, the maximum value of the relative circulating field is varied, and the corresponding gap is increased.

The relative circulating field at the resonant condition is varied when the R_{rod} is increased as shown in Fig. 3.7 (a). The other parameters are fixed at G = 0.2 μm, n_r = 1.6, λ = 619.1 nm and $W_r = W_w$ = 0.3 μm. It can be seen that, when the radius of the nanorod is increased, the relative circulating field is decreased. The trend is changed from decrease to increase after the critical value at R_{rod} = 0.1 μm, which is due to the overlap of the rod with the ring/waveguide. When the gap ratio ($\frac{G_{rr}}{G_{wr}}$) of the nanorod is increased, which means the nanorod is moving toward the waveguide, the relative circulating field is increased. The trend is also changed from increase to decrease after the critical value at R_{rod} = 0.1 μm. Further studies show that these conclusions are still correct when the refractive index is increased from 1.6 to 3.476.

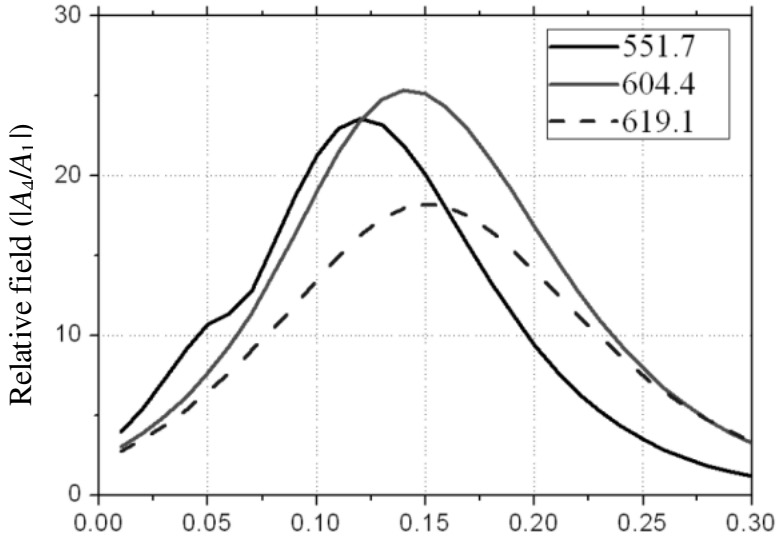

(a)

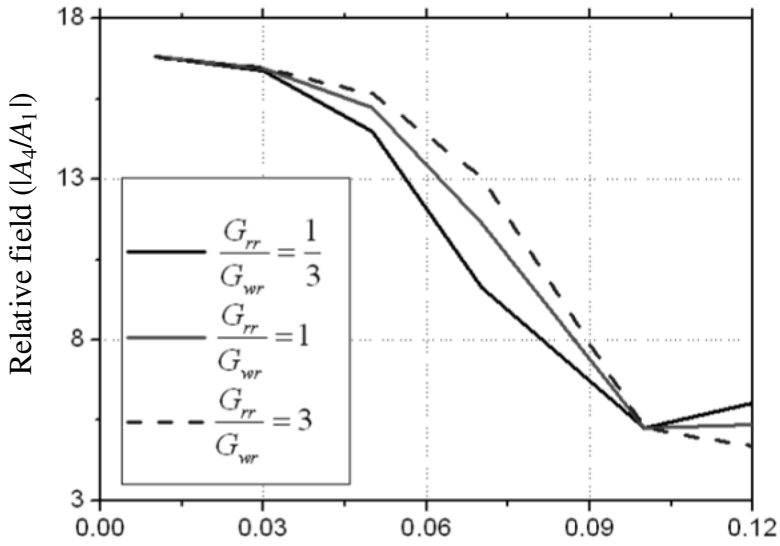

(b)

Figure 3.7: The relative circulating field as a function of (a) the gap between the ring and the waveguide at different wavelengths; and (b) the rod radius at different ratios of gaps.

3.2.2 Generation of angular momentum

For the angular momentum generator, when the parameters are N = 32, R_{in} = 2.2 μm, R_{out} = 2.5 μm, R_{rod} = 0.1 μm, G_{rr} = 0.1 μm, n_r = 1.6 and $W_r = W_w$ = 0.3 μm, the numerical results show that a series of WGMs have the wavelengths of 578.50 nm, 592.13 nm, 606.81 nm, 621.83 nm, 636.93 nm, 654.89 nm, 672.90 nm, 691.93 nm and 712.07 nm, which correspond to the order n from 36 to 28 as shown in Fig. 3.8. When the wavelength is 654.89 nm (i.e. n = 33), the optical field distribution inside the ring resonator has 1-fold symmetric structure as shown in Fig. 3.9 (a) and (b), which agrees with the prediction in the section 3.2.3. The corresponding circulating intensity in the ring is 75.4, and the intensity difference between I_a and I_b is 1, which indicates that the field intensity decrease per circle is 1/75.4 (~ 1.3%) and it is negligible for the theoretical

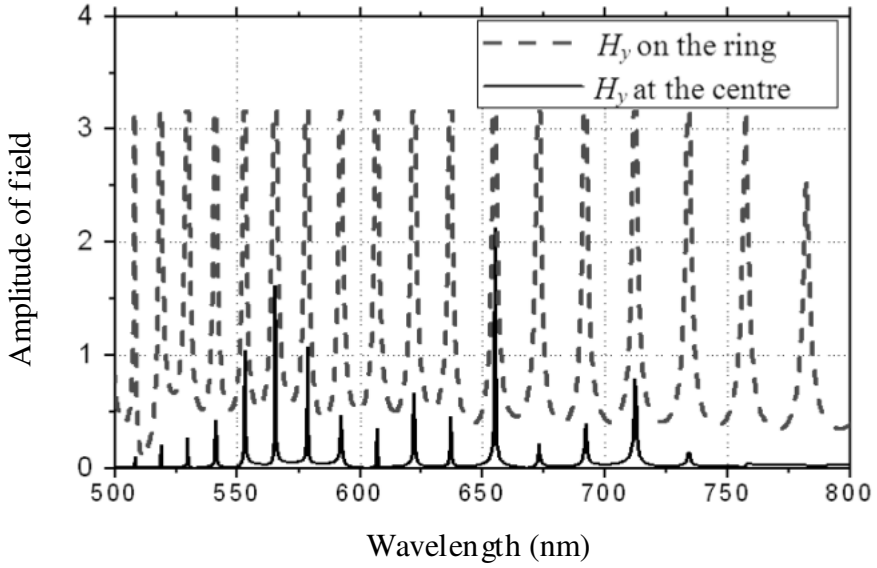

Figure 3.8: The amplitude of field H_y versus the wavelength.

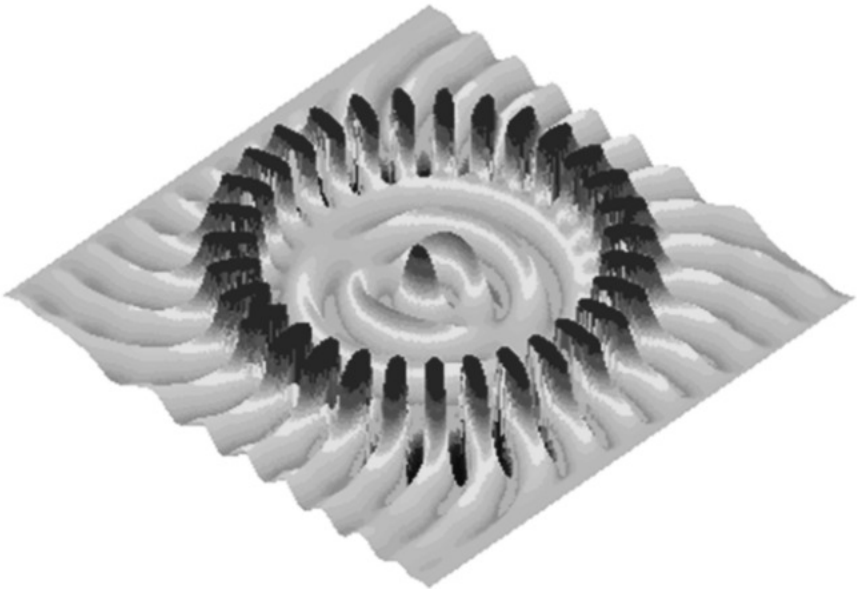

(a)

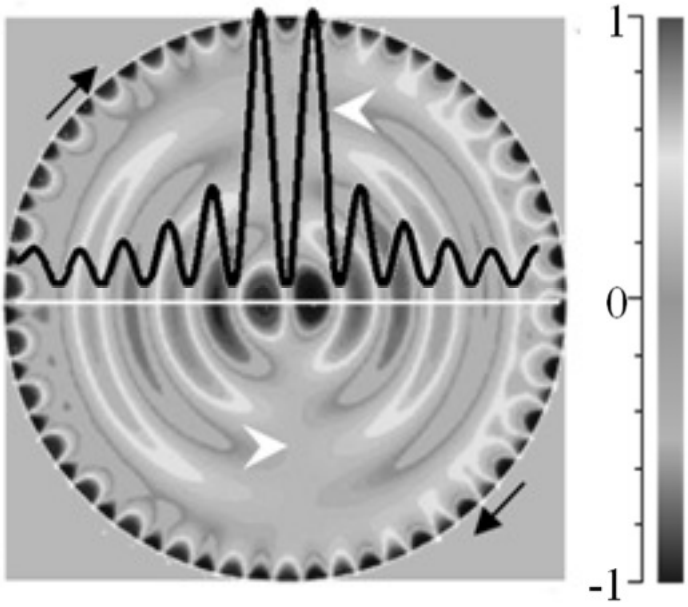

(b)

Figure 3.9: (a) The 3D view of the optical field distribution (H_y) of the AMG; and (b) The top view of the optical field distribution (H_y) inside the ring. The black line indicates the intensity distribution along the white line.

model. The field amplitude on the ring in Fig. 3.9 (a) is set to 1 for the convenience of observation, and the black line in Fig. 3.9 (b) is the intensity distribution along the white line. The black arrows indicate the light propagation direction in the ring resonator, and the white arrows indicate the optical field inside the ring has anticlockwise rotation.

When the wavelength is 636.93 nm, the order of WGM is 32, which is equal to the number of the rods *N*. The amplitude distribution of the optical field is a series of concentric circles as shown in Fig. 3.10. It matches with the analysis in the section 3.2.3. The optical field periodically varies amplitude and direction in a time period, which is equal to the period of the light in the ring resonator. The largest amplitude appears at the central of the field, which can be looked as the sub-wavelength focusing effect, and has applications such as nano particle trapping. The details will be discussed in next chapter.

Figs. 3.12 (a – d) show the 1^{st} – 4^{th} fold optical field distributions corresponding to the shorter wavelengths and Figs. 3.11 (e – h) show the optical field distributions corresponding to the longer wavelengths.

These optical fields not only have the *l*-fold rotational symmetric structure, but also have the rotation (except for $l = 0$). The relationship of the rotation frequencies ($f_r = \frac{f}{l}$) is also verified by the simulation results at different time frames [140]. The rotation axis is perpendicular to the *xz*-plane and the rotation direction is indicated by white arrows as shown in the Fig. 3.9 (b). In this specific case, the rotation direction is opposite to the light circulation direction as indicated by the black arrows. The simulation

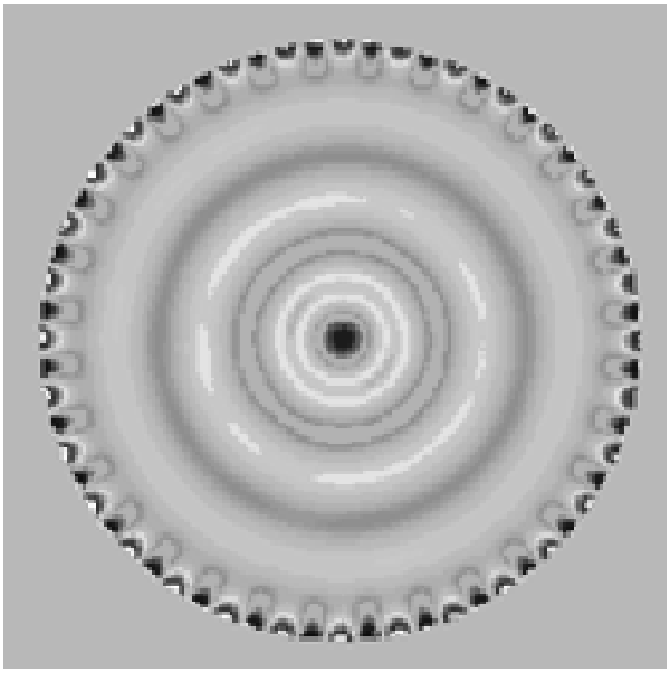

636.93 nm

Figure 3.10: The optical field distribution when $l = 0$ and $n = 32$.

results show that the rotation direction is opposite to the light circulation direction when $n < N$ (i.e. Figs. 3.11 (e – h)), and they are same when $n > N$ (i.e. Figs. 3.11 (a – d)). In all cases, the ROFs carry pure angular momenta.

The radial distributions of the generated ROFs are indicated in simulation results as shown in Figs. 3.11 (a – h). It can be seen that the radial orders (number of maxima and minima along the radius) of the field distributions are different due to the wavelength difference. For instance, the radial order is 5 at $\lambda = 578.5$ nm and 4 at $\lambda = 712.07$ nm as shown in Figs. 3.11 (e) and (i), respectively.

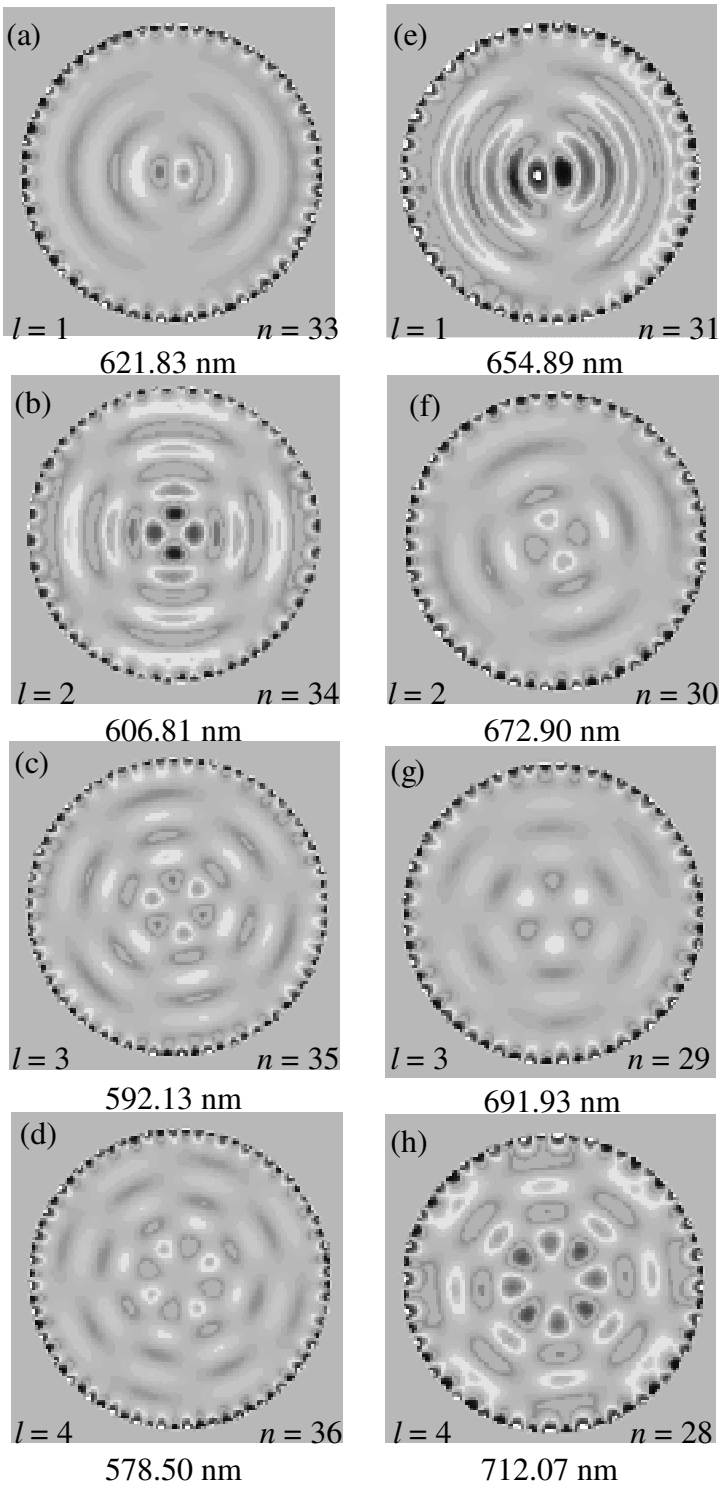

Figure 3.11: The generated ROFs. (a) – (d) the 1^{st} – 4^{th} order in the short wavelength range; and (e - h) the 1^{st} – 4^{th} order in the long wavelength range.

3.3 Discussions of the angular momentum generation

In this section, the generation efficiency, the effects of nanorod on generation and the backscattering effects are discussed.

3.3.1 The generation efficiency

The generation efficiency $\tau_{\pm l}$ of the *l*-order ROF is defined as

$$\tau_{\pm l} = \left| \frac{A_r^{\pm l}}{A_{in}} \right|^2, \quad l = 0, 1, 2, \ldots \tag{3.34}$$

where A_{in} is the input field, the $A_r^{\pm l}$ is the maximum amplitude of the *l*-order optical field, "+*l*" corresponds to the condition $n > N$ ($l = n - N$) and "- *l*" refers to $n < N$ ($l = N - n$). The ROF is a combination of the scattering from the nano-rods, the evanescent field at the rods' locations as well as the coupling effect of ring-waveguide coupler. Since the light propagation in the device is divided into two processes: (a) the input light from the waveguide is coupled into the ring resonator and is enhanced by the ring; and (b) the ring confined light generate evanescent field, which is scattered by these nano-rods, and these scattering lights form a ROF, the Eq. (3.34) can be rewritten as

$$\tau_{\pm l} = \left| \frac{A_c^{\lambda_n}}{A_{in}} \right|^2 \left| \frac{A_r^{\pm l}}{A_c^{\lambda_n}} \right|^2, \quad l = 0, 1, 2, \ldots \text{ and } n = 1, 2, \ldots \tag{3.35}$$

where $A_c^{\lambda_n}$ is the circulating field in the ring when the wavelength coincides with the *n*-order WGM. When the difference between the intensities after and before the coupling region (I_a and I_b) is ignored, the circulating field in the ring is equal to the optical field after the coupler (i.e. $A_c^{\lambda_n} = A_a^{\lambda_n}$), here the superscript 'λ_n' indicates that the field is still

wavelength dependent. Assuming the input optical field has amplitude of 1 (i.e. A_{in} = 1), the first term on the right side of Eq. (3.35) is the same as the circulating intensity in Eq. (3.14), and has maximum value of $\frac{t^2}{(1-ra_0)^2}$ at the resonant wavelength λ_n. The second term presents the scattering efficiency of the group of nano-rods. The generation efficiency of the *l*-order ROF is the same as the maximum intensity of the *l*-order optical field. In the simulation of field distributions, the intensity of the coupled light from the waveguide is set as 1, which means the intensity at the output of the waveguide is kept as zero. The gap between the waveguide and the ring is adjusted accordingly to maintain the coupling intensity independently of the circulating intensity on the ring.

The variable $A_r^{\pm l}$ is associated with the order of WGM *n*. When *n* is increased, the corresponding wavelength λ_n is decreased, and the amplitude of the evanescent field around the ring resonator is reduced. Once the wavelength λ_n is smaller than 550 nm, the evanescent fields at the outside of the ring become very weak, causing a low optical field inside the ring ($A_r^{\pm l} < 0.5$). In contrast, when *n* is decreased, λ_n goes up, and the radiation loss is enhanced, i.e., the attenuation factor a_0 is decreased, which decrease the circulating intensity in the ring. Therefore, the first term at right side of Eq. (3.35) is decreased, which decrease the generation efficiency $\tau_{\pm l}$ for the same scattering efficiency of these nanorods. The solid line in Fig. 3.8 shows that when λ_n is longer than 750 nm, the radiation loss is dominated and the circulating field $A_c^{\lambda_n}$ in Eq. (3.35) is

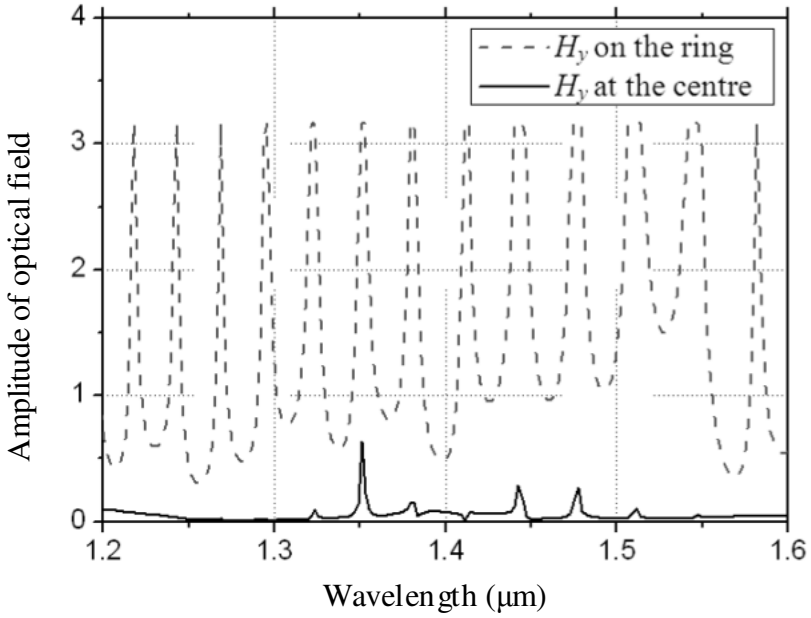

Figure 3.12: (a) the amplitude of field H_y versus wavelength (N =28, n_r =3.476).

reduced to a low level, which in turn causes the weak optical field inside the ring ($A_r^{\pm l} < 0.5$). The wavelength range that has $E_r^{\pm l} > 0.5$ decreases with the increasing of the number of the rods N and the refractive index n_r. For instance, when the n_r is increased to 3.476 (N = 28), the range is narrowed down to only one wavelength at 1350 nm as shown in Fig. 3.12.

3.3.2 The nanorod effects for the generation

For the same design, different order numbers l corresponds to different maximum amplitudes of the optical fields inside the ring. When the wavelength is increased from 519.2 nm to 541.6 nm (n_r = 1.6 and N = 36), the maximum amplitude of the optical field

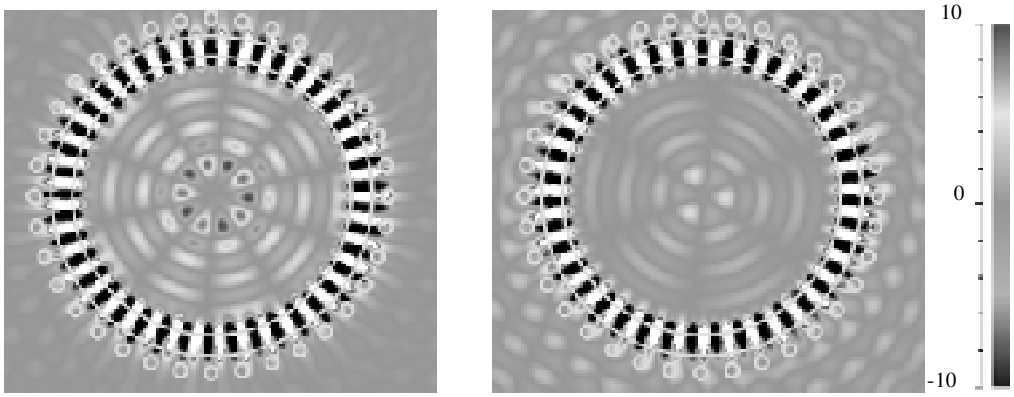

N = 36; λ= 519.2 nm

(a)

N = 36; λ= 541.6 nm

(b)

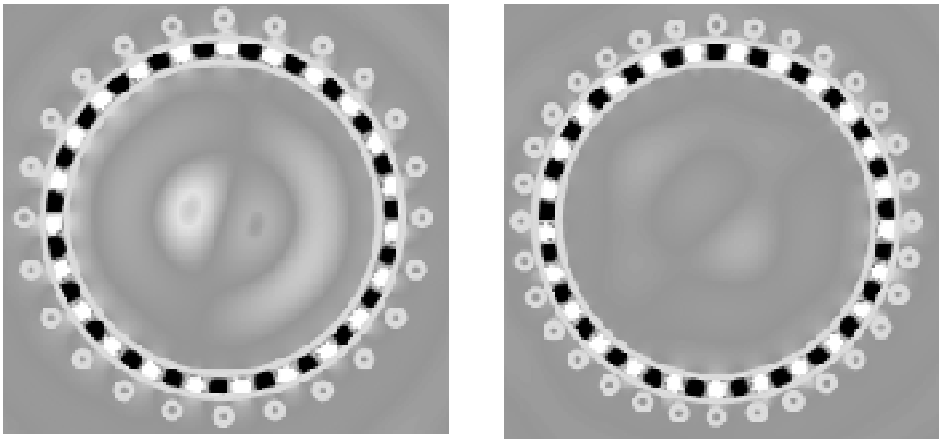

N = 24; n_r = 3.476

(c)

N = 32; n_r = 3.476

(d)

Figure 3.13: the field distribution when (a) N = 36 and λ = 519.2 nm; (b) N = 36 and λ= 541.6 nm; (c) N = 24 and n_r = 3.476; and (d) N = 32 and n_r = 3.476.

is decreased from 10 to 3.6, and most energy is scattered away rather than be confined inside the ring as shown in Figs. 3.13 (a) – (d).

For different N, the same l correspond different n (i. e. $n = N \pm l$) and a wide range of λ_n. Since the wavelength affects the circulating intensity and the evanescent field, the amplitudes of the generated fields with same order numbers l cannot present the generation efficiency. To investigate the variations of the maximum value of all the maximum amplitudes $A_r^{\pm l}|_{\max}$ with N, the rod R_{rod} as well as the refractive index n_r should be considered. The relationships are shown in Figs. 3.14 (a) and (b). With $n_r = 1.6$ and $R_{rod} = 0.08$ μm, $A_r^{\pm l}|_{\max}$ tends to increase when N goes from 24 to 37, and then decreases when $N > 37$ (see Fig. 3.14 (a)). For different rod radii, the peak positions are different. The maximum value is 10 times higher than the amplitude of the input field when $N = 36$, $R_{rod} = 120$ nm, $n_r = 1.6$, $\lambda = 519.2$ nm, $l = 5$ and circulating field $A_c = 14.7$. The field distribution is shown in Fig. 3.14 (a). When $n_r = 1.6$, 2.6 and 3.476, the peak position appear at $N = 37$, 28 and 24, respectively (see Fig. 3.14 (b)). After the peak position, the increase of N causes a reduction of $A_r^{\pm l}|_{\max}$. For example, when N is increased from 24 to 32 ($n_r = 3.476$, $l = 1$), $A_r^{\pm l}|_{\max}$ is reduced from 1.9 to 0.2 as shown in Figs. 3.13 (c) and (d).

The gap between the ring and the rods (G_{rr}) also affects $A_r^{\pm l}|_{\max}$. An increase of G_{rr} causes a reduction of the scattering from each rod, whereas a decrease of G_{rr} results in higher optical field loss, which in turn decreases the circulating field on the ring. For R_{rod} = 100 nm and $n_r = 1.6$, the optimized value is 80 nm as shown in Fig. 3.14 (c).

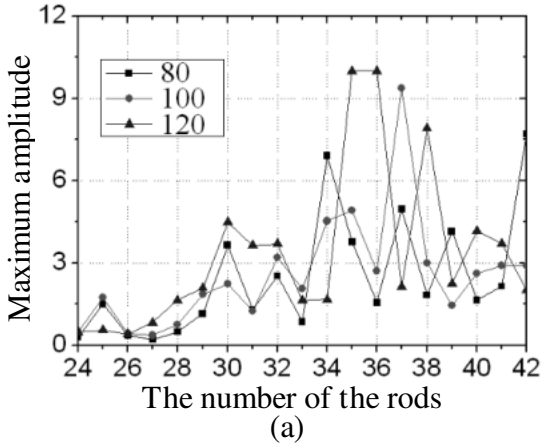

(a)

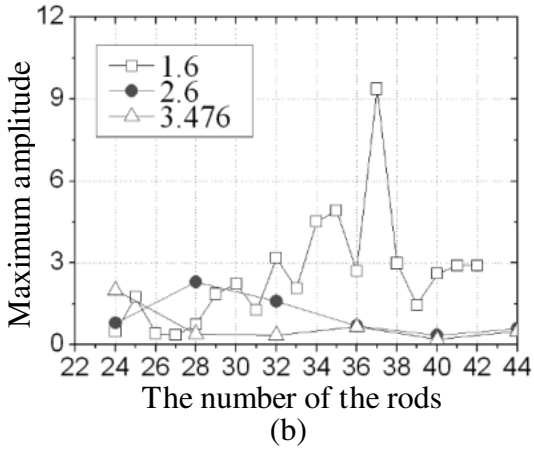

(b)

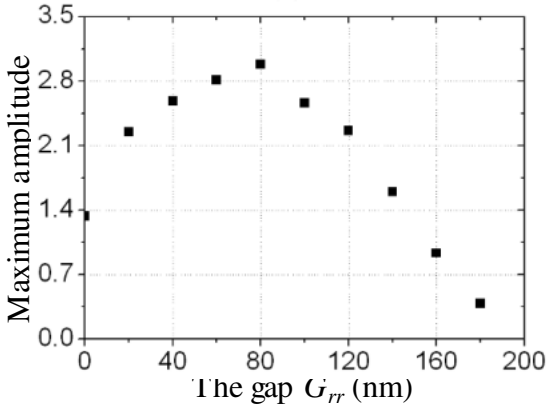

(c)

Figure 3.14: the maximum amplitude inside the ring versus the number of the rods (a) with different R_{rod} (n_r = 1.6); (b) with different refractive indices (R_{rod} = 100 nm); and (c) the maximum amplitude inside the ring versus the gap G_{rr} (R_{rod} = 100 nm, n_r = 1.6).

3.3.3 The 3D optical field distribution

When the structures have a limited height but are symmetric to the *xy*-plane (z = 0), the optical field distribution is same as previous presentation as shown in Figure 3.15(a). In the *yz*-plane (x = 0), the optical field is also symmetric to *xy*-plane (z = 0). In this case, the field has maximum amplitude in the same plane as shown in Fig. 3.15 (b) and has no linear momentum in z direction. Assuming a particle has a small displacement from this plane, the gradient force will draw it back, like what happens in optical trapping. This means the generated optical field can stably trap small particles. The scattering light has a divergent angle in the vertical (z) direction due to the small height (400 nm), and the divergent angle can be reduced by increasing the height.

More details for the 3D optical field distribution and nano particle trapping will be discussed in the next chapter.

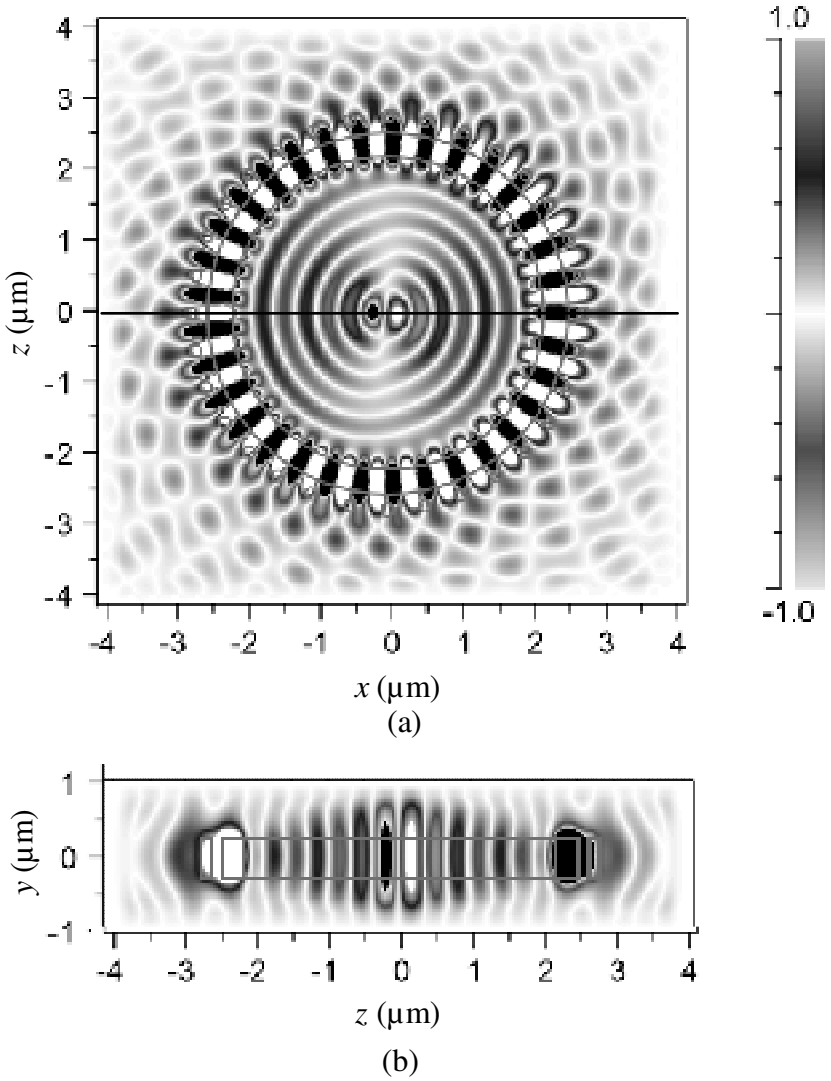

Figure 3.15: H_z field contour map of the 3D simulation (a) cross section view at $z = 0$; and (b) cross section view at $x = 0$ for $l = 1$.

3.4 Summary

An angular momentum generator consisting of a ring resonator, a waveguide and a group of nano-rods is designed, theoretically analyzed and numerically simulated. The effects of the nanorod for light coupling are discussed firstly. A nanorod in between the waveguide and the ring increases the coupling coefficient, and affects the circulating light intensity inside the ring. Then, the generation of angular momentum is theoretically analyzed and numerically simulated. The theoretical analysis and numerical results show that a series of l-order ROFs are generated when different resonant wavelengths are coupled into the generator. The order number of the generated ROFs is equal to the difference between n and N ($l = |n - N|$). Except the 0-order ROF, all other ROFs have angular momenta but no linear momenta along the axis of rotation. The rotation direction is opposite to the light circulation direction when $n < N$, and they are same when $n >$ N. Finally, the generation efficiency, the nanorod effects for generation, and the 3D optical field distribution are discussed. The generation efficiency is affected by the wavelength, the number of rods, as well as the refractive index. The number and the diameter as well as the locations of these nanorods have an optimized value to achieve the highest generation efficiency. The maximum amplitude of generated fields could be 10 times higher than that of the input field. The angular momentum generator overcomes the complication of linear momentum to the rotation of the small particles and provides a compact and flexible platform to study the rotational behaviors in micro-scale.

CHAPTER 4

OPTICAL FORCE, POTENTIAL AND TORQUE FOR NANO-PARTICLE TRAPPING AND ROTATION

An angular momentum generator is successfully designed for the rotating optical field (ROF) generation in last chapter. The principles, the optical field distributions, as well as the generation efficiencies are clearly illustrated. However, when a small object is put into the generated ROFs, the behaviors of it cannot be obtained directly from the field distributions. In order to judge its mechanical behaviors, the resultant force, the potential energy as well as the torque on it are the three necessary parameters. When a particle is significantly smaller than the wavelength, the particle is simplified as a dipole in the optical field. Thus, the force distributions, optical potentials and the optical torques associated with the generated ROFs becomes an interesting topic for nanoparticle trapping and rotation.

In this chapter, the optical force distributions, the optical potential, and the optical torque of generated ROFs are derived by using the Maxwell stress tensor firstly. Then, the corresponding numerical results are illustrated. Finally, the effects of the different shapes of the nano-objects (e.g. nanoparticle, nanowire, and nanorotor) as well as the effects of the angular order are calculated and discussed.

4.1 Theoretical analysis

The designed nano-motor consists of an angular momentum generator (AMG) and a nano-rotor, which is a totally released nano-rod and laid at the central area as shown in Fig. 4.1. This AMG can produce a rotating optical field (ROF) at the central area, which

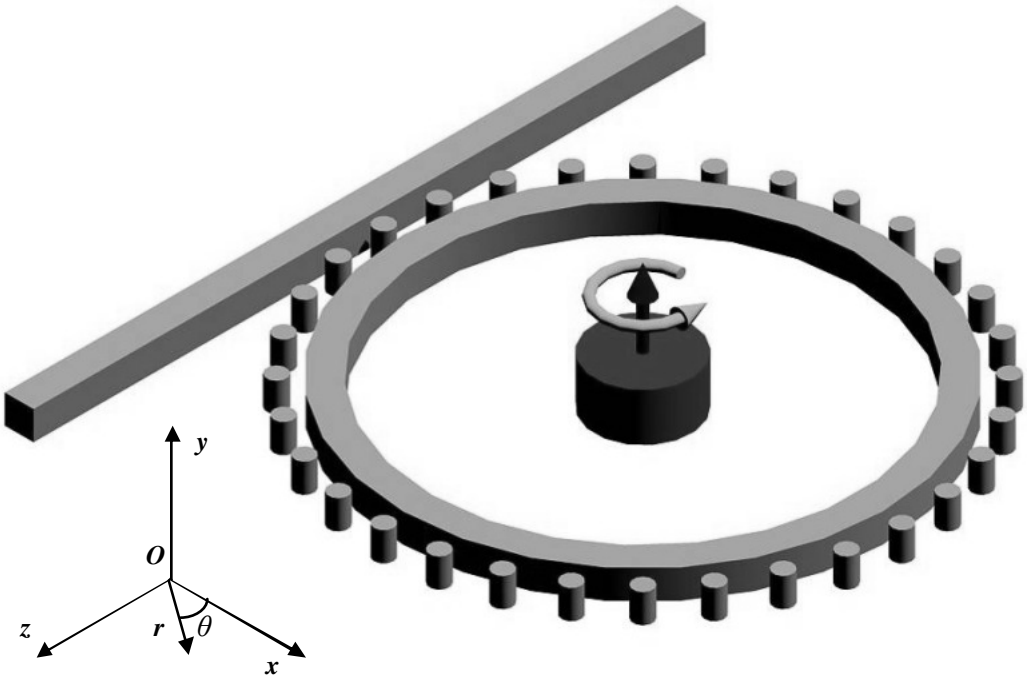

Figure 4.1: Schematic of the nano-rotor at the central of the angular momentum generator.

has been discussed in last chapter. The ROF generates optical forces and optical torques on the nano-rotor due to the rotation of the optical field distribution. When the angular orders are different, the generated ROFs are different. The angular order is equal to the difference between the order of whispering gallery mode (WGM) (n) and the number of the surrounding rods (N) (i.e. $l = |n - N|$). For each ROF, the optical forces and optical

torques are associated with the radius, the height and the refractive index of the nano-rotor. When the nano-rotor is put into the ROF, it can be treated as a group of point charges being put into the ROF, and then the Lorentz force on each tiny volume is produced. The nano-rotor is not only driven by the optical force, but also reforms the ROF due to the change of the refractive index distribution. When the nano-rotor is replaced by a nano-particle with diameter of several nanometers, the effects on the ROF become negligible. The behavior of the nano-particle can be predicted by the optical potential distribution.

The theoretical analysis of the optical force distribution and optical torque on the nano-rotor, as well as the optical potential is presented in this section. This theory is derived by using the Lorentz force law and the Maxwell's equations.

4.1.1 Optical force distributions

For a unit volume with unknown charge distribution, the force obeys the Lorentz force law. Based on the Gauss's law $\nabla \cdot \vec{E} = \frac{\rho}{\varepsilon_0}$ and Ampère's circuital law $\nabla \times \vec{B} = \mu_0 \vec{J} + \mu_0 \varepsilon_0 \frac{\partial \vec{E}}{\partial t}$, and the optical force can be expressed as

$$\vec{f} = \rho \vec{E} + \vec{J} \times \vec{B} = \varepsilon_0 \left(\nabla \cdot \vec{E}\right) \vec{E} + \frac{1}{\mu_0} \left(\nabla \times \vec{B}\right) \times \vec{B} - \varepsilon_0 \frac{\partial \vec{E}}{\partial t} \times \vec{B}, \tag{4.1}$$

where $\vec{E}$ is the electric field, $\vec{B}$ is the magnetic induction, which is related to $\vec{H}$ by the relationship of $\vec{B} = \mu \vec{H}$, μ and μ_0 are the magnetic permeability of material and vacuum, respectively.

Based on the product rule and the Faraday's law $\nabla\times\vec{E}=-\frac{\partial\vec{B}}{\partial t}$, the Poynting vector derivation of time can be expressed as

$$\frac{\partial}{\partial t}\left(\vec{E}\times\vec{B}\right)=\frac{\partial\vec{E}}{\partial t}\times\vec{B}+\vec{E}\times\frac{\partial\vec{B}}{\partial t}=\frac{\partial\vec{E}}{\partial t}\times\vec{B}-\vec{E}\times\left(\nabla\times\vec{E}\right). \tag{4.2}$$

Based on the Gauss's law for magnetism $\nabla\cdot\vec{B}=0$, the force can be expressed as

$$\vec{f}=\varepsilon_0\left[\left(\nabla\cdot\vec{E}\right)\vec{E}-\vec{E}\times\left(\nabla\times\vec{E}\right)\right]+\frac{1}{\mu_0}\left[\left(\nabla\cdot\vec{B}\right)\vec{B}-\vec{B}\times\left(\nabla\times\vec{B}\right)\right]-\varepsilon_0\frac{\partial}{\partial t}\left(\vec{E}\times\vec{B}\right). \tag{4.3}$$

Combined with the curl identity, $\nabla A^2/2=\vec{A}\times\left(\nabla\times\vec{A}\right)+\left(\vec{A}\cdot\nabla\right)\vec{A}$, the force is rewritten as

$$\vec{f}=\varepsilon_0\left[\left(\nabla\cdot\vec{E}\right)\vec{E}+\left(\vec{E}\cdot\nabla\right)\vec{E}\right]+\frac{1}{\mu_0}\left[\left(\nabla\cdot\vec{B}\right)\vec{B}+\left(\vec{B}\cdot\nabla\right)\vec{B}\right]-\frac{1}{2}\nabla\left(\varepsilon_0E^2+\frac{1}{\mu_0}B^2\right)-\varepsilon_0\frac{\partial}{\partial t}\left(\vec{E}\times\vec{B}\right). \tag{4.4}$$

To simplify Eq. (4.4), the Maxwell stress tensor is introduced as

$$T_{ij}\equiv\varepsilon_0\left(E_iE_j-\frac{1}{2}\delta_{ij}E^2\right)+\frac{1}{\mu_0}\left(B_iB_j-\frac{1}{2}\delta_{ij}B^2\right), \tag{4.5}$$

where ε_0 and μ_0 are the permittivity and permeability of the vacuum respectively, δ_{ij} is Kronecker's delta. The force is simplified as

$$\vec{f}=\nabla\cdot\vec{\vec{T}}-\varepsilon_0\mu_0\frac{\partial\vec{S}}{\partial t}. \tag{4.6}$$

For convenience, the first term $(\nabla\cdot\vec{\vec{T}})$ is defined as $\vec{F}_g$ (i.e. $\nabla\cdot\vec{\vec{T}}\equiv\vec{F}_g$), and the second term ($\varepsilon_0\mu_0\frac{\partial\vec{S}}{\partial t}$) is caused defined as $\vec{F}_r$, which represents the change of energy flux.

Integrating the force per unit volume on the nano-rotor, the total force is given by

$$\vec{F}_{total} = \iiint_V \vec{f} dV = \iiint_V \left(\nabla \cdot \vec{T} - \frac{1}{c^2} \frac{\partial \vec{S}}{\partial t} \right) dV, \tag{4.7}$$

where V is the rotor's volume. Appling the divergence theorem, the total force can be written as

$$\vec{F}_{total} = \iint_a \vec{T} \cdot \vec{n} da - \frac{1}{c^2} \frac{\partial}{\partial t} \iiint_V \vec{S} dV, \tag{4.8}$$

where $\vec{n}$ is the normal vector of the rotor's surface, a is the surface area, da is the differential surface area. The first term is the integrated shear stress and pressure at the surface of the rotor, and the second is the optical momentum change rate in the rotor.

4.1.2 Optical potential and particle trapping

A nano-particle at an arbitrary point in the ROF corresponds to an optical force and these optical forces at all points form a force field. The nano-particle in this force field carries a potential energy, U, which is named 'optical potential'. The work done by the optical force, W, is equal to the change in potential energy, which can be expressed as

$$W = -\Delta U \tag{4.9}$$

where the sign of minus indicates that the positive work corresponds to the decrease in optical potential. When a nano-particle moves along a path C, the work done by the optical force (W) can be expressed as

$$W = \int_C \vec{f} \cdot d\vec{r}, \tag{4.10}$$

where $\vec{r}$ is the displacement from the starting point to the ending point.

Assuming the optical potential at the origin is zero, the optical potential at each point can be expressed as

$$U(r,\theta,y)=\int_C \vec{f}\cdot d\vec{r}, \tag{4.11}$$

where *r, θ, y* are the three coordinates in the cylindrical coordinate system, and the ending point is the origin. For the conservative force field, the optical potential is independent of the path, but depends on the starting and ending force. This property is useful to simplify the numerical simulation by choosing particular path.

The optical potential determines the mechanical behavior of a nano-particle inside the ROF. The nano-particle is driven to the local minimums in the optical potential by optical force, and will stop at these local minimums points or oscillate around them. The potential gradient around these local minimums determines the trapping capability of the ROF.

4.1.3 Optical torque

The corresponding torque $\vec{\tau}$ can be expressed as

$$\vec{\tau}=\vec{r}\times\vec{f}=\vec{r}\times\left(\nabla\cdot\vec{\vec{T}}\right)-\frac{1}{c^2}\vec{r}\times\frac{\partial\vec{S}}{\partial t}, \tag{4.12}$$

where $\vec{r}$ is the displacement vector (from the axis of the rotor to the considered point), *t* is time, and *S* is the Poynting vector.

The total torque $\vec{\tau}_{total}$ on the rotor is expressed as

$$\vec{\tau}_{total} = \iiint_V \vec{\tau}\, dV \tag{4.13}$$

where the value of torque $\vec{\tau}$ is a time-dependent. When the rotor is a cylinder and the center is same as the origin (i.e. ring's geometrical center), the total torque ($\vec{\tau}_{total}$) becomes time independent due to the ROF's rotational symmetry.

4.2 Numerical simulation results and discussions

Finite difference time domain (FDTD) method is used for numerical simulations of optical fields. The AMG has height of 0.4 μm, rings' external radius of 2 μm, rings' width of 0.45 μm, refractive index of 2, nano-rods number of 28, nano-rods radius of 0.1 μm, nano-rods-ring gap of 0.08 μm. The waveguide is replaced by a light source in the ring by assuming the light coupling is at critical coupling conditions [141]. A cylinder nano-rotor with radius of 0.5 μm, refractive index of 2, height of 0.4 μm, is put at the geometric center of the ring resonator, i.e., the ring and the nano-rotor has same geometric center. This center is also set as the origin of the Cartesian coordinate system, and the ring lays on the xz-plane. The axis of the nano-rotor is same as the *y* axis, as well as the longitudinal axis of a cylindrical coordinate system. All simulations are based on input light with TE-mode.

4.2.1 Optical force distributions

The electric field distributions and magnetic field distributions of the generated ROF are the fundament for the optical force calculation. When the input light is TE-mode, (i.e. $E_x \neq 0$, $H_y \neq 0$, $E_y = E_z = H_x = H_z = 0$), the generated ROF (e.g., angular order l =1, i. e. 1-fold symmetric optical field, and anticlockwise rotation) at central area has electric and the magnetic field distributions as shown in Fig. 4.2. It can be seen that the generated

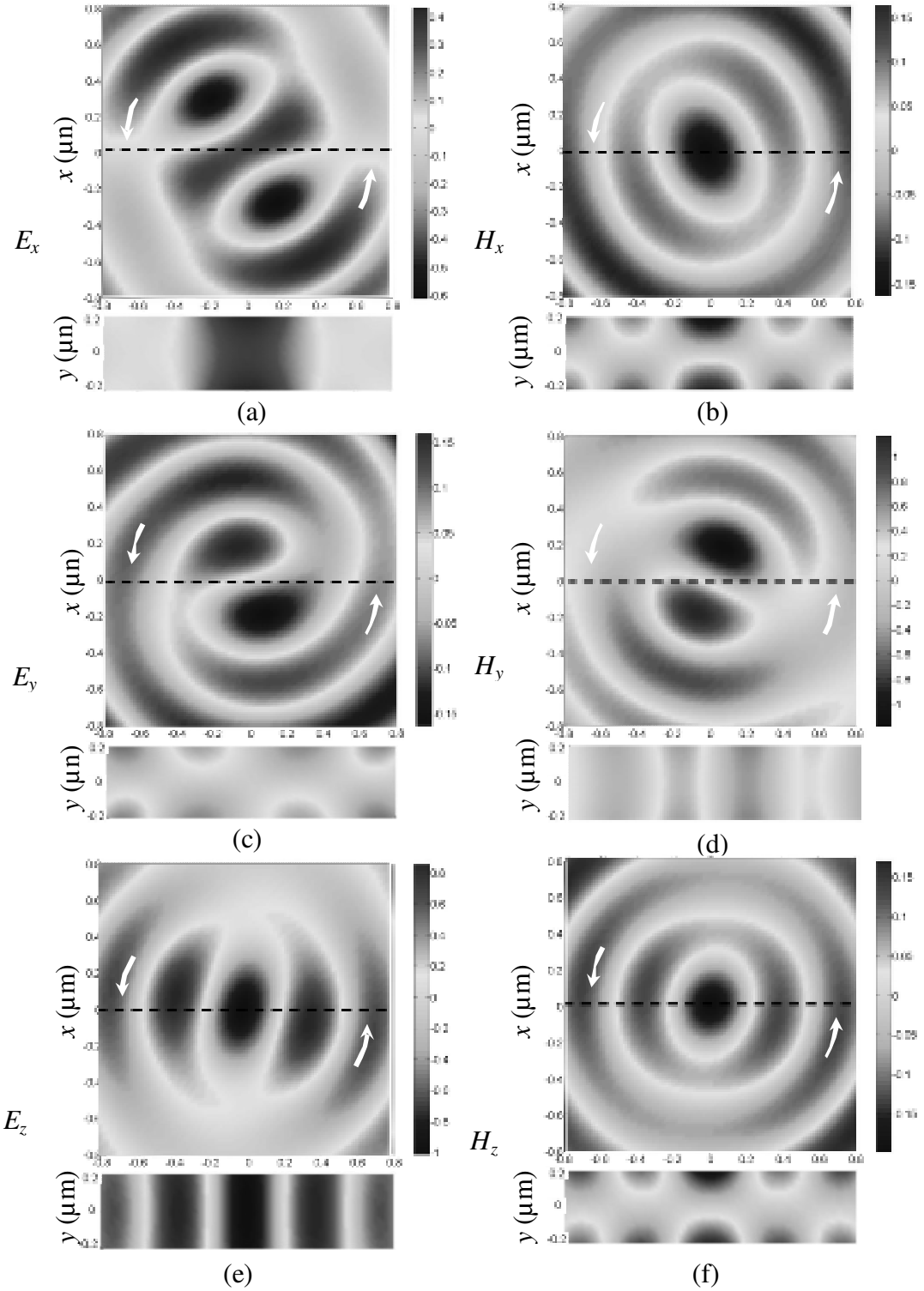

Figure 4.2: (a) E_x; (d) H_y; (e) E_z distributions in the *xz*-plane (y = 0 μm) and *zy*-plane (x = 0); and (b) H_x; (c) E_y; (f) H_z distributions in the *xz*-plane (y = 0.2 μm) and *zy*-plane (x = 0).

ROF has electric field not only in x direction, but also in y, and z directions; has magnetic field not only in y direction, but also in x and z directions. This is caused by the propagating mode transformation on the waveguide and the ring of the AMG. However, the electric field has larger amplitude in x and z directions than it in y direction (i.e. $E_x > E_y$ and $E_z > E_y$). The magnetic field has larger amplitude in y direction than it in x and z directions (i.e. $H_y > H_x$ and $H_y > H_z$), which means that the linear polarization corresponding to the TE-mode still dominates this ROF generation process. In other words, when the input light has TE-mode, the ROF can be characterized by E_x, E_z and H_y. On the other hand, the generated has an anticlockwise rotation, and its rotation frequency is same as the frequency of the input light (i.e. $f_r = f$).

The optical force is calculated based on Eq. (4.6) and the electric and magnetic field distributions. The Poynting vector $\vec{S}$ is involved in right side expression of Eq. (4.6). On the other hand, the Poynting vector also represents the energy flux or optical intensity of the generated ROF. On the Cartesian axes x, y and z, the Poynting vector has three corresponding components of S_x, S_y and S_z. In the xz-plane, the Poynting vector's component ($\vec{S}_{xz}$) is equal to the sum of $\vec{S}_x$ and $\vec{S}_z$ (i.e. $S_{xz} = \left|\vec{S}_{xz}\right| = \sqrt{S_x^2 + S_z^2}$). The contour plots of S_{xz} in the xz-plane at $y = 0$ μm and yz-plane at $x = 0$ μm are shown in Fig. 4.3 (a), in which the arrows indicate the directions of $\vec{S}_{xz}$. It can be seen that the energy flux in the xz-plane has two high value zones in the central area. The energy flows into the central area, change the flowing directions before arriving the origin, and flows out of this area again. S_{xz} has maximum values at $y = 0$ μm, however, the intensity gradient along the y direction is much smaller than it along the x or z direction. The contour plot of

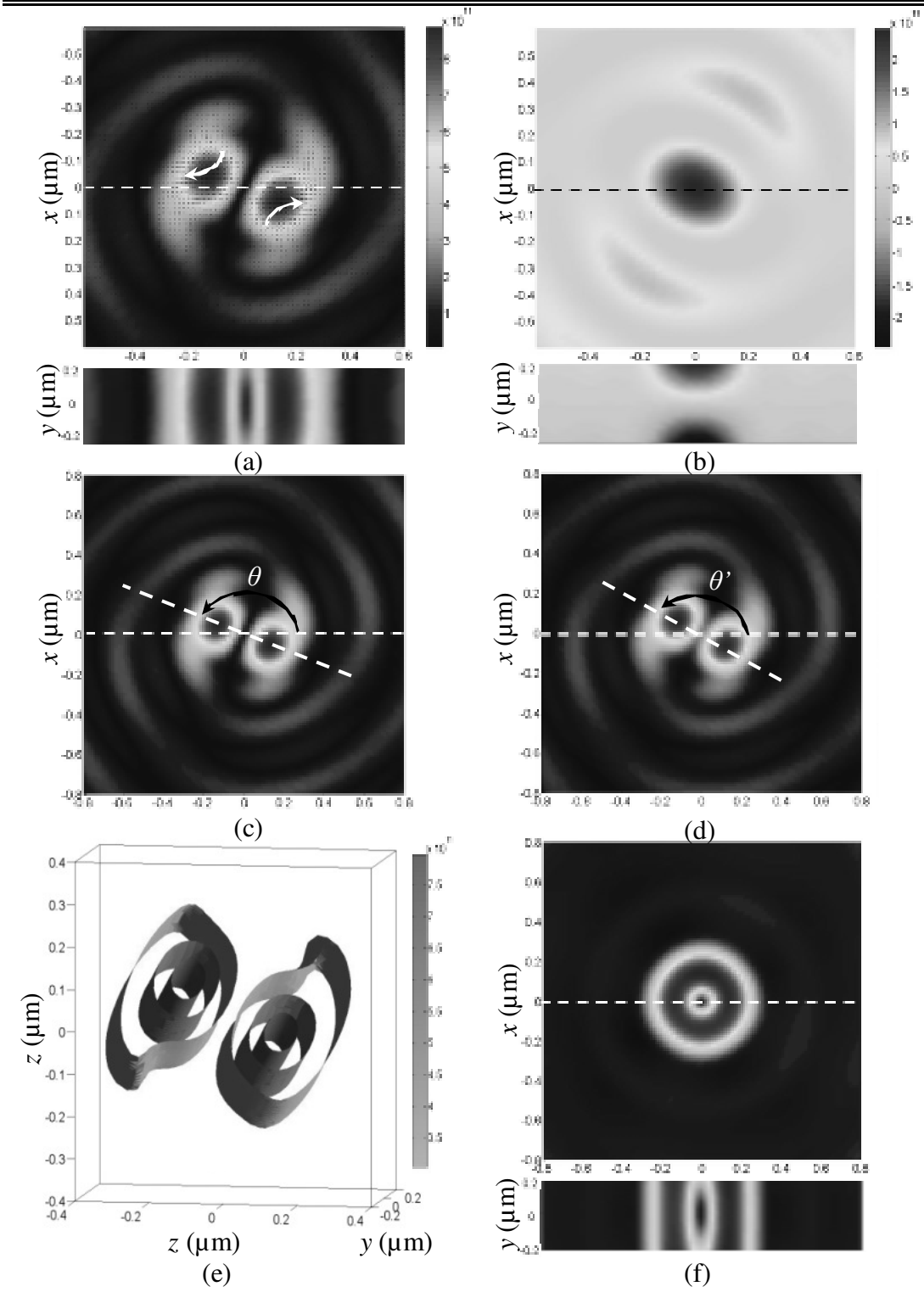

Figure 4.3: The contour plot of (a) S_{xz}; (c) S; (f) S_T in xz-plane at $y = 0$ μm and yz-plane at $x = 0$ μm; (b) S_y in xz-plane at $y = 0.2$ μm and yz-plane at $x = 0$ μm; (d) S in xz-plane at $y = 0.2$ μm; and (g) the isovalue surfaces in the energy flux (S) field.

S_y in xz-plane at y = 0.2 μm and yz-plane at x = 0 μm are shown in Fig. 4.3(b). The S_y represents the energy flux along the y directions. S_y has maximum value at the central of the xz-plane, positive value when y is positive, and negative value when y is negative. This means that the energy flows away from the origin along the y axis, and flow rate is increased when the distance to the origin is increased. The S_y in xz-plane at y = 0 μm is close to zero, which means in this plane, the S_{xz} represents the energy flux totally. The contour plots of Poynting vector's value, S (i.e. $S = |\vec{S}| = \sqrt{S_x^2 + S_y^2 + S_z^2}$), in xz-plane at y = 0 and 0.2 μm are shown in Fig. 4.3 (c) and (d), respectively. It can be seen that the distribution of S at y = 0.2 μm has a phase delay (i.e. the angle between the x axis and the line connected two largest values is satisfy that $\theta > \theta'$) compared to it at y = 0 μm, and the two high value zones are more close. The isovalue surfaces in the energy flux (S) field are shown Fig. 4.3 (e).

The optical fields and the Poynting vector at certain time are discussed in above two paragraphs. In one rotation period, the amplitude of the Poynting vector (S_T) can well represents the energy flux. The contour plot of S_T in xz-plane at y = 0.2 μm and yz-plane at x = 0 μm are shown in Fig. 4.3 (f). It can be seen that in this period, the Poynting vector (i.e. energy flux or optical intensity) has larger values in a cylinder which has radius of 200 nm and has axis as y axis than in other areas. The unit of the Poynting vector is W/m^2 when the input light is 1 W.

The first term (F_g) and the second term (F_r) of Eq. (4.6) are discussed separately. On the Cartesian axes x, y and z, the F_r has three corresponding components of $F_{r,x}$, $F_{r,y}$

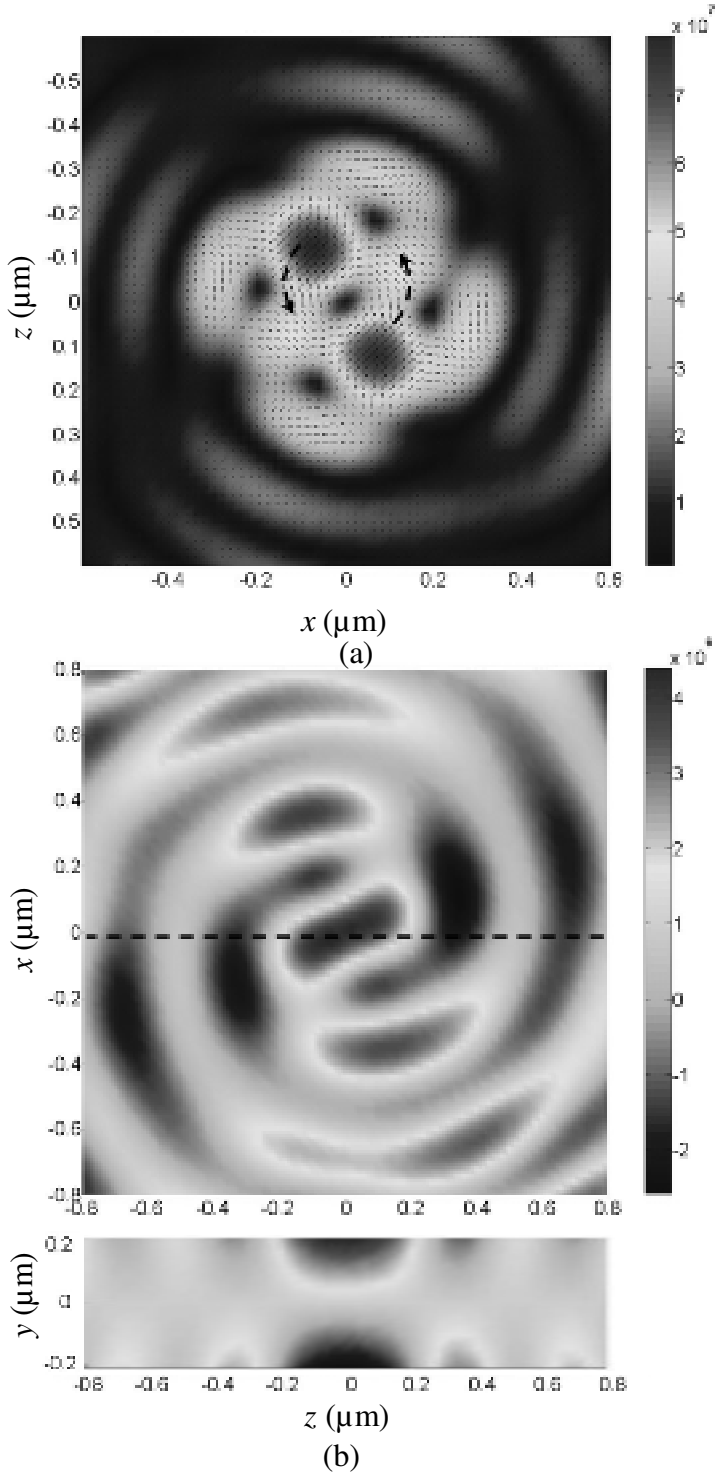

Figure 4.4: The contour plot of (a) $F_{r,xz}$ in xz-plane at $y = 0$ μm; and (b) $F_{r,y}$ in xz-plane at $y = 0.2$ μm and yz-plane at $x = 0$ μm.

and $F_{r,z}$. In the *xz*-plane, the component of F_r ($\vec{F}_{r,xz}$) is equal to the sum of $\vec{F}_{r,x}$ and $\vec{F}_{r,z}$ (i.e. $F_{r,xz} = \left|\vec{F}_{r,xz}\right| = \sqrt{F_{r,x}^2 + F_{r,z}^2}$). The contour plot of $F_{r,xz}$ in *xz*-plane at $y = 0$ μm is shown in Fig. 4.4 (a). The optical force F_r in the *xz*-plane, which push a small particle to rotate along the anticlockwise direction (same as the rotation direction of the ROF) around the *y* axis. The contour plots of $F_{r,y}$ in *xz*-plane at $y = 0.2$ μm and *yz*-plane at $x = 0$ μm are shown in Fig. 4.4 (b) and (c) respectively. $F_{r,y}$ represents the force along the *y* axis. It has positive value when $y > 0$ and negative value when $y < 0$, which states that the origin is not a stable mechanic equilibrium point, and the force field tends to draw a particle away. Compared to the maximum value of $F_{r,xz}$, the maximum value of $F_{r,y}$ is one order of magnitude smaller, which means $F_{r,xz}$ dominates the F_r field. As discussed in the section 4.1.1, the optical force is associated with the input power and the target volume. The normalized optical force density is used to replace the optical force in numerical simulation, which is equal to the optical force divided by the input power and the volume of object. The normalized optical force density is 10^{-6} pNW^{-1}μm^{-3}. The numerical results show that the maximum F_r (for convenience, F_r also presents normalized optical force density) is 77 pNW^{-1}μm^{-3}.

Similarly, the F_g has three corresponding components of $F_{g,x}$, $F_{g,y}$ and $F_{g,z}$ on the Cartesian axes *x*, *y* and z, and the contour plot of $F_{g,xz}$ (i.e. $F_{g,xz} = \left|\vec{F}_{g,xz}\right| = \sqrt{F_{g,x}^2 + F_{g,z}^2}$) in *xz*-plane at $y = 0$ μm is shown in Fig. 4.5 (a). It can be seen that the F_g is proportional to the gradient of the optical intensity (represented by the Poynting vector), and tends to attract a small particle to the region of highest intensity as indicated by the black arrows.

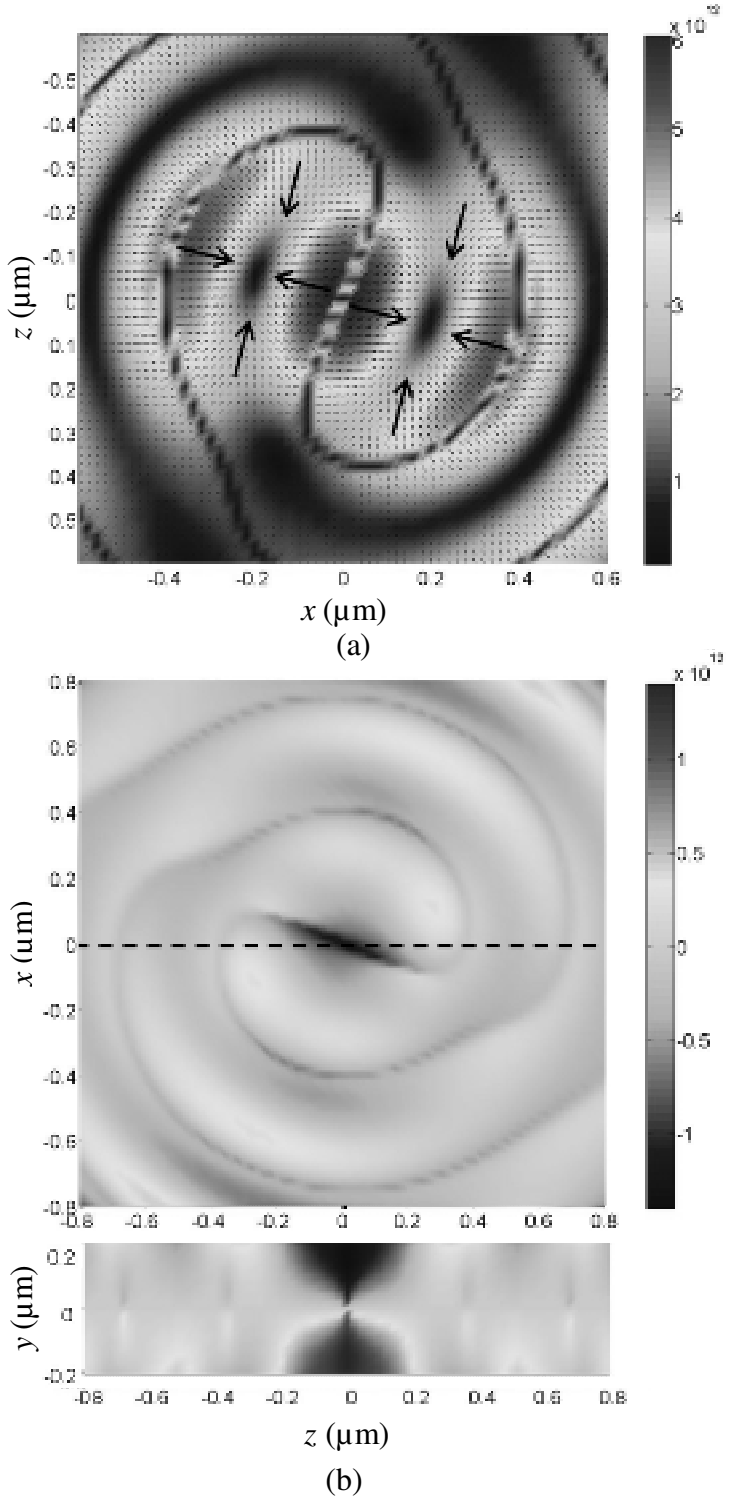

Figure 4.5: The contour plot of (a) $F_{g,xz}$ in xz-plane at y = 0 μm; and (b) $F_{g,y}$ in xz-plane at y = 0.2 μm and yz-plane at x = 0 μm.

The contour plots of $F_{g,y}$ in xz-plane at $y = 0.2$ μm and yz-plane at $x = 0$ μm are shown in Fig. 4.5 (b). $F_{g,y}$ is positive when $y < 0$ and negative when $y > 0$, which means the force field tends to draw a particle back the origin when the particle is displaced an arbitrarily small distance from the origin. Compared to the maximum value of $F_{g,y}$, the maximum value of $F_{g,xz}$ is 5 times higher, which means that $F_{g,xz}$ dominates F_g field. The numerical results show that the maximum F_g is 6.1×10^6 $\text{pNW}^{-1}\mu\text{m}^{-3}$.

Compared to F_r, F_g is 6-order of magnitude higher, which means that F_r is negligible in most cases. However, compared to the gravity, F_r and F_g are both large. For instance, the material is silicon nitride (density 3.29 gram/cm^3), then the gravity is equal to 3.2×10^{-2} $\text{pN}\mu\text{m}^{-3}$. In other words, when the input power is 0.05 μW, F_g approximates to the gravity, and when the input power is 5 mW, F_r approximates to the gravity.

The optical force distributions of the special ROF (angular order $l = 1$, and nothing inside) is illustrated and discussed. Several important conclusions are listed at here. Firstly, the ROF can be characterized by E_x, E_z and H_y. Secondly, the Poynting vector (i.e. energy flux or optical intensity) has larger values in a cylinder which has radius of 200 nm and has axis as y axis than in other areas. Thirdly, F_g is 6-order of magnitude higher than the F_r, and the F_g is close to the gravity when the input power is around 0.05 μW. In the following, the effects of the nano-rotor and the angular order are discussed.

4.2.1.1 The effects of the nano-rotor

When there is a nano-rotor at the central of the ring resonator, the generated ROF is affected. For instance, the nano-rotor has refractive index of 2 (Si_3N_4) and radius of 0.5 μm, then the corresponding distributions of E_x, H_y, E_z and S_T in the xz-plane

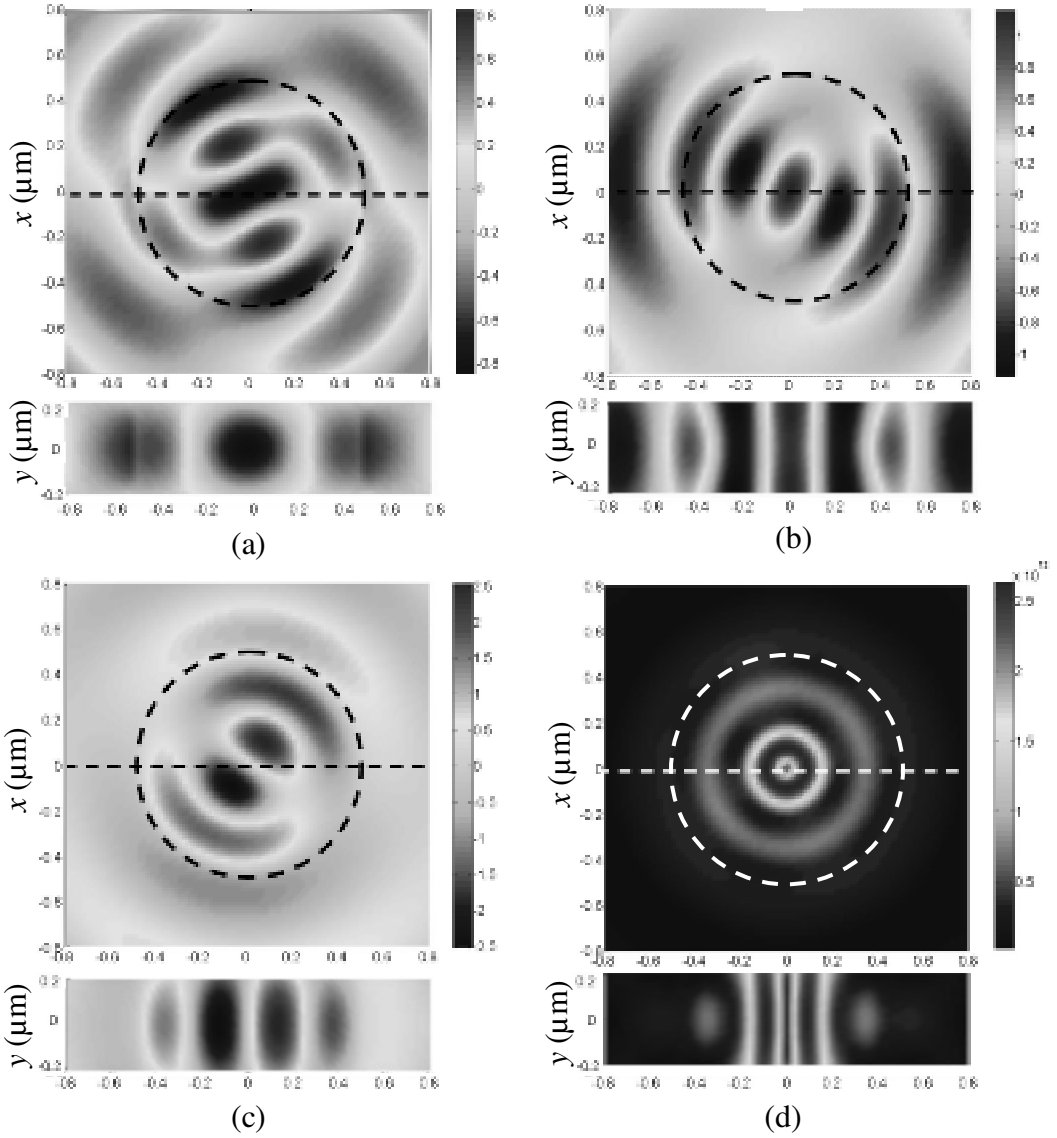

Figure 4.6: (a) E_x; (b) H_y; (c) E_z; and (d) S_T distribution in the xz-plane at y = 0 μm and the yz-plane at x = 0 μm.

at y = 0 μm and the yz-plane at x = 0 μmare shown in Fig. 4.6 (a), (b), (c) and (d), respectively. Compare the ROF with the nano-rotor to the ROF without the nano-rotor, the maximum values of E_x, H_y, E_z and S_T are enlarged, the space between two

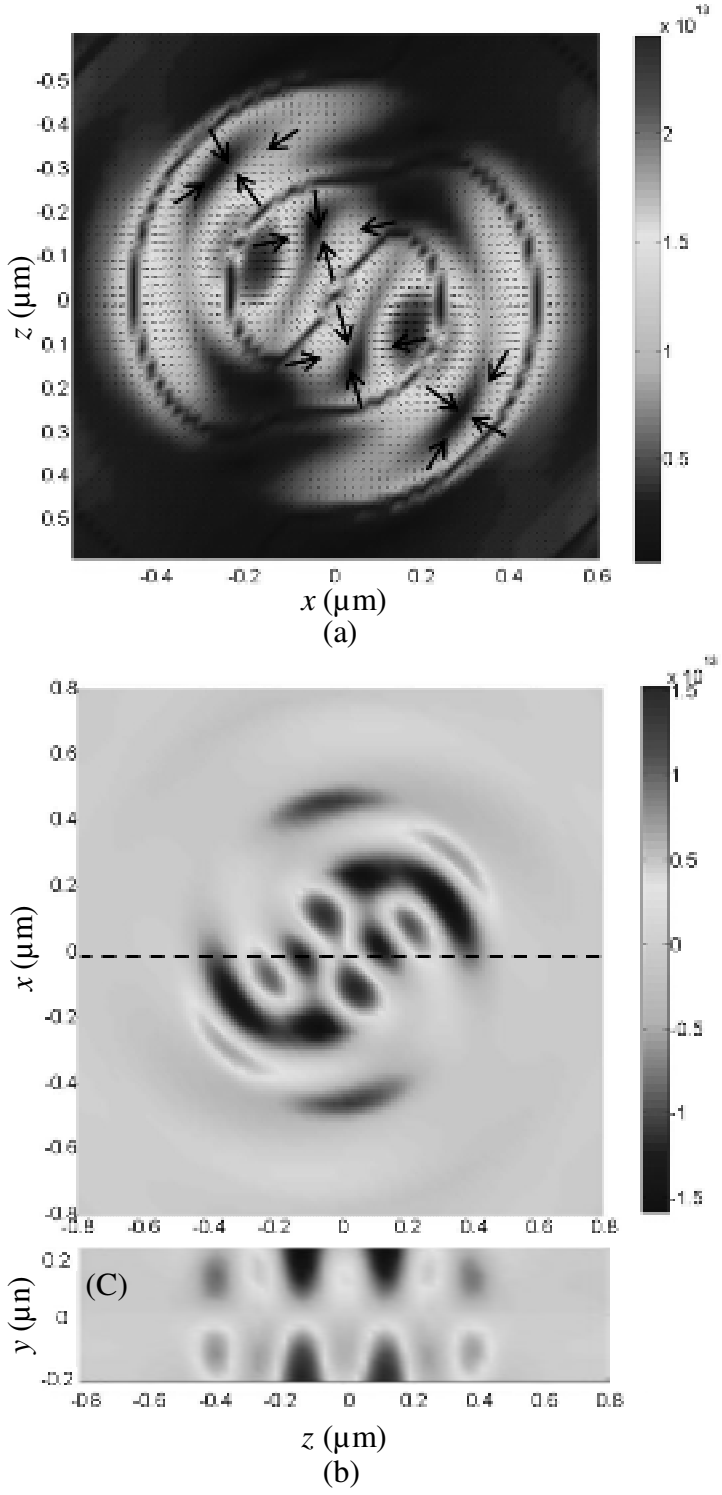

Figure 4.7: The contour plot of (a) $F_{g,xz}$ in xz-plane at y = 0 μm; and (b) $F_{g,y}$ in xz-plane at y = 0.2 μm and yz-plane at x = 0 μm.

neighboring radial maximums of E_x, H_y and E_z are decreased, the gradient of E_x, H_y, E_z and S_T along the y-axis is increased, and the radius of the cylinder, in which the Poynting vector (i.e. energy flux or optical intensity) has larger values, is decreased from 200 nm to 180 nm. The optical force (F_g) field corresponds to the ROF with nano-rotor is also varied as shown in Fig. 4.7. It can be seen that the maximum of F_g is increased to 2.48×10^7 $pNW^{-1}\mu m^{-3}$. That means the optical force draws the nano-rotor back or away from the xz-plane at $y = 0$ μm is dependent on the radius of the rotor. For the calculated radius (0.5 μm), the optical force draws the nano-rotor back to the xz-plane at $y = 0$ μm. However, when the central part (i.e., a cylinder with radius of 10 nm) of the nano-rotor is movable, this part is driven away from this plane.

4.2.1.2 The effects of the angular order

The effects of the angular order are discussed without the nano-rotor inside the ROF. As discussed in last chapter, the generated ROF are different when the angular order has different values. One difference is that the l-order ROF has l-fold rotation symmetric field distributions. Here, this difference is not discussed, but the differences of the amplitude distributions of E_{xz}, H_y and S are discussed, where $E_{xz} = (E_x^2 + E_z^2)^{1/2}$. The amplitudes of E_{xz}, H_y and S are equal to the maximum values in one rotation period, and their distributions are directly related to the optical force field.

When the angular order l is equal to zero (i.e. $l = 0$), the amplitude distributions of E_{xz}, H_y and S in the xz-plane at $y = 0$ μm and yz-plane at $x = 0$ μm are shown in Fig. 4.8 (a-c). It can be seen that the amplitude distributions are concentric distributed in the xz-plane at $y = 0$ μm. The amplitude changes along the y-axis of E_{xz} and H_y are small. The

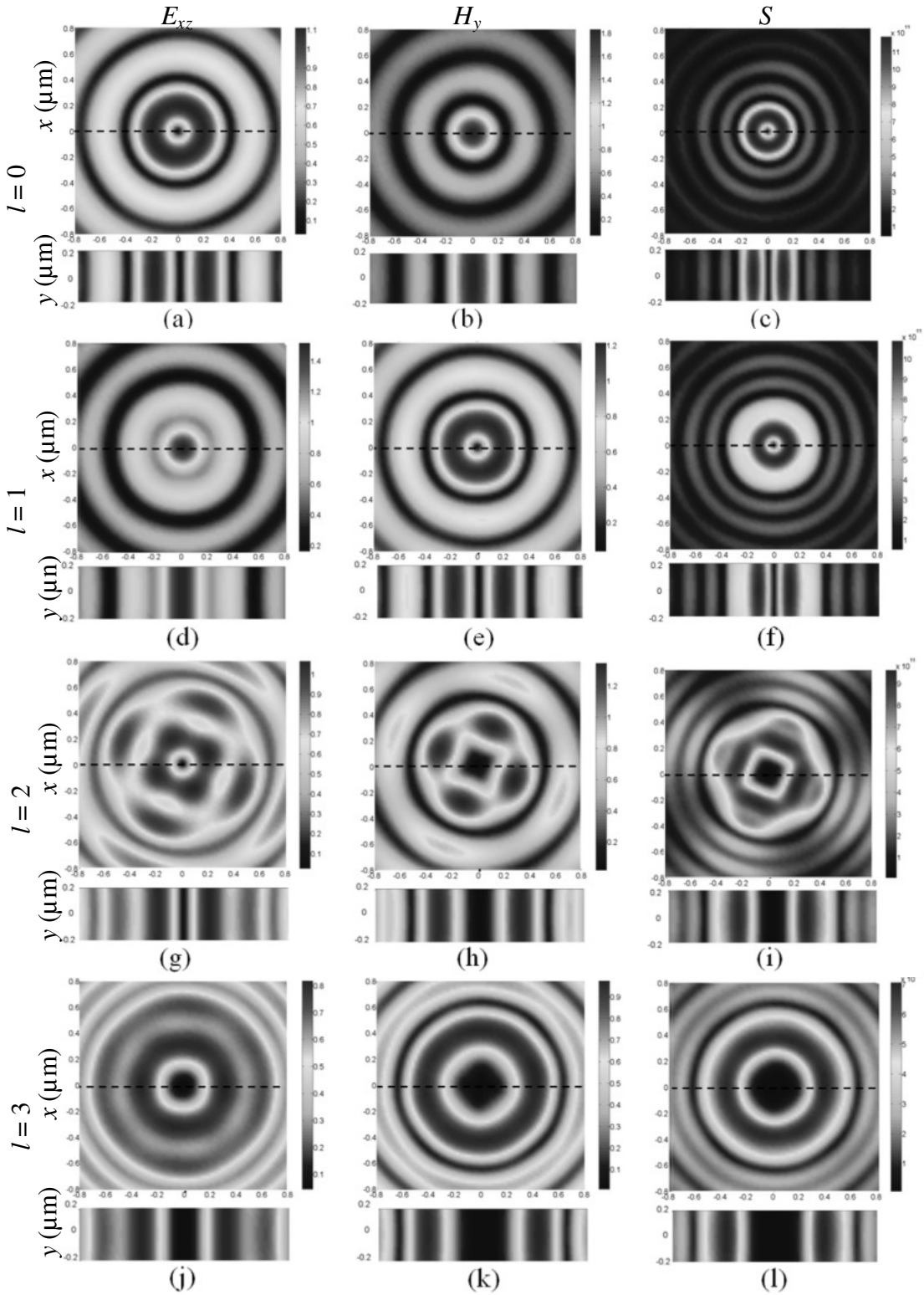

Figure 4.8: The amplitude distributions of E_{xz}, H_y, and S in the xz-plane at $y = 0$ μm and the yz-plane at $x = 0$ μm when (a-c) $l = 0$; (d-f) $l = 1$; (g-i) $l = 2$; and (j-l) $l = 3$.

amplitude of S has maximum values at $y = 0$ μm. As discussed in the last chapter, this angular order (i.e. $l = 0$) is a special case that the generated optical field doesn't have a rotation. Thus, the amplitude distributions of E_{xz}, H_y and S represent the maximum values of E_{xz}, H_y and S in an input light's period.

The amplitude distributions of E_{xz}, H_y and S are shown in Fig. 4.8 (d) – (f) at $l = 1$, Fig. 4.8 (g) – (i) at $l = 2$, and Fig. 4.8 (j) – (l) at $l = 3$. It can be seen that when the angular order l is increased, the central area without optical field is enlarged, e.g., the central area is a cylinder with radius of 10 nm at $l = 1$, and is enlarged to a cylinder with radius of 200 nm at $l = 3$, as shown in Fig. 4.8 (f) and (l), respectively. The amplitude at arbitrary point represents the maximum value in a rotation period. In other words, the iso-amplitude curves of the amplitude distribution in the xz-plane at $y = 0$ μm is a series of concentric circles when the optical field distributions doesn't vary versus the time in one rotation period. For instance, the iso-amplitude curves in the distribution of H_y as shown in Fig. 4.8 (e) are close to a series of concentric circles, which means that the H_y distribution as shown in Fig. 4.2 (d) is almost same except the rotation. It also means the maximum optical field at r in Fig. 4.2 (d) is equal to the value of the amplitude at r in Fig. 4.8 (e). Thus, the concentric liked amplitude distribution represents the generated ROF is timely stable. When the angular order $l = 1$ and 3, the corresponding ROFs are timely stable as shown in Fig. 4.8. However, not all the generated ROFs have the concentric liked amplitude distribution. For instance, the iso-amplitude curves in the distribution of E_{xz}, H_y and S as shown in Fig. 4.8 (g) – (i) are close to rectangles rather than circles, which mean that the optical field distributions has four weak-strong circles in one rotation period. That is to say the maximum value of the generated ROF

at r is

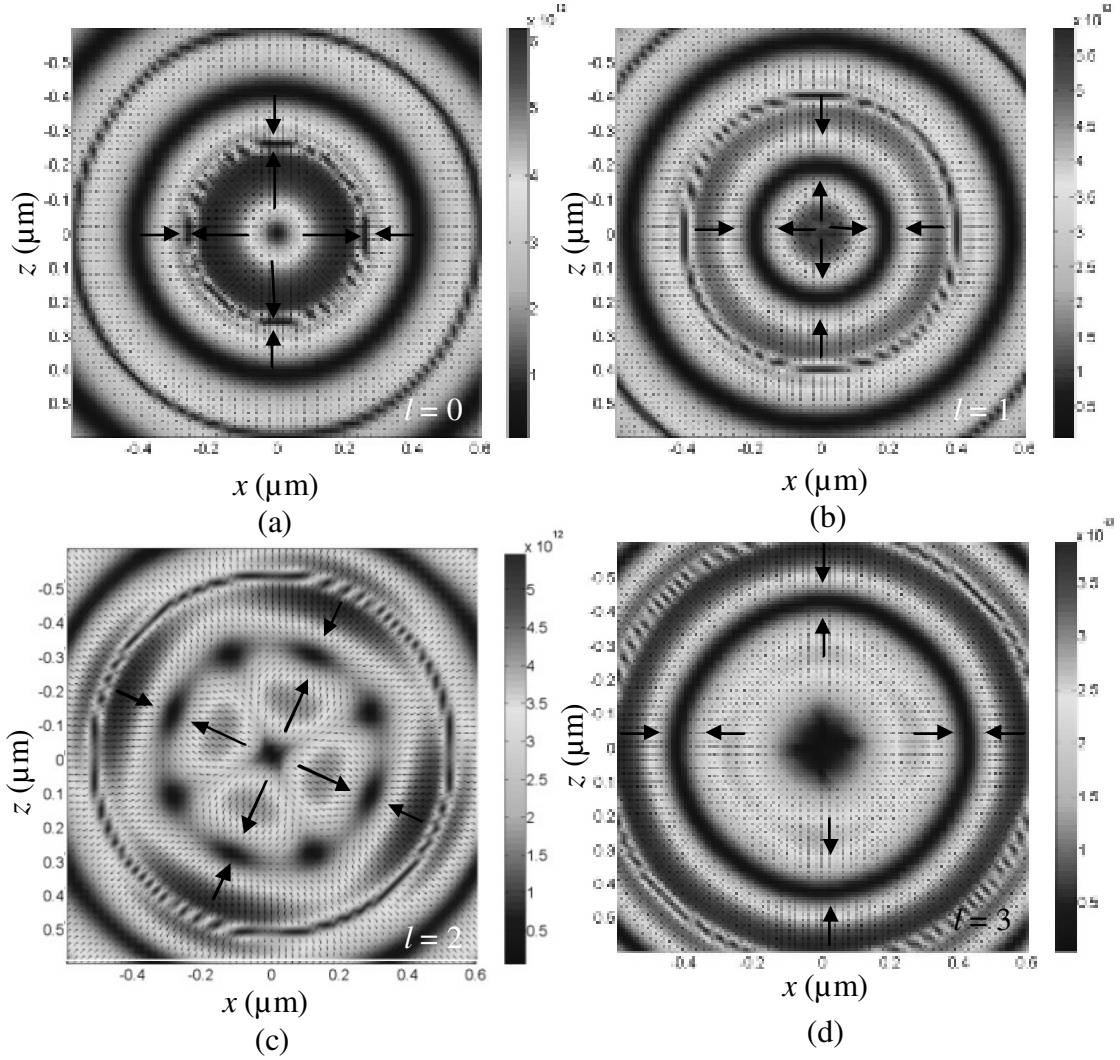

Figure 4.9: The resultant force distributions in the *xz*-plane at $y = 0$ μm when (a) $l = 0$; (b) $l = 1$; (c) $l = 2$; and (d) $l = 3$.

varied from small to large and large to small four times in a rotation period (i.e. $T_r = 1/f_r$). The reason caused this variation is the backscattering. The nano rods around the ring resonator in the AMG not only scatter the light into the central area, but also scatter the light into the ring resonator. In the ring resonator, another circulating light appears which

has opposite travelling direction compared to the original circulating light. We call the original circulating light has a forward propagation, and then the new circulating light has a backward propagation. The corresponding scattering is the backscattering. When the backward circulating light is strong enough, its evanescent field also scattered by the nano rods around the ring resonator, and another ROF is generated. The new ROF has opposite rotation direction compared to the original ROF. These two ROFs are interfered in the central space. They both have 2-fold rotational symmetry, and the optical field distributions in *xz*-plane have four petals. After the interference, the four maximums appear when the positive-positive or negative-negative petals are overlapped, and four minimums appear when the positive-negative petals are overlapped.

The resultant force $\vec{F}_T(r)$ at arbitrary point *r* is defined as

$$\vec{F}_T(r) = \frac{1}{T_r}\int_0^{T_r} \vec{f}(r,t)\,dt. \tag{4.14}$$

Where $\vec{f}(r,t)$ is the optical force which can be calculated by Eq. (4.6), T_r is the rotation period, which is equal to the reciprocal of the rotation frequency (i.e. $T_r = 1/f_r$), t is the time. Usually, the mechanical response time of the nano-particle is much longer that the rotation period, so the effects of optical force on the nano-particle is determined by the resultant force. When the angular order is increased from 0 to 3, the resultant force distribution is varied as shown in Fig. 4.9(a) – (d) correspondingly. It can be seen that when the *l* is increased from 0 to 3, the maximum resultant force in the *xz*-plane at $y = 0$ μm is decreased from 6.2×10^6 $pNW^{-1}\mu m^{-3}$ to 3.8×10^6 $pNW^{-1}\mu m^{-3}$.

The resultant force is proportional to the gradient of the optical intensity (represented by the Poynting vector), and tends to push a small particle to the

region with highest light intensity. For instance, when $l = 3$ the amplitude distribution of S as shown in Fig. 4.8 (u) indicates that the intensity in this plane has a maximum value on a circle with radius of 390 nm. Correspondingly, the resultant optical force field tends to push a small particle to the equilibrium circle, which is verified by the resultant force distribution as shown in Fig. 4.9 (d). When the angular order is increased, the radius of the first equilibrium circle is increased (e.g. 213nm at $l = 0$, 181 nm at $l = 1$, 358 nm at $l = 2$ and 380 nm at $l = 3$).

The contour plot of the resultant force in the xz-plane at $y = 0$ μm is a series of concentric circles when the optical force distributions doesn't vary versus the time in one rotation period except the rotation. For instance, the contour plot of the resultant force as shown in Fig. 4.9 (b) is a series of concentric circles, which means that the optical force (represented by F_g) distribution as shown in Fig. 4.5 (a) is almost same except the rotation. Similarly, due to the backscattering, when $l = 2$, the contour plot of the resultant force in the xz-plane at $y = 0$ μm has 2-fold rotational symmetry, as shown in Fig. 4.9 (c).

4.2.2 Optical potential and particle trapping

The optical potential is calculated based on Eq. (4.13), which represents potential energy carried by a nano-particle. When the angular order $l = 1$, the optical potential in the xz-plane at $y = 0$ μm is shown in Fig. 4.10. The unit of the calculated optical potential is equal to the unit of normalized optical force density ($NW^{-1}m^{-3}$) times the unit of radius (μm), i.e. 10^{-12} $pJW^{-1}\mu m^{-3}$. It can be seen that the optical potential has two local

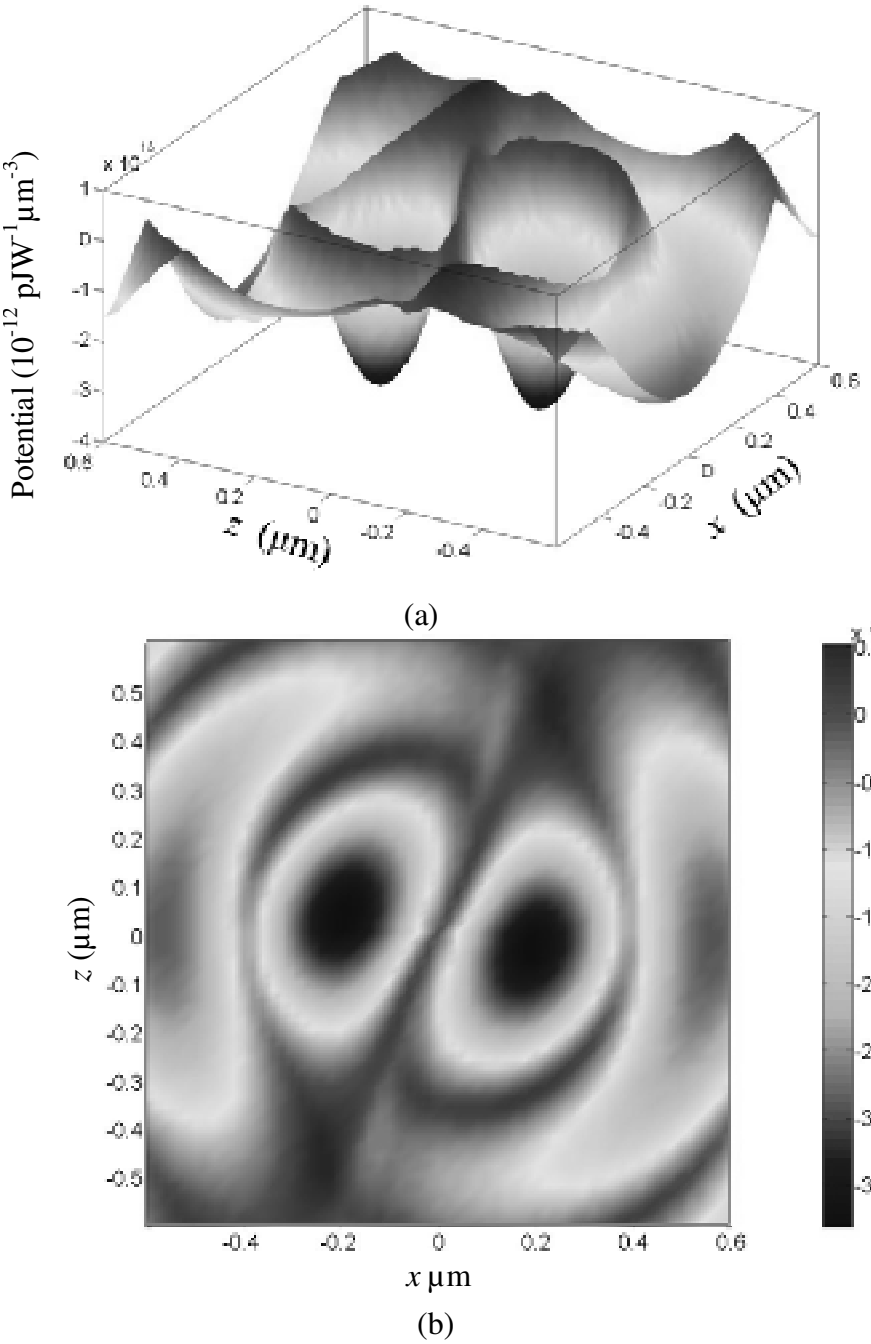

Figure 4.10: (a) The 3D surface; and (b) the contour plot of optical potential in the *xz*-plane when $y = 0$ µm and $l = 1$.

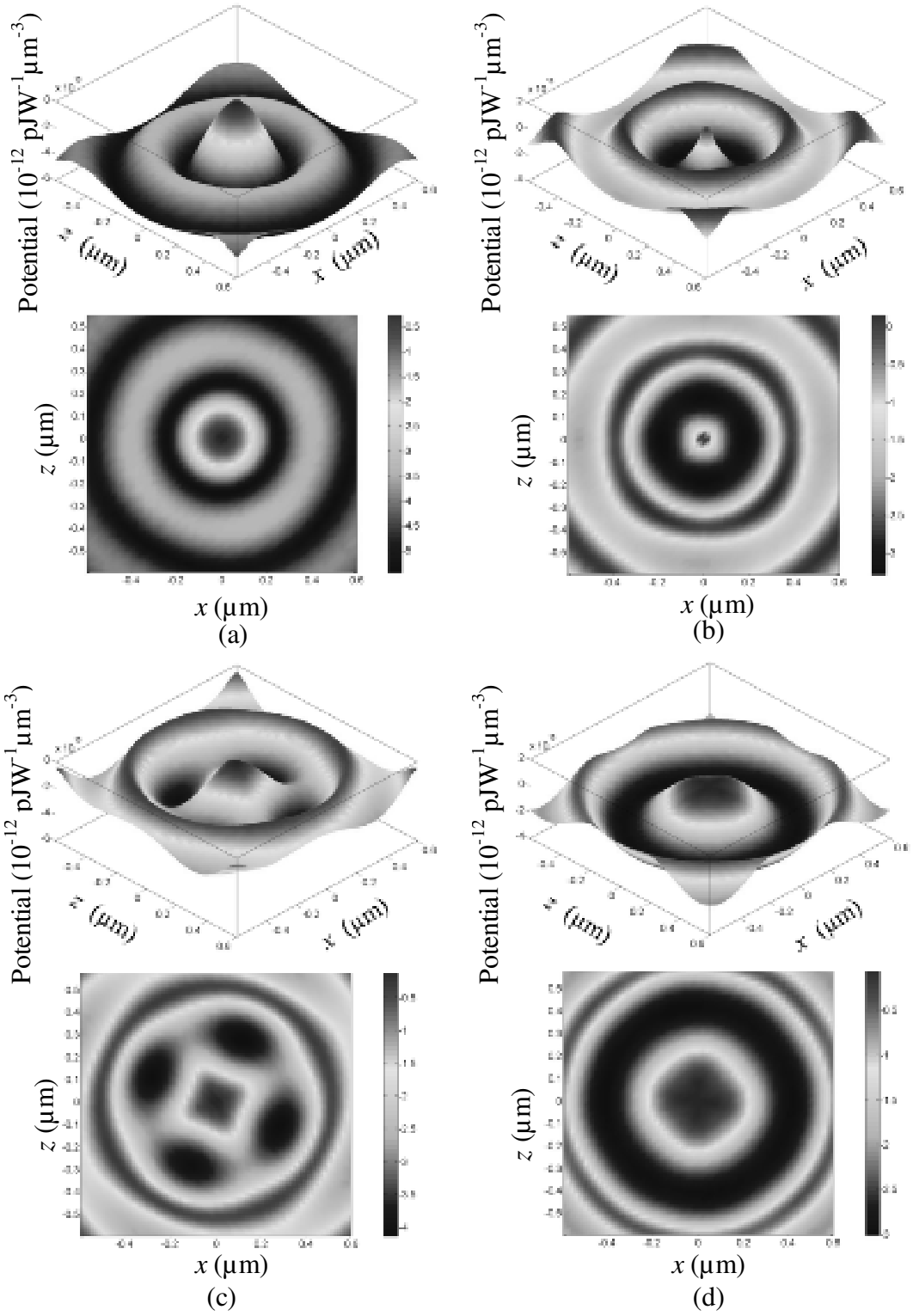

Figure 4.11: The 3D surface of time independent optical potential and corresponding contour plot in the *xz*-plane at $y = 0$ µm when (a) $l = 0$; (b) $l = 1$; (e) $l = 2$; and (f) $l = 3$.

minimums, which have same locations as the locations of the two maximums of Poynting vector as shown in Fig. 4.3 (a).

However, due to the optical force in Eq. (4.13) is time dependent, the calculated optical potential as shown in Fig. 4.10 is also time dependent. Usually, the nano-particle cannot catch up the rotation frequency of the ROF. Otherwise, the nano-particle rotates on a circle with radius of 181nm, and has a rotation frequency same as the light's frequency. It results one abnormal conclusion, which is that the velocity of the nano-particle is faster than the light speed. On the other hand, the optical force cannot generate the corresponding radial acceleration to keep such high frequency rotation. The maximum possible frequency can be estimated based on the force distribution as shown in Fig. 4.5 (a). The normalized force density is around 5×10^{13} $NW^{-1}m^{-3}$, and the mass density has order of 10^3 $kg \cdot m^{-3}$, so the normalized acceleration is 5×10^{10} $ms^{-2}W^{-1}$. Thus, when the input light has power of 1 W, on the circle with radius of 181nm, the maximum possible frequency is 83.6 MHz, which is much smaller than the rotating frequency of the generated ROF (>100 THz).

Using the resultant force in one rotation period to replace the optical force, the Eq. (4.13) can be rewritten as

$$U(r, \theta, y) = \int_C \vec{F}_T(r) \cdot d\vec{r}. \tag{4.15}$$

The time independent optical potential can be obtained.

The time independent optical potential is shown in Fig. 4.11. It can be seen that when angular order equal to zero (i.e. $l = 0$), the optical potential has minimum value of -54.8 $pJW^{-1}\mu m^{-3}$ on the circle with radius of 213 nm. Compared to the minimum optical

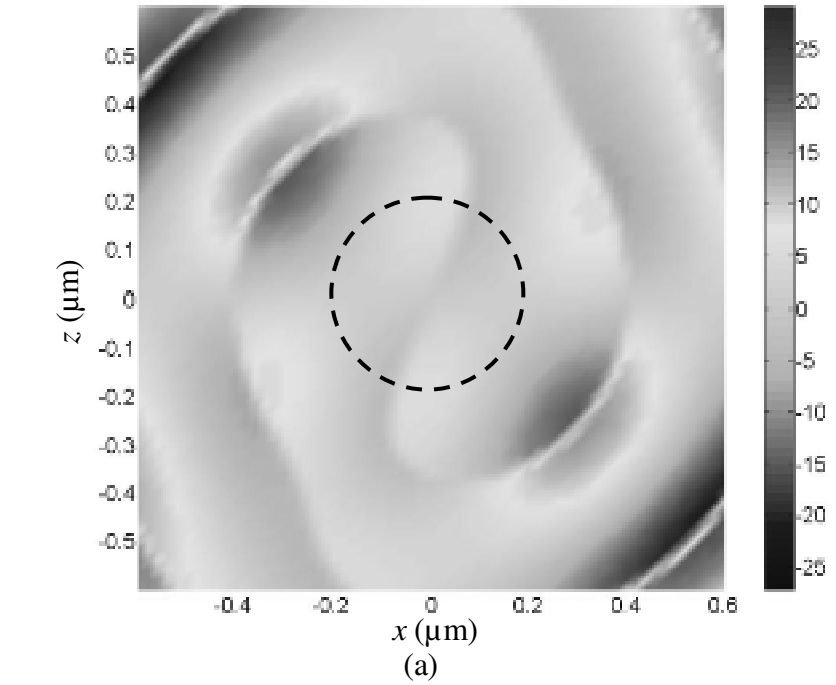

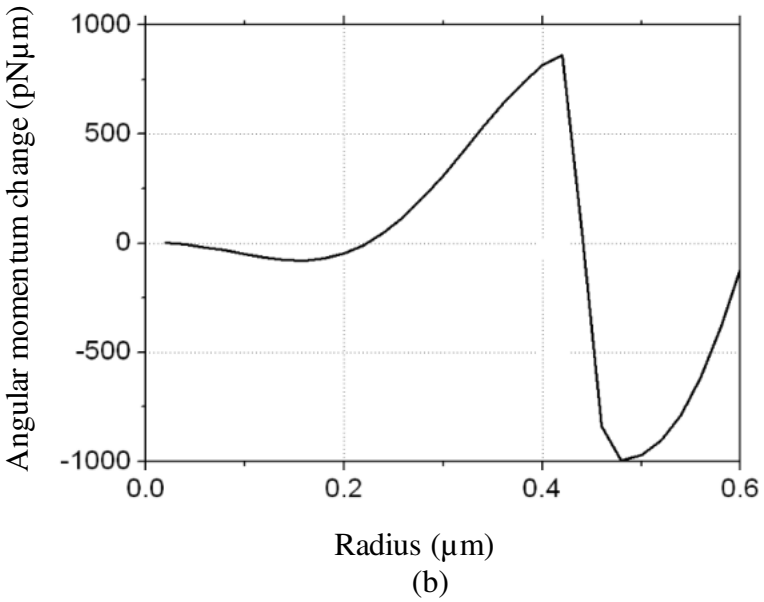

Figure 4.12: (a) the contour plot of optical torque in the *xz*-plane at $y = 0$ μm; and (b) the curve of the nano-particle's angular momentum change per rotation period versus the radius.

potential of -33.1 $pJW^{-1}\mu m^{-3}$ at $l = 1$, -41.2 $pJW^{-1}\mu m^{-3}$ at $l = 2$ and -30.6 $pJW^{-1}\mu m^{-3}$ at $l = 3$, the minimum optical potential at $l = 0$ has the smallest value, which means the corresponding optical field has highest particle trapping capability. In addition, either the optical intensity or the energy flux is well confined in a circular area with radius of 213 nm, which achieve a perfect sub-wavelength focusing, thus, this optical field can efficiently to trap and manipulate nano-particles.

4.2.3 Optical torque

The optical torque is discussed depends on the object. Firstly, the optical torque on a nano-particle is analyzed. Subsequently, the optical torque on a nano-wire is presented. Finally, the optical torque on a nano-rotor is discussed.

4.2.3.1 Nano-particle

For a nano-particle, it is obviously that it can be trapped the generated ROF at the locations where has the lowest optical potential, e.g., on the equilibrium circle with radius of 213 nm at $l = 0$, 181 nm at $l = 1$, 358 nm at $l = 2$ and 380 nm at $l = 3$. When $l = 2$, the circle with radius of 358 nm is degenerated into four local minimums due to the backscattering as analyzed perilously. When $l = 0$, the optical field doesn't rotate, therefore, a nanoparticle inside doesn't have rotation around the y-axis. However, a nano particle will rotate in ROF with angular order of 1 (i.e. $l = 1$). The optical torque on the nanoparticle is calculated based on the Eq. (4.9) and the contour plot is shown in Fig. 4.12(a). The unit of the optical torque is 1.25×10^{-4} $pN\mu mW^{-1}nm^{-3}$, which means contour

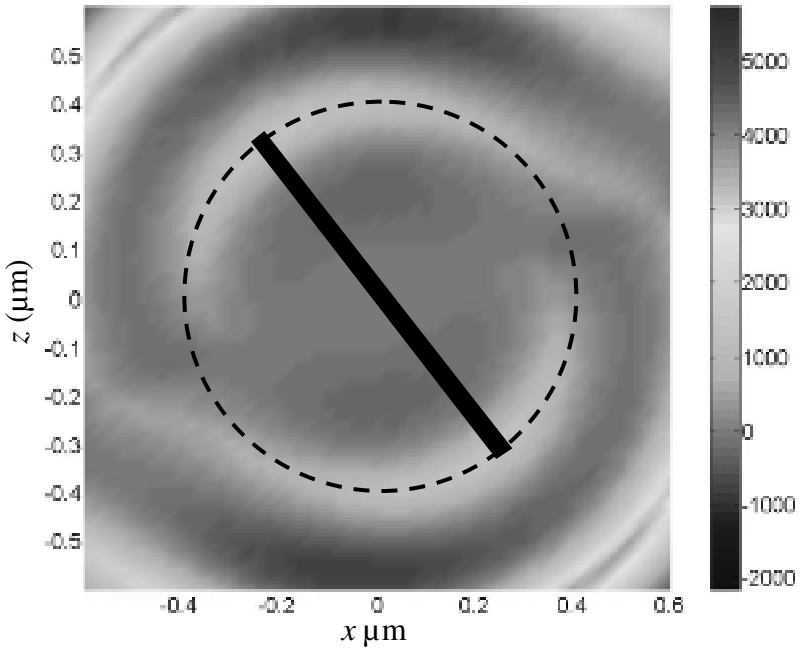

(a)

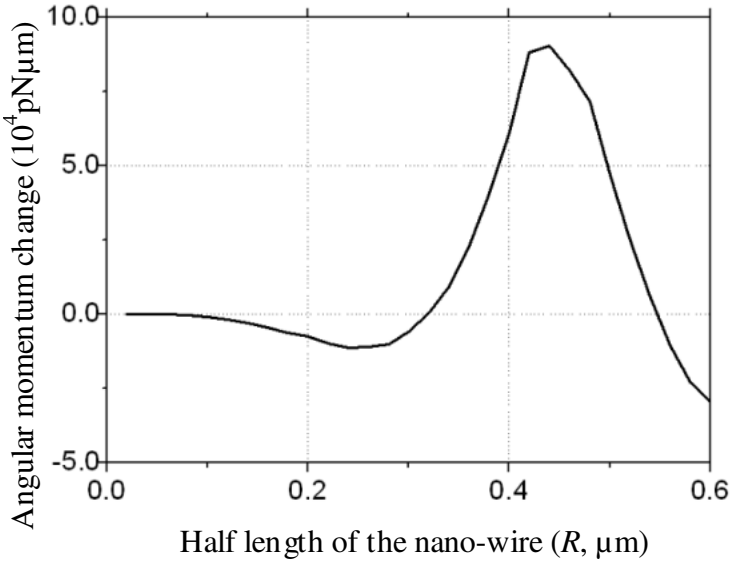

(b)

Figure 4.13: (a) the contour plot of optical torque on nano-wire in the *xz*-plane at y = 0 μm; and (b) the curve of the nano-wire's angular momentum change per rotation period versus the half length of the nano-wire.

plot represent the optical torque on a spherical nano-particle radius of 12.5 nm, which has volume of $(20\text{nm})^{-3}$. Here, the input light has power of 1 W. It can be seen that the optical torque on the nano-particle could be positive or negative. For instance, When x = 0 nm and z = 181 nm, the optical torque on the spherical nano-particle is 7.1 pNμm, and the rotation direction is anticlockwise direction. The change of angular momentum ($\Delta\vec{L}$, corresponds to the y-axis) during one rotation period (T_r) is equal to the integration of optical torque on this time, and it can be expressed as

$$\Delta\vec{L} = \int_0^{T_r} \vec{\tau}(t)dt, \tag{4.16}$$

As mentioned in section 4.3.1.1, the optical fields as well as the optical fields are almost same except the rotation. Thus, the integration of optical torque by time in Eq. (4.16) can be converted into integration along the black dash circle with radius of 181 nm as shown in Fig. 4.12(a). The angular momentum change of a spherical nano-particle with side length of 12.5 nm is varied when the particle is located on circles with different radius as shown in Fig. 4.12(b). It can be seen that the when a particle is located on the circle with radius from 0 to 220 nm, the angular momentum change becomes a negative value, which means that the spherical nano-particle trends to do clockwise rotation. However, when a particle is located on the circle with radius from 220 to 440 nm, the angular momentum change becomes a positive value, which means that the spherical nano-particle trends to do anticlockwise rotation in this range.

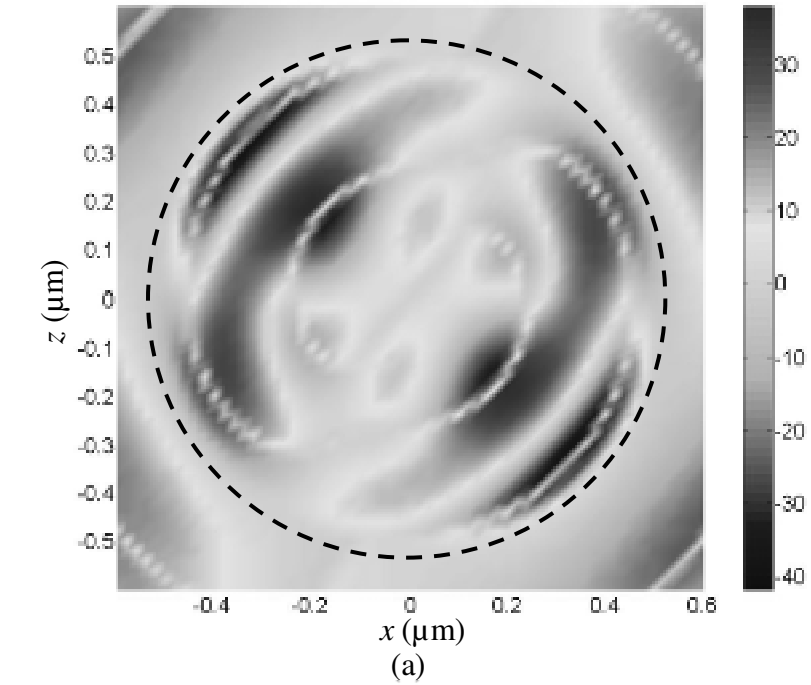

(a)

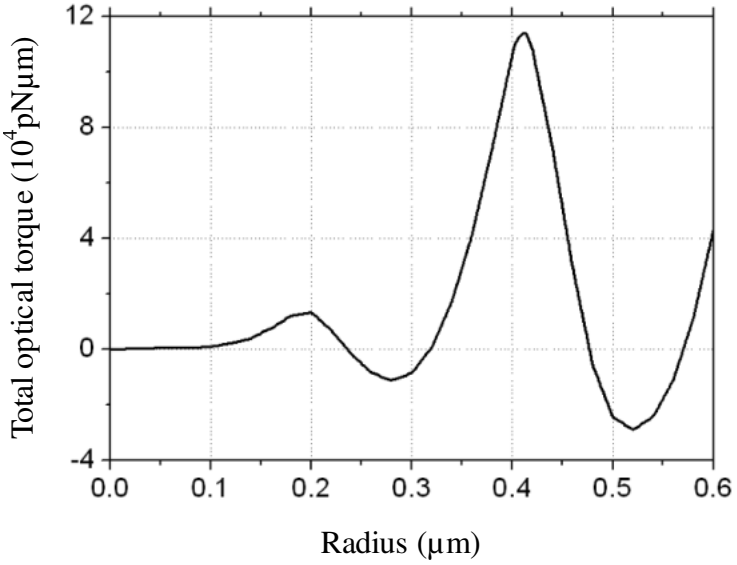

(b)

Figure 4.14: (a) the contour plot of the optical torque in the *xz*-plane at $y = 0$ μm; and (b) the curve of the total torque versus radius.

4.2.3.2 Nano-wire

When the spherical nano-particle is replaced by the nano-wire with height 20 nm, width 20 nm and length $D = 2R$. Assuming the nano-wire is put in the *xz*-plane at y = 0 μm and its center is located on the origin, the optical torque on the nano-wire τ_{nw} can be expressed as

$$\tau_{nw} = \int_{-R}^{R} \vec{F}_T(r) \cdot d\vec{r} \tag{4.17}$$

Based on Eq. (4.17), the calculated optical torque on the nano-wire in the *xz*-plane at y = 0 μm is shown as the contour plot Fig. 4.13(a). The change angular momentum ($\Delta\bar{L}_{nm}$) of the nano-wire during one rotation period (T_r) is equal to the integration of optical torque by this time, which can be expressed as

$$\Delta\bar{L}_{nm} = \int_0^{T_r} \vec{\tau}_{nm}(t)dt. \tag{4.18}$$

The integration of optical torque by time in this equation can also be converted into integration along the black dash circle. The angular momentum change of nano-wire after one rotation period is varied versus the change of the half length (R) as shown in Fig. 4.13(b). It can be seen that when the nano-wire has half length of 440 nm, the angular momentum change per rotation period has maximum value of 9.05×10^4 pN·μm, which means the nano-wire is driven with the highest efficiency. The positive value indicates the nano-wire trends to do an anticlockwise rotation. However, when the half length is in the range from 0 nm to 300 nm and from 560 nm to 600nm, the angular momentum change is a negative value, which means that the spherical nano-particle trends to do clockwise rotation.

4.2.3.3 Nano-rotor

The rotation condition of nano-particle and nano wire is analyzed based on the assumption that the objective doesn't affect the generated ROF deeply. But for a nano-rotor with radius of 0.5 μm, refractive index of 2, height of 0.4 μm, the effects cannot be ignored as discussed in section 4.3.1.1. Thus, the optical torque on the nano-rotor is calculated based on the reformed ROF as shown in Fig. 4.6. The contour plot of the optical torque in the *xz*-plane at $y = 0$ μm is shown in Fig. 4.14(a). Compare to the optical torque without the nano-rotor as shown in Fig. 4.12(a), the maximum optical torque inside the nano-rotor area is increased by the nano-rotor itself. The optical torque at an arbitrary point on the nano-rotor is equal to the optical force on a small volume of (20 nm)^3 times the corresponding radius. By integration of the optical torque on the volume of the nano-rotor, the total torque on the nano-rotor is equal to -2.4×10^4 pNμm, which means that the nano-rotor tends to do a clockwise rotation. However, when the integration is done on a partial of the nano-rotor, i.e., a cylinder with radius varying from 0 to 0.5 μm, the total optical torque on this cylinder is varied correspondingly as shown in Fig. 4.14(b). It can be seen that the total torque has maximum value of 1.08×10^5 pNμm when the radius is 0.44 μm, which means the used radius of nano-rotor is not the optimized radius. To obtain the maximum total optical torque on the designed nano-rotor, the radius should be around, but not the exactly value of 0.44 μm. That is due to the ROF reformation when the nano-rotor is changed.

Similarly, the angular order of the ROF also has effects on the values and distributions of the optical torques. When the $l = 2$ and 3, the contour plots of the

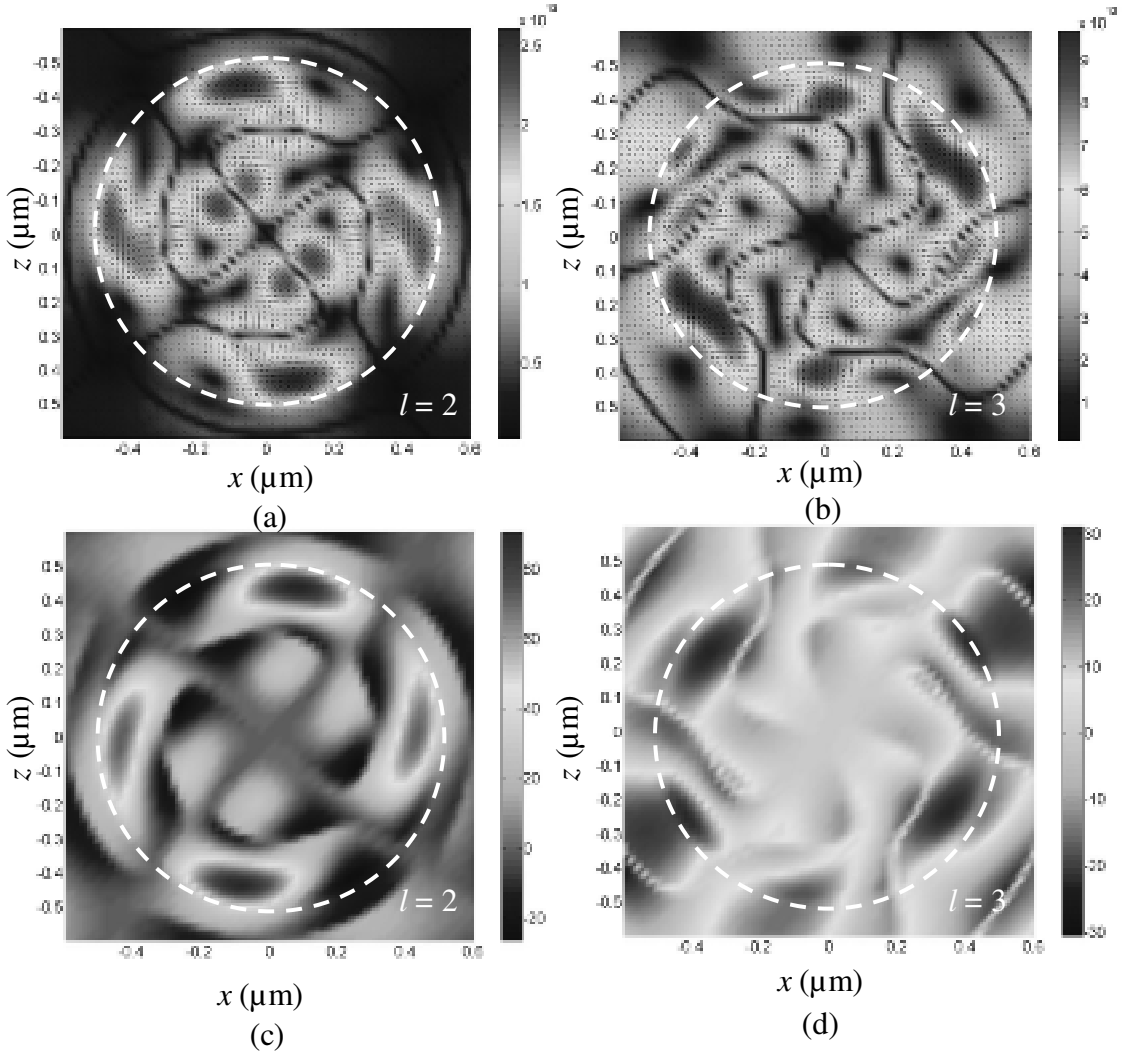

Figure 4.15: The contour plot of $F_{g,xz}$ in xz-plane at $y = 0$ μm when (a) $l = 2$; and (b) $l = 3$; and the contour plot of the optical torque in the xz-plane at $y = 0$ μm when (c) $l = 2$;and (d) $l = 3$.

normalized optical force density in xz-plane at $y = 0$ μm are shown in Fig. 4.15(a) and (b) respectively. It can be seen that the maximum optical force density is 2.63×10^7 $pNW^{-1}\mu m^{-3}$ at $l = 2$ and 9.5×10^6 $pNW^{-1}\mu m^{-3}$ at $l = 3$. The contour plot of the optical torque in the xz-plane at $y = 0$ μm are shown in Fig. 4.15(c) and (d) respectively. As

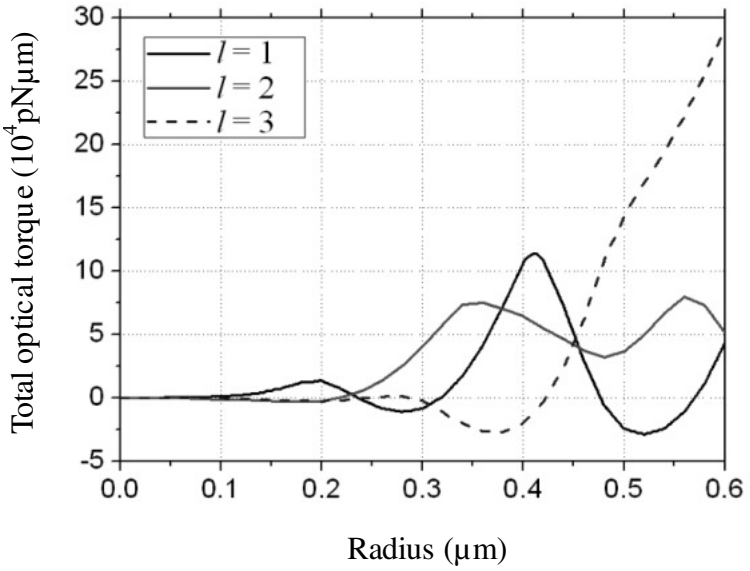

Figure 4.16: the curve of the total torque versus radius when the angular orders are different.

mentioned in section 4.3.1.1, the maximum optical force density is 2.48×10^7 pNW^{-1}μm^{-3} at $l = 1$. It can be found that the 2-folder ROF has largest optical force, which is due to the enhancement of the backscattering. The curves of the total optical torque on a cylinder with radius varying from 0 to 0.5 μm are plotted in Fig. 4.16. When the angular order is increased, the total optical torque on the nano-rotor with radius of 0.5 μm is increased from -2.4×10^4 pNμm (at $l = 1$) to 1.44×10^5 pNμm (at $l = 3$). This means that it is much efficient to use 3-order ROF for driving as compared to 1- or 2-order ROF for the nano-rotor with radius of 0.5 μm. However, 3-order ROF becomes inefficient to drive a small nano rotor with radius less than 0.3 μm. But for the 1-order ROF, the threshold radius is decreased to 0.1 μm.

4.3 Summary

In this chapter, the optical force, the optical potential, and the optical torque of the generated ROF are theoretically analyzed, numerically simulated and discussed.

The optical force includes two terms. The first term is represented by the divergence of the Maxwell stress tensor, and the second term is the change of energy flux, which can be represented by the time derivative of the Poynting vector. The numerical results show that the first term is 6-order of magnitude higher than the second term. Thus, in most cases, the second term is negligible.

The generated ROF as well as the corresponding optical force are affected by the existence of the nano-rotor. Compared to the ROF without the nano-rotor, the maximum values of E_x, E_z, H_y and S_T are enlarged, the space between two neighboring radial maximums of E_x, E_z and H_y are decreased, and the gradient of E_x, E_z, H_y and S_T along the y-axis is increased. The maximum optical force is also increased and the force distributions are changed due to the existence of the nano-rotor.

Different angular orders of the generated ROF correspond to the different resultant force values and distributions. When the l is increased from 0 to 3, the maximum resultant force in the xz-plane at $y = 0$ μm is decreased. The resultant force tends to push a small particle to the regions with highest light intensity, and the region is usually a circle. When the angular order is increased, the radius of the circle is increased, and the circle is degenerated into four individual regions due to the backscattering.

The optical potential is calculated based on the resultant force, and the minimum optical potential has smallest value at $l = 0$, which means the corresponding optical field

has highest particle trapping capability. In addition, particle will be trapped on a circle with radius of 213nm at $l = 0$, 181 nm at $l = 1$, 358 nm at $l = 2$ and 380 nm at $l = 3$, which are same as the regions with highest light intensity.

Finally, the optical torques are analyzed and discussed in the different objects, i.e. spherical nano-particle, nano-wire and nano-rotor.

For the nano-particle, when $l = 1$, the optical torque drives it to do a clockwise rotation when and it is located on the circle with radius from 0 to 220 nm and do an anticlockwise rotation from 220 to 440 nm.

For the nano-wire, the optical torque drives it to do clockwise rotation when its half length is in the range from 0 nm to 300 nm and 560 nm to 600nm and do anticlockwise rotation from 300 nm to 560 nm. When the nano-wire has half length of 440 nm, the nano-wire is driven with the highest efficiency.

For the nano-rotor, when $l = 1$ and the radius is approximate to 0.44 μm, there is a maximum total optical torque on it. When the designed nano-rotor has radius of 0.5 μm, the 3-order ROF has highest driving efficiency. However, to drive a small nano-rotor with radius less than 0.3 μm, 3-order ROF becomes inefficient. But for the 1-order ROF, the threshold radius is decreased to 0.1 μm. The 2-order ROF has driving capability in between of the 1- and 3-order ROF.

CHAPTER 5

COUPLED-RESONATOR-INDUCED TRANSPARENCY (CRIT) TUNING VIA OPTICAL FORCE

Recently, the optical gradient force around the optical ring resonator attracts more attention due to its merits of high efficiency, accurate tuning, and simple fabrication. On the other hand, the ring resonator based coupled-resonator-induced transparency (CRIT) system has many applications in optical storage, slow light and optical switch etc. Therefore, a tunable CRIT using optical force is the objective of this chapter.

The tunable coupled-resonator-induced transparency (CRIT) system by using optical force is designed, fabricated and demonstrated. It consists of one bus waveguide and two coupled ring resonators, in which one ring is released and held by spokes and a pedestal. The different input powers produce different optical forces, which correspond to different optical field buildups, different shifts of transmission spectrum and different time delays. Firstly, the theoretical analysis of the tunable CRIT is discussed. Then, the results of the numerical simulation are illustrated. Subsequently, the nanophotonic fabrication processes are developed. Finally, experimental results are discussed.

5.1 Theoretical analysis

In order to simplify the theoretical analysis of the tunable CRIT system, this section is divided into five subsections. Firstly, the design of the tunable CRIT system is presented. Secondly, the properties of double coupled ring resonator based CRIT system are discussed. Thirdly, the optical force between ring 1 and the substrate is analyzed based on the energy conservation law. Finally, the stable point is determined and the tuning ratio is derived.

5.1.1 Design of the tunable CRIT system

The tunable CRIT system consists of a bus waveguide, a released ring resonator (ring 1) and a fixed ring resonator (ring 2) as shown in Fig. 5.1. The fixed ring is fabricated on a SiO_2 layer and the released ring is supported by a pedestal and four spokes as shown in Fig. 5.1 (a). Two light sources are coupled into the CRIT system through the bus waveguide: (1) the probe light, which is used to detect the CRIT phenomenon, and (2) the control light, which is used to tune the CRIT phenomenon. The probe light can be either a low power broadband light source or a low power laser, and the optical force produced by the probe light is negligible. Because of the CRIT system, a narrow transmission band is observed at the output absorption spectrum. Subsequently, the control laser is injected into the waveguide and coupled into ring 1 through ring 2. The control laser undergoes optical resonance with a high built-up energy in ring 1. The corresponding optical force between the released ring and the substrate deforms the spokes. Due to this deformation, the effective refractive index of ring 1 is changed, which

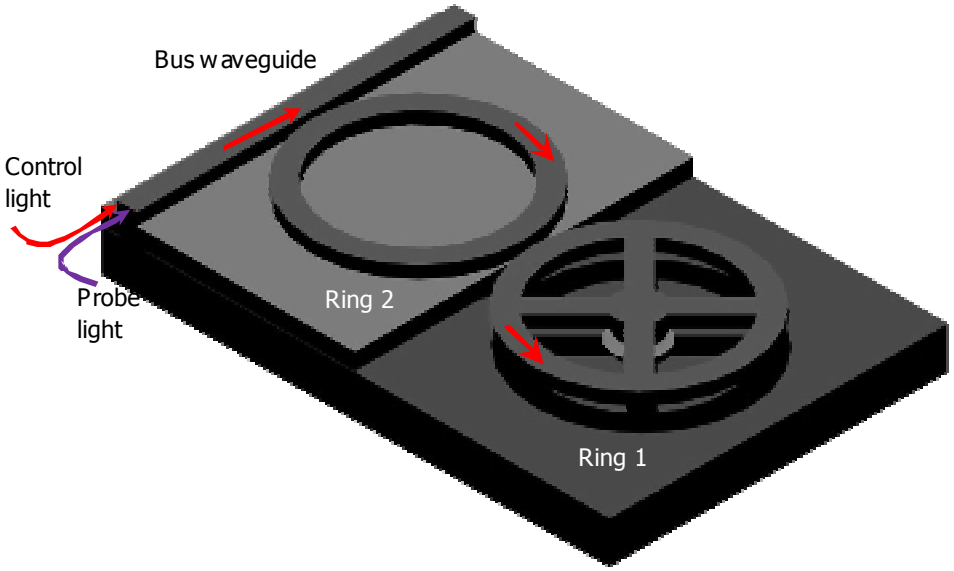

(a)

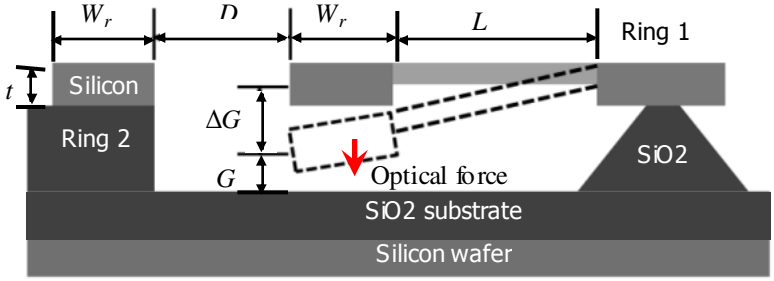

(b)

Figure 5.1: (a) the schematic of coupled-resonator-induced transparency (CRIT) which is tuned by the optical force; (b) the cross section of the coupling region between two ring resonators. The dash line indicates the bent spokes and ring which are driven by optical force.

shifts the transmission band, and changes the group delays, as well as the optical fields in ring 1 and ring 2. Different input powers induce different optical forces on ring 1, which correspond to different deformations. Subsequently, the different extents of shifting are observed in the transmission spectrum. The cross-sectional view of the CRIT system is

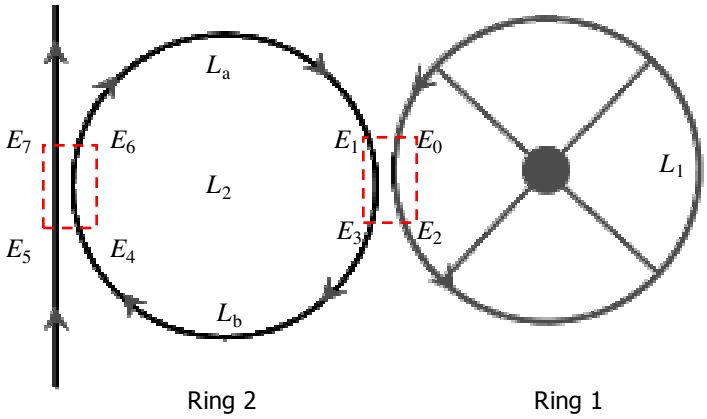

Figure 5.2: The schematic of double coupled ring resonator based CRIT system. The red arrows indicate the directions of light propagation, and the red dash rectangles highlight the coupling regions.

shown in Fig. 5.1 (b). The gap between the two rings is D, the deformation of the released ring due to the optical force is ΔG, the spoke length is l, and the gap between the deformed Ring 1 and the substrate is G, and the initial gap G_o equal to $G + \Delta G$. To simplify the theoretical analysis and the numerical simulation, the two rings are designed to have the same width (W_r), radius (R), thickness (t) and refractive index (N_r).

5.1.2 Ring-resonators-based CRIT

The schematic of double coupled ring resonators based CRIT system is shown Fig. 5.2, in which the red arrows indicate the directions of light propagation, the red dash rectangles highlight the coupling regions, and E_i (i = 0, 1, 2, …, 7) are the complex amplitudes of optical fields at the ports of the two coupling regions. E_5 and E_7 are the amplitude of the input optical field, and the output optical field, respectively. To analyze

the optical properties of the double coupled ring resonators based CRIT system, the transfer matrixes of the optical fields before and after coupling regions can be expressed as [69, 125, 137]

$$\begin{bmatrix} E_3 \\ E_2 \end{bmatrix} = \begin{bmatrix} r_1 & -jt_1 \\ -jt_1 & r_1 \end{bmatrix} \begin{bmatrix} E_1 \\ E_0 \end{bmatrix}, \tag{5.1}$$

and

$$\begin{bmatrix} E_6 \\ E_7 \end{bmatrix} = \begin{bmatrix} r_2 & -jt_2 \\ -jt_2 & r_2 \end{bmatrix} \begin{bmatrix} E_4 \\ E_5 \end{bmatrix}, \tag{5.2}$$

where i = 1 and 2, which indicates coupler 1 (ring-ring coupling region) and coupler 2 (ring-waveguide coupling region) respectively. $r_i = \sqrt{1-K_i}$ and $t_i = \sqrt{K_i}$ are the reflectivity and transmittivity of coupler i. K_1 is the energy coupling coefficient of coupler i, j is the imaginary unit (i.e. j^2 = -1). Considering the continuity, the optical fields inside the same ring are related as,

$$E_0 = a_1 e^{j\phi_1} E_2, \tag{5.3}$$

$$E_1 = a_2^{L_a/L_2} e^{j\phi_2 L_a/L_2} E_6, \tag{5.4}$$

and

$$E_4 = a_2^{L_b/L_2} e^{j\phi_2 L_b/L_2} E_3, \tag{5.5}$$

where $a_i = e^{-\alpha_i L_i/2}$ is the field attenuation factor, α_i is the power loss coefficient, L_a is the waveguide length from coupler 2 to coupler 1 along the light propagation direction, L_b equals L_2 minus L_a, ϕ_i is the collected phase caused by propagation, L_i is the circumference of ring i and τ_1 is the ratio of E_3 to E_1.

Based on the Eqs. (5.1-5), the optical field buildup in ring 1 (B_1) can be expressed as

$$B_1 = \left|\frac{E_2}{E_5}\right| = \left|\rho_1 a_2^{L_a/L_2} e^{j\phi_2 L_a/L_2} \rho_2\right|, \tag{5.6}$$

where

$$\rho_1 \equiv \frac{E_2}{E_1} = \frac{-jt_1}{1 - r_1 a_1 e^{j\phi_1}}, \tag{5.7}$$

and

$$\rho_2 \equiv \frac{E_6}{E_5} = \frac{-jt_2}{1 - r_2 a_2 \tau_1 e^{j\phi_2}}. \tag{5.8}$$

The transmittivity T can be expressed as

$$T = \left|\frac{E_7}{E_5}\right|^2 = \left|\frac{r_2 - a_2 \tau_1 e^{j\phi_2}}{1 - r_2 a_2 \tau_1 e^{j\phi_2}}\right|^2, \tag{5.9}$$

where

$$\tau_1 \equiv \frac{E_3}{E_1} = \frac{r_1 - a_1 e^{j\phi_1}}{1 - r_1 a_1 e^{j\phi_1}}. \tag{5.10}$$

The phase shift caused by the CRIT system is equal to the argument of output to input field ratio, and can be expressed as

$$\Phi = \arg\left(\frac{E_7}{E_5}\right) = \arg\left(\frac{r_2 - a_2 \tau_1 e^{j\phi_2}}{1 - r_2 a_2 \tau_1 e^{j\phi_2}}\right), \tag{5.11}$$

and the group delay is defined as

$$t_D = -\frac{\partial \Phi}{\partial \omega}, \tag{5.12}$$

where ω is the angular frequency of the light, c and λ are the speed of light and the light wavelength in vacuum.

The optical field buildup in ring 1 (B_1) presents the energy storage capability of ring 1. The transmittivity (T) illustrates the transmission of this system, which is an important feature for the light switch. The group delay (t_D) presents the dispersion of the system, and a larger group delay means a smaller group velocity. Using the application point of view, the three parameters are major features of the CRIT system.

In order to calculate the three parameters, the coupling coefficient K_i, the collected phase ϕ_i, and the attenuation factor a_i are necessary.

The K_i can be calculated by integrating the light power on the coupled area, which is expressed as [138]

$$K_i = \sin^2\left(\int_{-\pi/2}^{\pi/2} \frac{\omega\varepsilon_0}{4} \iint_S \left(N_r^2 - 1\right) E^2 dS \cos\theta d\theta,\right), \tag{5.13}$$

where S is the coupling area, ε_0 is the permittivity of the vacuum, N_r is the refractive index of the waveguide. The collected phase $\phi_i = \beta_i L_i = 2\pi N_{i,eff} L_i / \lambda$, where $N_{i,\,eff}$ is the effective refractive index of Ring i, and can be calculated by the finite element method (FEM).

The power loss per length unit α_i can be expressed as [142]

$$\alpha_i = \frac{4\pi}{\lambda} N_{i,img}, \tag{5.14}$$

where $N_{i,img}$ is the imaginary effective refractive index of ring *i*, and also can be calculated by the FEM. Thus, the attenuation factor (a_i) can be obtained by using the expression $a_i = e^{-\alpha_i L_i/2}$.

5.1.3 Optical force on the released ring

The effective index method is derived from the energy conservation law [82, 143]. Assuming there are *N* photons inside Ring, the total optical energy inside ring 1 can be expressed as

$$\xi = N\hbar\omega, \tag{5.15}$$

where $\hbar$ is the reduced Planck constant. Assuming the ring-substrate gap change process is an adiabatic process, the decrease of optical energy is equal to the increase of mechanical energy in ring 1, and assuming all photons in ring 1 are involved in the converting process, the optical force F_o on ring 1 can be expressed as

$$F_o = -\frac{\partial \xi}{\partial G} = -\frac{\partial (N\hbar\omega)}{\partial G} = -N\hbar\frac{\partial \omega}{\partial G} = -\frac{1}{\omega}\frac{\partial \omega}{\partial G}\xi. \tag{5.16}$$

The total energy also can be expressed as

$$\xi = Pt = P\frac{L_1}{v_g} = \frac{N_g P L_1}{c}, \tag{5.17}$$

where v_g is the group velocity, N_g is the group index, L_1 is the circumference of Ring 1, P is the average power in the ring 1, c is seep of light in the vacuum. The light frequency ω

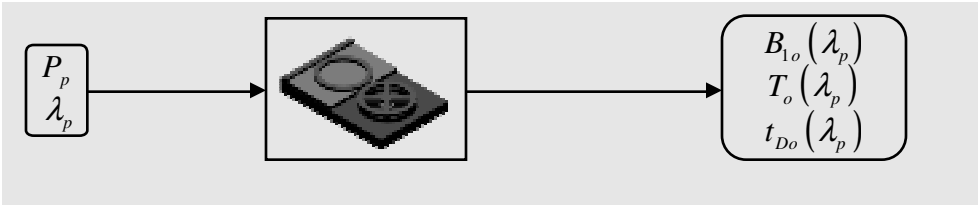

(a)

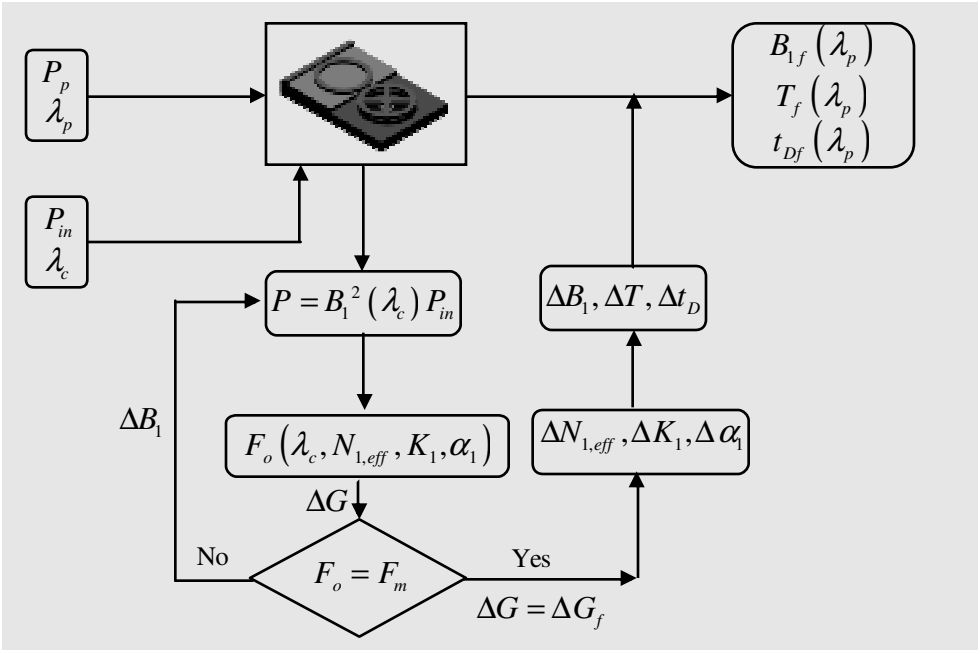

(b)

Figure 5.3: The flow chart of the tunable CRIT (a) without control laser; and (b) with the control laser.

= $\omega_o/N_{1,eff}$, where $N_{1,\ eff}$ is the effective refractive index of Ring 1, ω_o is the angular frequency of the light in the vacuum. The optical force can be rewritten as [143]

$$F_o = \frac{N_g}{cN_{1,eff}} \frac{\partial N_{1,eff}}{\partial G} PL_1. \tag{5.18}$$

The group refractive index (N_g) and can be expressed as [144]

$$N_g = \frac{c}{v_g} = N_{1,eff} - \lambda \frac{dN_{1,eff}}{d\lambda}. \tag{5.19}$$

For the design with fixed N_r, W_r, t and L_1, $N_{1,eff}$ is only dependent on the gap G and the wavelength λ, which can be expressed as

$$N_{1,eff} = N_{1,eff}(G,\lambda), \tag{5.20}$$

and the numerical results can be obtained by finite-element method. The average power P is a function of the input power (P_{in}) and the optical field buildup in ring 1 (B_1), and can be expressed as

$$P = B_1^2 P_{in}. \tag{5.21}$$

Once the P_{in} and λ are given, the B_1 can be calculated based on equation (5.6), and thus, the P as well as the optical force can be calculated.

5.1.4 Stable point determination

Based on the theoretical analysis in the preceding sections, the principles of optical force tuned CRIT system can be derived by using the flow chart as shown in Fig. 5.3. When there is no control light, the probe light with power of P_p and wavelength of λ_p coupled into the CRIT system which has corresponding original optical field buildup B_{1o}, original transmittivity T_o, and original group delay t_{Do}, as shown in Fig. 5.3 (a). When the P_p is very small, the optical force produced by the probe light can be ignored, and the B_{1o}, T_o and t_{Do} are only varied according to the λ_p. When a control laser with power of P_{in} ($P_{in} >> P_p$) and wavelength of λ_c ($\lambda_c \neq \lambda_p$) is coupled into the CRIT system, the optical force F_o in ring 1 is produced, which is the function of λ_c, $N_{1,eff}$, K_1 and α_1. The optical force deforms the spokes, and results in a gap change ΔG (for convenience, it is also referred to as deformation). ΔG changes the B_1, T and t_D by changing of $N_{1,eff}$, K_1 and α_1. When the

ring 1 is finally stopped at a point (i.e. stable point), the stability conditions are: (a) the sum of all external forces on Ring 1 is zero (i.e. $\vec{F}_o + \vec{F}_m = 0$); and (b) The potential energy of ring 1 is at a local minimum. At the stable point, ΔG is equal to ΔG_f, which tunes the B_{1o}, T_o and t_{Do} to B_{1f}, T_f and t_{Df}, respectively.

Considering the amplitudes of the optical force and the mechanical force, and ignoring the horizontal components of the two forces, the stability condition (a) can be rewritten as

$$F_o = 4\zeta\Delta G \tag{5.22}$$

where F_m is replaced by $4\zeta\Delta G$, $\zeta = \frac{Ewt^3}{4l^3}$ is the spring constant of the released spokes, w is the spokes' width, t is height, l is the length and E is young modulus of material. The gravity of ring and spokes (~ 5 fN/ μm) is negligible comparing to the optical force, which will be discussed in the next section.

Due to periodical variation of the optical force, Eq. (5.22) is satisfied by a series of deformations (ΔG_i). However, not all the solutions (ΔG_i) of Eq. (5.22) are satisfied the stability condition (b). To judge which solution corresponds to the stable point, the optomechanical potential U is introduced and can be expressed as

$$U = -W_F = -F_r\Delta G, \tag{5.23}$$

where W_F is the work done by the resultant force F_r, which is equal to the difference between the optical force and the mechanical force (i.e. $F_r = F_o - F_m$).

When ΔG_i is satisfied as

$$\left.\frac{\partial^2 U}{\partial \Delta G^2}\right|_{\Delta G=\Delta G_i} > 0, \tag{5.24}$$

the corresponding potential energies are at local minimums, and these deformations correspond to the stable points.

5.1.5 Tuning ratio

As discussed in the previous section, the final deformation (ΔG_f) is determined by the input power (P_{in}) and wavelength (λ_c) of the control light, which subsequently changes the B_{1o}, T_o and t_{Do} to B_{1f}, T_f and t_{Df}, respectively.

The tuning capability of the control light and the responsiveness of the designed CRIT system could be described by the tuning ratio, which can be defined as

$$S_X = \frac{\partial X}{\partial P_{in}}, \tag{5.25}$$

where X represents B_1, T, or t_D. The tuning ratio can be divided as

$$S_X = \frac{\partial X}{\partial \Delta G_f}\frac{\partial \Delta G_f}{\partial P_{in}}, \tag{5.26}$$

where $\frac{\partial X}{\partial \Delta G_f}$ is the X's change ratio versus deformation and $\frac{\partial \Delta G_f}{\partial P_{in}}$ is the deformation to be produced by unit input power. These two parts are calculated separately in the numerical simulation.

5.2 Numerical results and discussions

The effective refractive indices in deformation-wavelength domain are simulated by the finite-element method (FEM), and the coupling coefficient between the two rings is simulated by using Finite-difference time-domain method. In the simulation, the two rings have same radius (R) of 50 μm. The rings and waveguide have width W_r of 0.45μm, height t of 0.22 μm, refractive index N_r of 3.49 (Si). The substrate is the SiO_2 layer, which has a refractive index N_s of 1.5. The spokes have a height t of 0.22 μm, a width w of 0.5 μm, and a length l of 40 μm. The Young's modulus of silicon is 160 GPa. The horizontal ring-ring gap and ring-waveguide gap D are fixed at 200 nm. All simulations are based on input light with TE-mode.

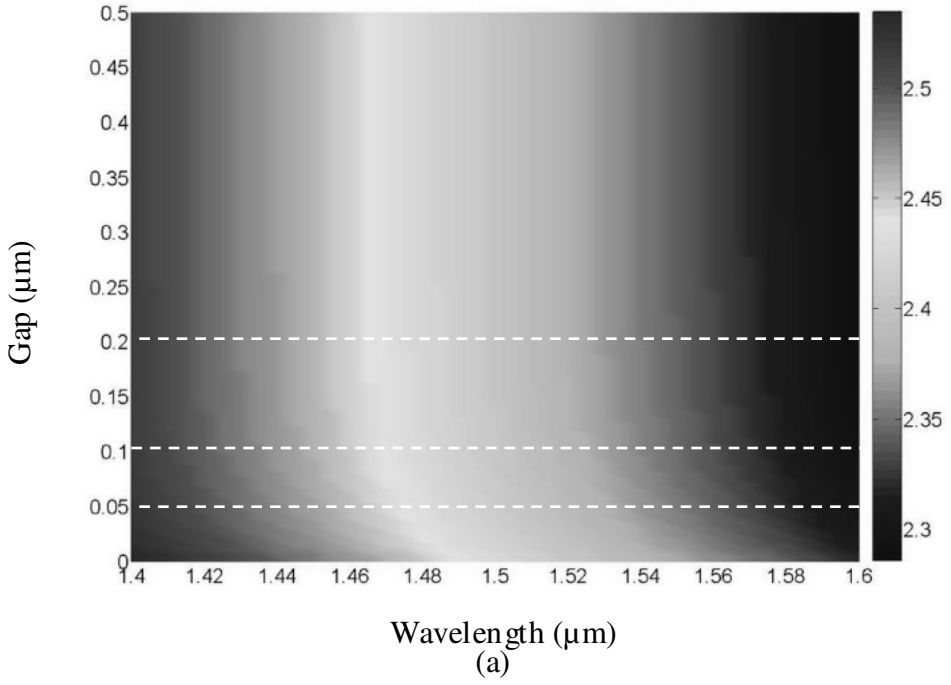

(a)

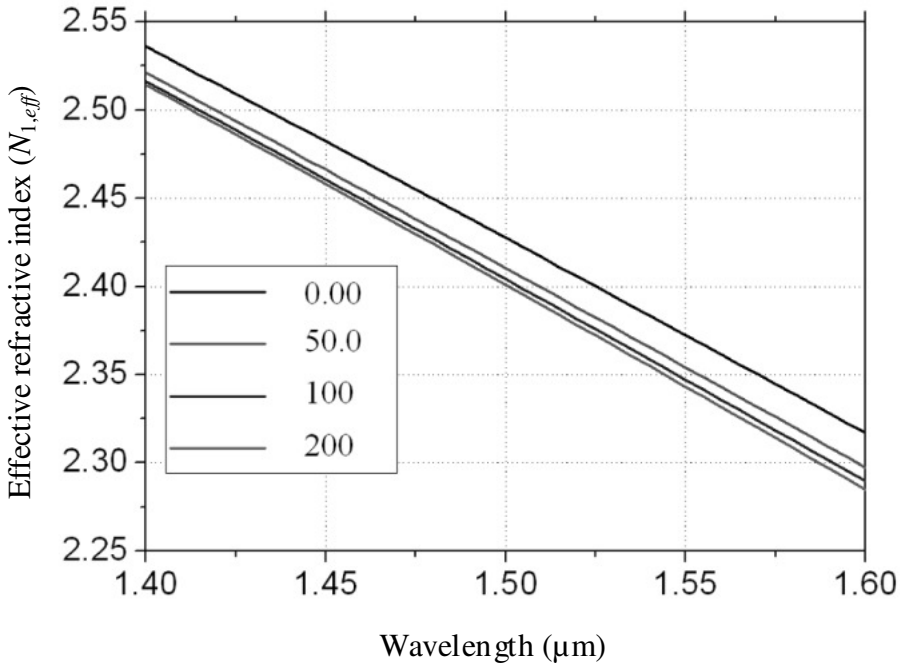

Figure 5.4: (a) the contour plot of effective refractive index in gap-wavelength domain; and (b) the wavelength response of the effective refractive index at G = 0, 50, 100 and 200 nm.

5.2.1 Effective refractive index, attenuation factor and coupling coefficient

To calculate the optical field buildup in ring 1 (B_1), the transmittivity (T) and the group delay (t_D), as mentioned in section 5.1.2, the complex effective refractive index of ring i ($N_{i,\,eff}$), the attenuation factor (a_i) and coupling coefficient (K_i) are necessary besides the wavelength λ.

For the released ring resonator (ring 2), the effective refractive index is affected by the gap (G) and the wavelength (λ). Fig. 5.4 (a) shows the contour plot of the effective refractive index of ring 1 ($N_{1,eff}$) as a function of the gap (G) and the wavelength (λ). The changes in the effective refractive index for wavelength in the range of 1.2 to 1.5 μm at G = 0, 50, 100 and 200 nm, are plotted in Fig. 5.4 (b). It can be seen that the effective refractive index is decreased when the wavelength is increased and the gap is fixed. On the other hand, when the gap is increased and the wavelength is fixed, the effective refractive index is decreased. When the gap is larger than 300 nm, the change of effective refractive index is close to zero ($|\partial N_{1,eff}/\partial G| < 10^{-3}$ RIU/μm) and can be ignored. The sensitive gap range of effective refractive index can be improved with smaller ring's height. Ignoring the spokes' effect, the effective refractive index of ring 2 ($N_{2,eff}$) is equal to the effective refractive index of ring 1 ($N_{1,eff}$) with $G = 0$.

The attenuation factor is calculated by using the expression $a_i = e^{-\alpha_i L_i/2}$, in which the power loss per length unit, α_i, is obtained from the imaginary effective refractive index ($N_{i,img}$) based on Eq. (5.14). The imaginary effective refractive index ($N_{i,img}$) is also

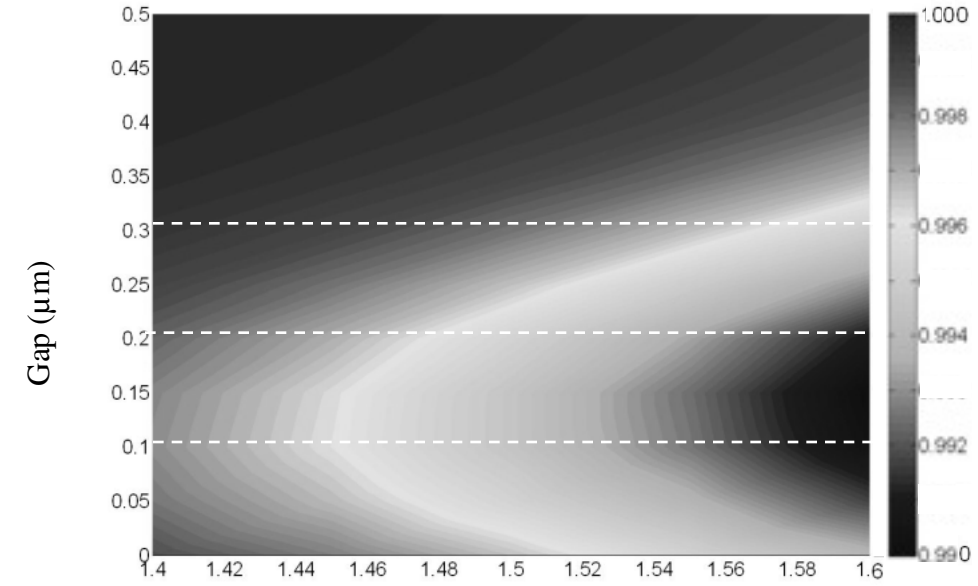

(a)

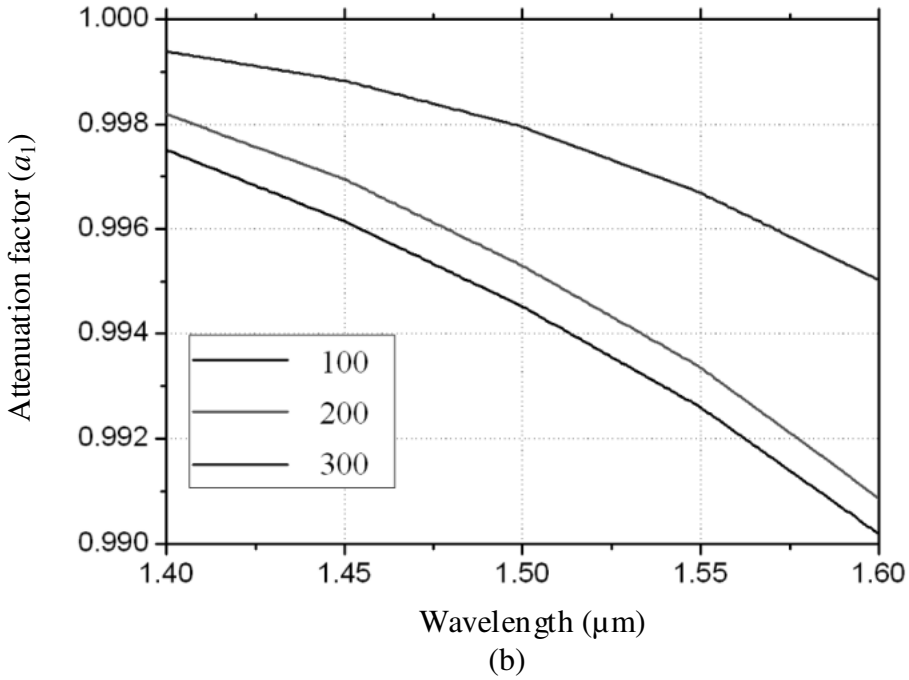

(b)

Figure 5.5: (a) the contour plot of the attenuation factor in gap-wavelength domain; and (b) the wavelength response of the attenuation factor at G = 100, 200 and 300 nm.

obtained from the FEM simulation. Fig. 5.5 (a) shows the contour plot of the attenuation factor of ring 1 (a_1) as a function of the gap (G) and the wavelength (λ). The changes of the attenuation factor for wavelength in the range of 1.4 to 1.6 μm at G = 100, 200 and 300 nm, are plotted in Fig. 5.5 (d). It can be seen that the attenuation factor is decreased when the wavelength increases and the gap is fixed. On the other hand, when the gap is increased and the wavelength is fixed, the attenuation factor decreases and reaches its minimum value at gap around 0.13 μm, thereafter, is increased. The minimum attenuation factor appears neither at the maximum gap nor the minimum gap but at the gap of 0.13 μm, it may be due to the horizontal slot waveguide effects [145]. The attenuation factor (a_2) of ring 2 equals the attenuation factor (a_1) of ring 1 at G = 0.

Based on Eq. (5.13), the coupling coefficient K_i is calculated. In order to simplify the calculation, when $E_0 = 0$, $K_1=|t_1|^2 = |E_2|^2/ |E_1|^2$; similarly, when $E_4 = 0$, $K_2=|t_2|^2 = |E_6|^2/ |E_5|^2$. The $|E_i|_{max}$ (i = 0, 1, 2, …, 7) are obtained by using Finite-difference time-domain method (FDTD) method. It can be used to replace the $|E_i|$ in K_1 and K_2 calculation and don't affect the numerical results. Fig. 5.6 (a) shows the contour plot of the ring-ring coupling coefficient (K_1) as a function of the deformation (ΔG) and the wavelength (λ). The changes of the ring-ring coupling coefficient for deformation in the range of 0 to 0.5 μm at λ = 1.45, 1.50 and 1.55 μm, are plotted in Fig. 5.6 (b). The ring-ring coupling coefficient is decreased when the deformation is increased and the wavelength is fixed. On the other hand, when the wavelength is increased and the deformation is fixed, the ring-ring coupling coefficient is increased. The ring-waveguide coupling coefficient (K_2) increases when the wavelength is increased as shown in Fig. 5.7.

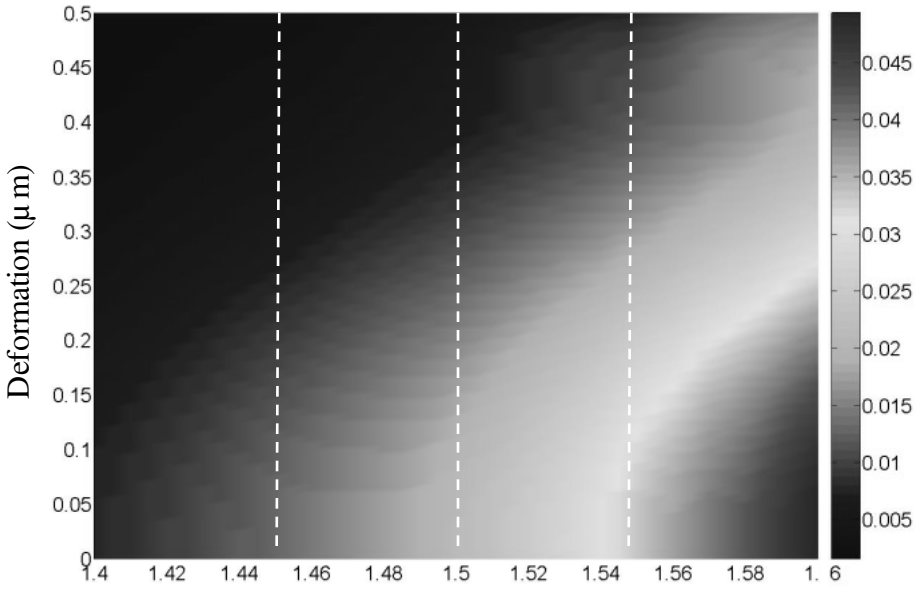

(a)

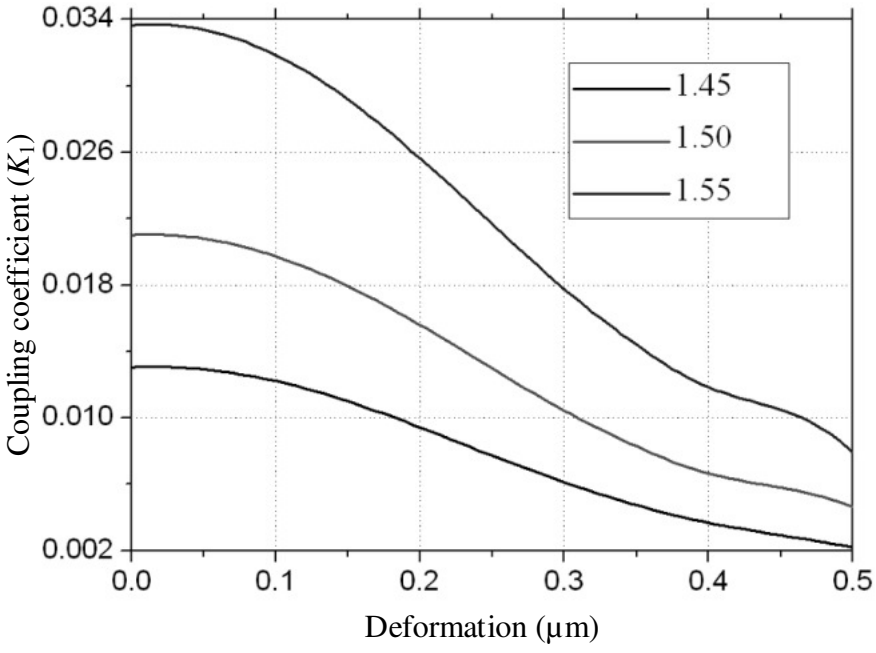

(b)

Figure 5.6: (a) the contour plot of the ring-ring coupling coefficient in deformation-wavelength domain; and (b) the deformation response of the ring-ring coupling coefficient at λ = 1.45, 1.50 and 1.55 μm.

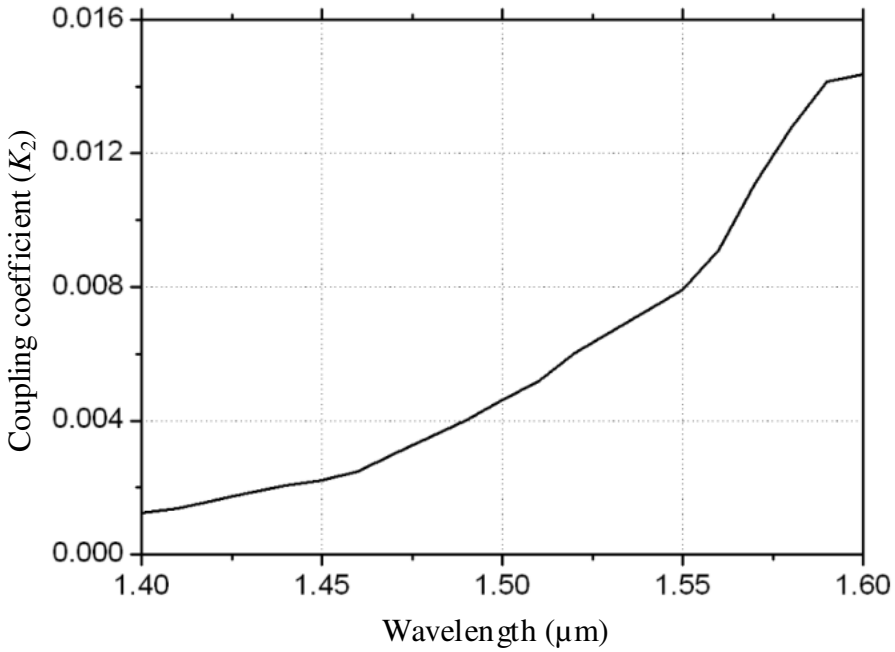

Figure 5.7: The curves of coupling coefficient versus the wavelength.

5.2.2 Optical field buildup, transmittivity and group delay

Since the change of effective refractive index is close to zero when the gap is larger than 300 nm, the original gap (G_o) should be smaller than 300 nm. Otherwise, the optical force between ring 1 and the substrate is negligible. In order to illustrate the numerical calculation process of the final deformation (ΔG_f), the original gap is set as 300 nm. The original gap's effects will be discussed in the next section.

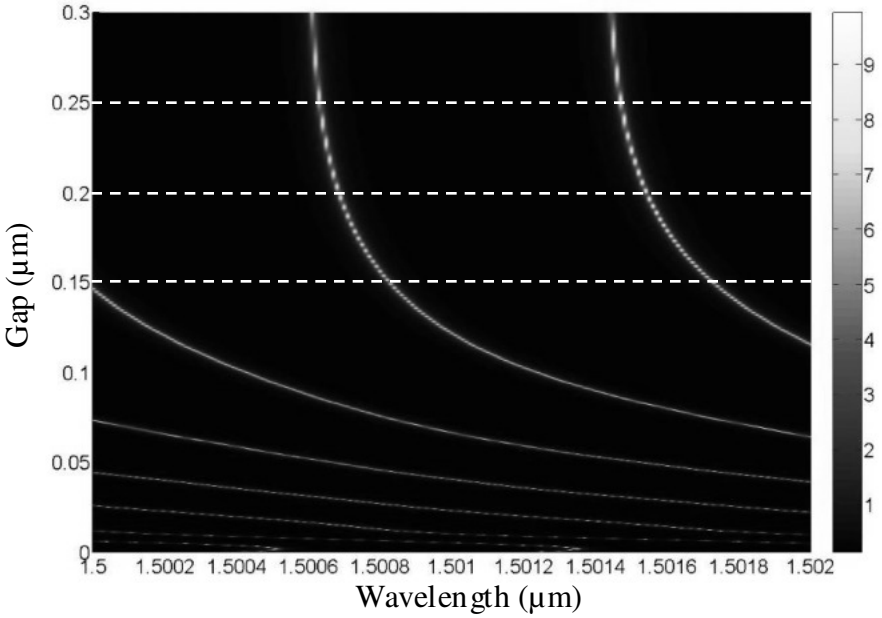

(a)

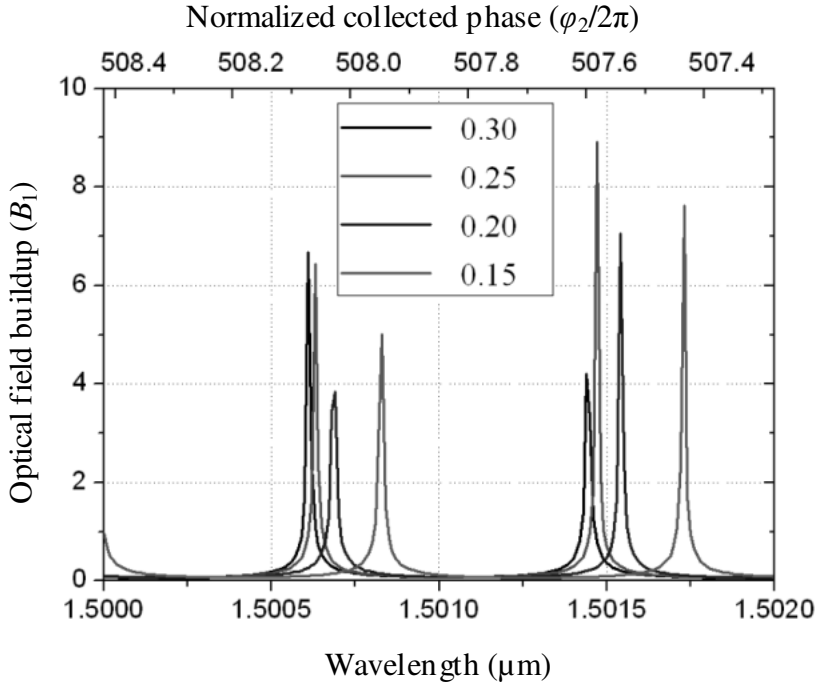

(b)

Figure 5.8: (a) the contour plot of the optical field buildup in gap-wavelength domain; and (b) the wavelength response of the optical field buildup at G = 0.3, 0.25, 0.20 and 0.15 μm.

The optical field buildup in ring 1 (B_1), the transmittivity (T) and the group delay (t_D) are dependent on the position of ring 1, regardless of its velocity as well as acceleration. Based on Eqs. (5.6) – (5.10) and the calculated $N_{i,\,eff}$, a_i and K_i, B_1 is obtained. Fig. 5.8 (a) shows the contour plot of the optical field buildup (B_1) as a function of the gap (G) and the wavelength (λ). The shifts of the optical field buildup for wavelength in the range of 1.5 to 1.502 μm at G = 0.3, 0.25, 0.20 and 0.15 μm are shown in Fig. 5.8 (b). The wavelength range is chosen from 1.500 μm to 1.502 μm, which corresponds to a collected phase band (on ring 2) of 2π, and presents one-period-optical response of the CRIT system. The wavelength response of the original field buildup (B_{1o}) at G = 0.3 μm is indicated by the black solid line. It can be seen that the original optical field buildup has two peaks due to the ring-ring coupling, which are asymmetrical about the line of $\varphi_2/2\pi$ = 508 due to collected phase difference between ring 1 and ring 2. When there is only ring 1 coupled to the bus waveguide, the optical field buildup has a single peak. Thus, the spectrum range between the two optical field buildup peaks is the coupled ring-ring resonator induced transparency band. The bandwidth is determined by the ring-ring coupling coefficient, K_1. When K_1 is increased, the bandwidth is increased. When K_1 is very small (i.e. ring-ring coupling is very weak), the bandwidth becomes very narrow. These phenomena are known as CRIT effects. However, it also requires ultralow loss ring resonators, thus, the weak coupled light can be enhanced by the resonator. In order to achieve the tuning purpose, this design presented in this paper is not to focus on the ultralow loss ring resonator, ultra narrow transparency band, or ultra high dispersions. When the collected phases on ring 1 and ring 2 are equal (i.e. $\varphi_1 = \varphi_2$), the two peaks are symmetrical about the line of $\varphi_2/2\pi$ = 508.

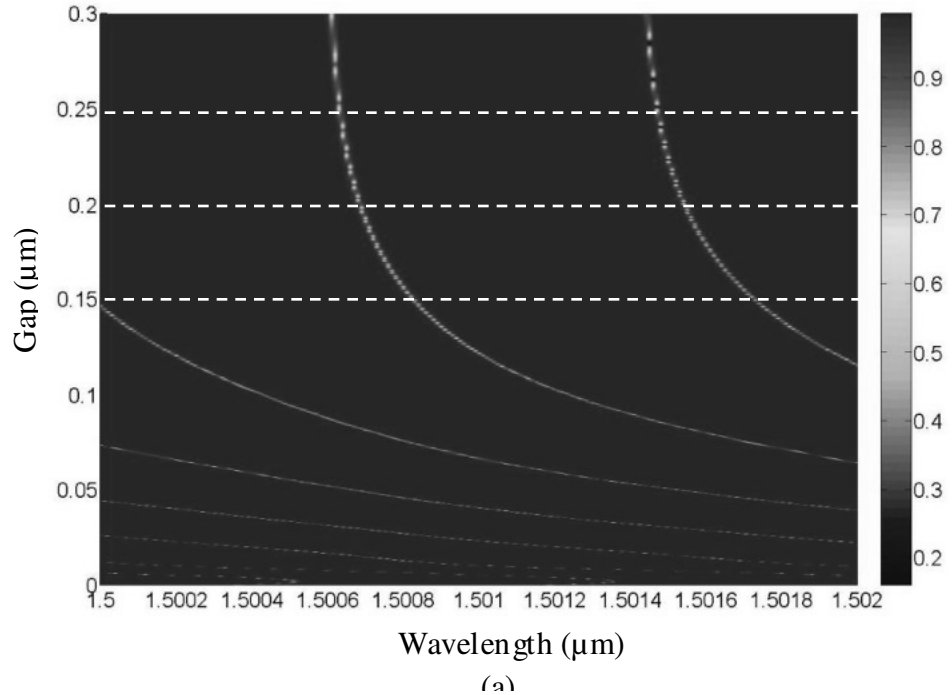

(a)

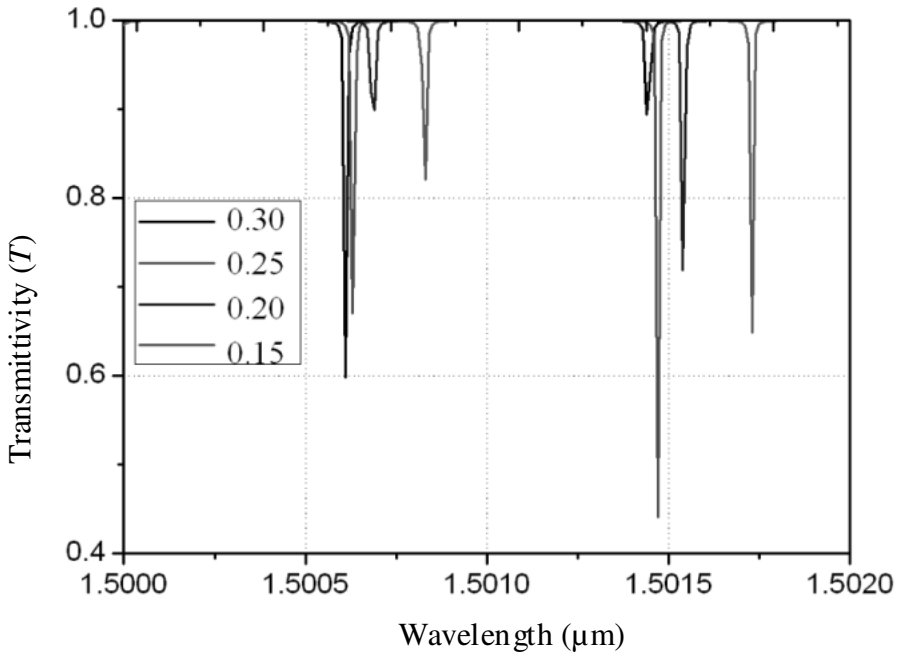

(b)

Figure 5.9: (a) the contour plot of the transmittivity in gap-wavelength domain; and (b) the wavelength response of the transmittivity at G = 0.3, 0.25, 0.20 and 0.15 μm.

However, this symmetry doesn't have obvious merits in applications, and faces complicated designing processes. The optical buildup peaks redshift when the gap is decreased, and the maximum values are varied correspondingly.

Based on Eq. (5.9), the transmittivity (T) is obtained. The contour plot of the transmittivity (T) as a function of the gap (G) and the wavelength (λ) is shown in Fig. 5.9 (a). The transmittivity for wavelength in the range of 1.5 to 1.502 μm at G = 0.3, 0.25, 0.20 and 0.15 μm are shown in Fig. 5.9 (b). The wavelength response of the original transmittivity (T_o) at G = 0.3 μm is indicated by the black solid line. Similarly, the transmittivity peaks have red shifted when the gap is decreased, and the minimum transmittivity are varied correspondingly.

The group delay is calculated based on Eqs. (24) – (25), which presents the rate of change of the phase shift with respect to angular frequency, and presents the transit time required for optical power to travel through the CRIT part. Compare to a system with a bus waveguide only, the CRIT system slows the transportation speed of the optical power. For instance, when the optical power of a pulse travels through a waveguide or through a CRIT system with a same length waveguide, the required transit times are different. The time difference between them is the calculated group delay, which is the reciprocal of the group velocity. Here the group velocity corresponds to the whole system, is different to the mentioned group velocity in ring 1. Fig. 5.10 (a) shows the contour plot of the logarithmic value of the group delay ($\lg(t_D)$) as a function of the gap (G) and the wavelength (λ). The group delay for wavelength in the range of 1.5 to 1.502 μm at G = 0.30, 0.20, 0.10 and 0.05 μm, are shown in Fig. 5.10 (b). The wavelength

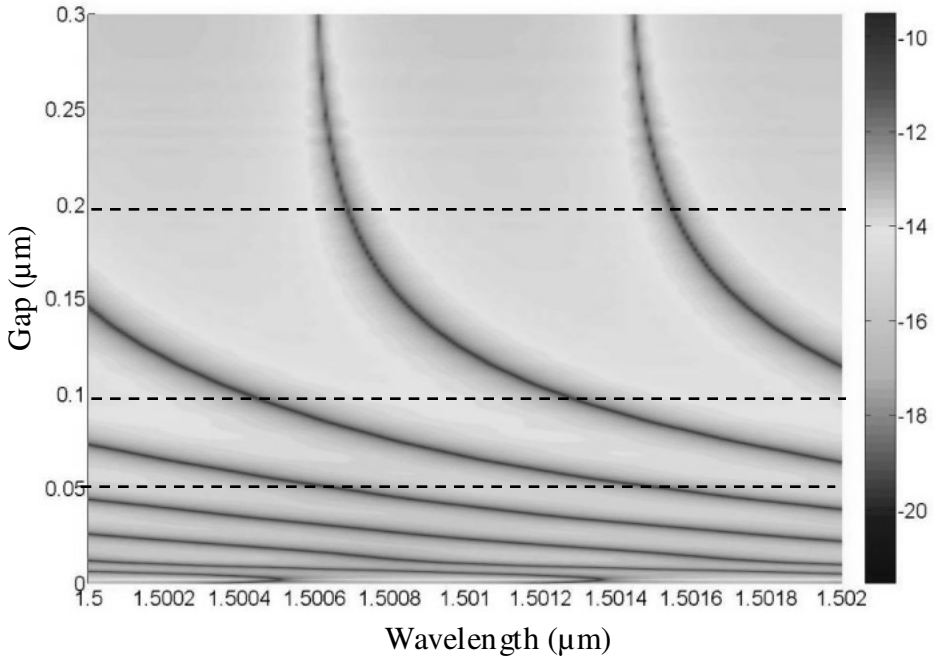

(a)

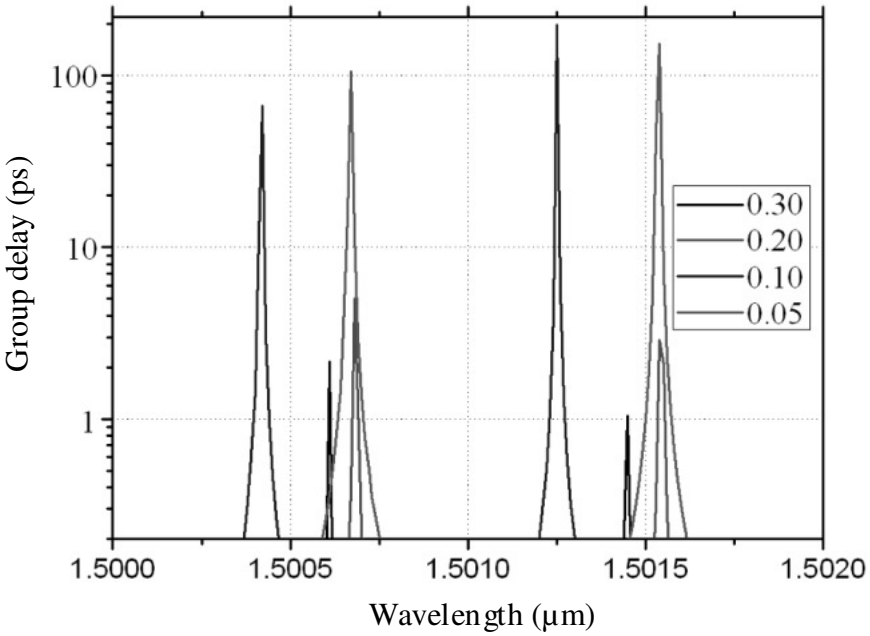

(b)

Figure 5.10: (a) the contour plot of the logarithmic value of the group delay in gap-wavelength domain; and (b) the wavelength response of the group delay at G = 0.3, 0.25, 0.20 and 0.15 μm.

response of the original group delay at G = 0.3 μm is indicated by the black solid line. The longest delay time at G = 0.3 μm and G = 0.05 μm has a value of 2.16 ps and 153.41 ps, respectively.

Therefore, the original values of the optical field buildup in ring 1 (B_1), the transmittivity (T), and the group delay (t_D) are produced in gap-wavelength domain when the original gap is set as 300 nm (i. e., G_o = 300 nm). As indicated by theoretical analysis, the following step is to find out the stable point, which can be used for the calculation of final values.

5.2.3 Stable point determination

In order to obtain the final values of the optical field buildup, the transmittivity, and the group delay, the final deformation (ΔG_f) has to be calculated. Once the final deformation is confirmed, these final values can be obtained based on the contour plots Figs. 5.8 – 5.10.

The final deformation (ΔG_f) corresponds to the stable point of ring 1, which is determined by Eq. (5.22) and judged by the second derivative test of optomechanical potential U. Base on the graphing method, when the input power (P_{in}) is assumed as 1 mW, the power in ring 1 is calculated by using Eq. (5.21), and the optical force can be calculated based on Eq. (5.18). The optical force normalized to the input power is numerically figured out in gap-wavelength domain. Fig. 5.11 (a) shows the contour plot of the logarithmic value of the normalized optical force ($\lg F_o$) as a function of the gap

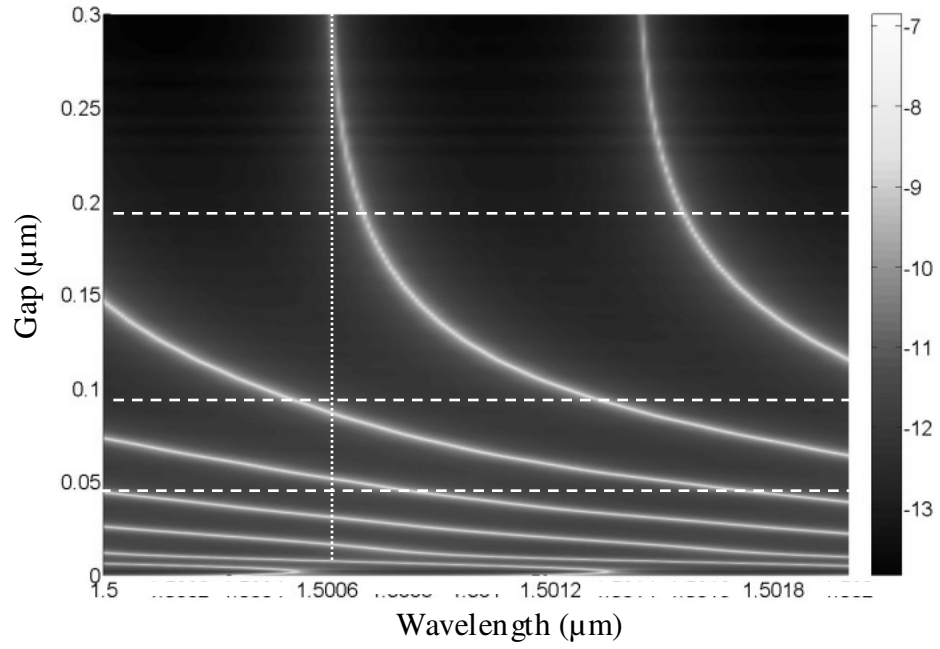

(a)

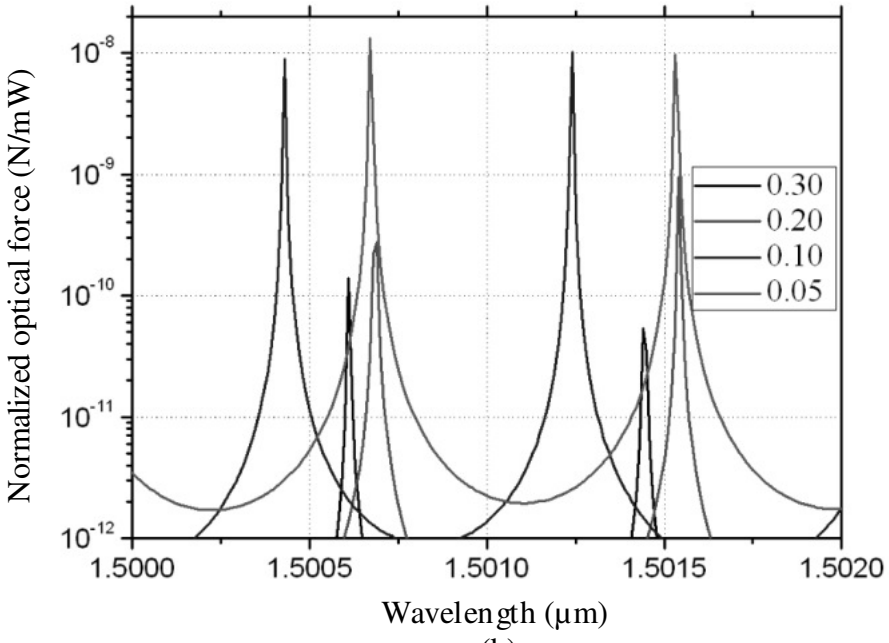

(b)

Figure 5.11: (a) the contour plot of the logarithmic value of the optical force in gap-wavelength domain; and (b) the wavelength response of the optical force at G = 0.30, 0.20, 0.10 and 0.05 μm.

(G) and the wavelength (λ). The normalized optical force associated with wavelength in the range of 1.5 to 1.502 μm at G = 0.30, 0.20, 0.10 and 0.05 μm is shown in Fig. 5.11 (b). The wavelength response of the normalized original optical force at G = 0.3 μm is indicated by the black solid line. It can be seen that the normalized optical force is larger than 1 pN/mW when the input wavelength is in the ranges from 1.50058 to 1.50064 μm and from 1.50141 to 1.50147 μm. The optical force has maximum value of 139.1 pN at λ_c = 1.50061μm. There are two peaks on the wavelength response of the optical force, which correspond to two wavelengths, and are the same as the two wavelengths corresponding to the two peaks on the wavelength response of B_1. It means that the optical force on ring 1 is dominated by the optical field buildup rather than the change of effective refractive index. This is reasonable because that B_1 has a much higher maximum change rate than $N_{1,eff}$'s. When the gap is decreased, the two peaks on the wavelength response broaden. Based on Eq. (5.22), the mechanical force (F_m) is linearly proportional to ΔG, and the spring constant has value of 2.99 pN/nm (ξ = 2.99 pN/nm).

When the control laser has a wavelength of 1.50061μm, the curves of the optical force versus deformation at P_{in} = 1, 5, 50 and 500 mW are plotted in Fig. 5.12 (a), as well as the curve of mechanical force. When control laser has input power of 50mW, the curves of mechanical force and optical force versus deformation at λ_c = 1.50061, 1.50062, 1.50063 and 1.50064 μm are plotted in Fig. 5.12 (b). The deformations (ΔG_i), which correspond to the crossing points between the curves of the optical force and the mechanical force as shown in Figs. 5.12 (a) and (b), are the solutions of Eq. (5.22). It can be seen that when P_{in} is increased, the optical force is increased. When λ_c is increased, the peaks on the curves are shifted to the larger deformation direction. However, the first

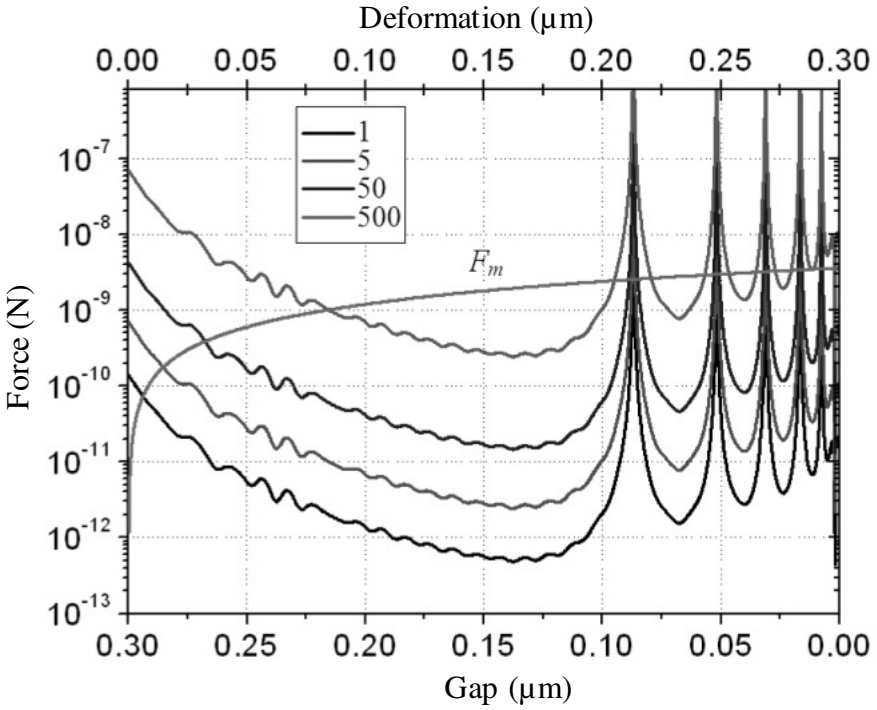

(a)

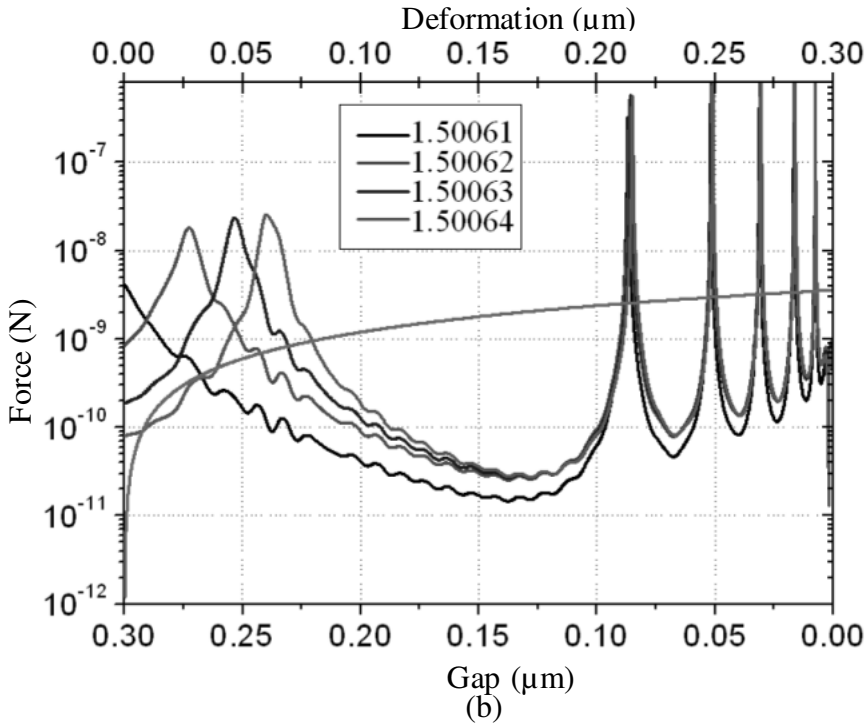

(b)

Figure 5.12: (a) the curves of mechanical force and optical forces versus deformation at P_{in} = 1, 5, 50 and 500 mW; and (b) the curves of mechanical force and optical force versus deformation at λ_c = 1.50061, 1.50062, 1.50063 and 1.50064 μm.

peak is shifted much faster than the other peaks. It is because that when a peak corresponds to a small deformation (i.e., the gap is large), the change rate of the effective index ($N_{1,eff}$) is relatively small as shown in Fig. 5.4 (a). Compared to the peak at a large deformation, a larger deformation increase (gap decrease) is required to reduce the same value of the effective refractive index. Thus, to cancel the same increase of the collected phase, (i.e., $\Delta\varphi_1 = \Delta\varphi_1(\Delta\lambda_c)$), the peak at a small deformation has larger shift. On the other hand, the curve of mechanical force is not changed when the input power or the wavelength increases.

When the control laser has a wavelength of 1.50061μm, there are 11 crossing points between the curve of optical force at P_{in} = 1 mW and the curve of the mechanical force, which correspond to 11 deformations. When the input power is increased from 1 mW, the number of the crossing points is decreased. When the input power is high enough, the number of the crossing points decreases to zero, which means the optical force is always higher than the mechanical force when the deformation is in the range from 0 to 300 nm. Under this condition, the final deformation is 300nm, and the optical force is balanced by an additional normal force. Conversely, when the input power is decreased from 1 mW, the number of the crossing points also decreases. But even the input power is close to zero, there is at least one crossing points, which corresponds to a tiny deformation. Usually, there are more than one crossing points between the two curves in a large input power range.

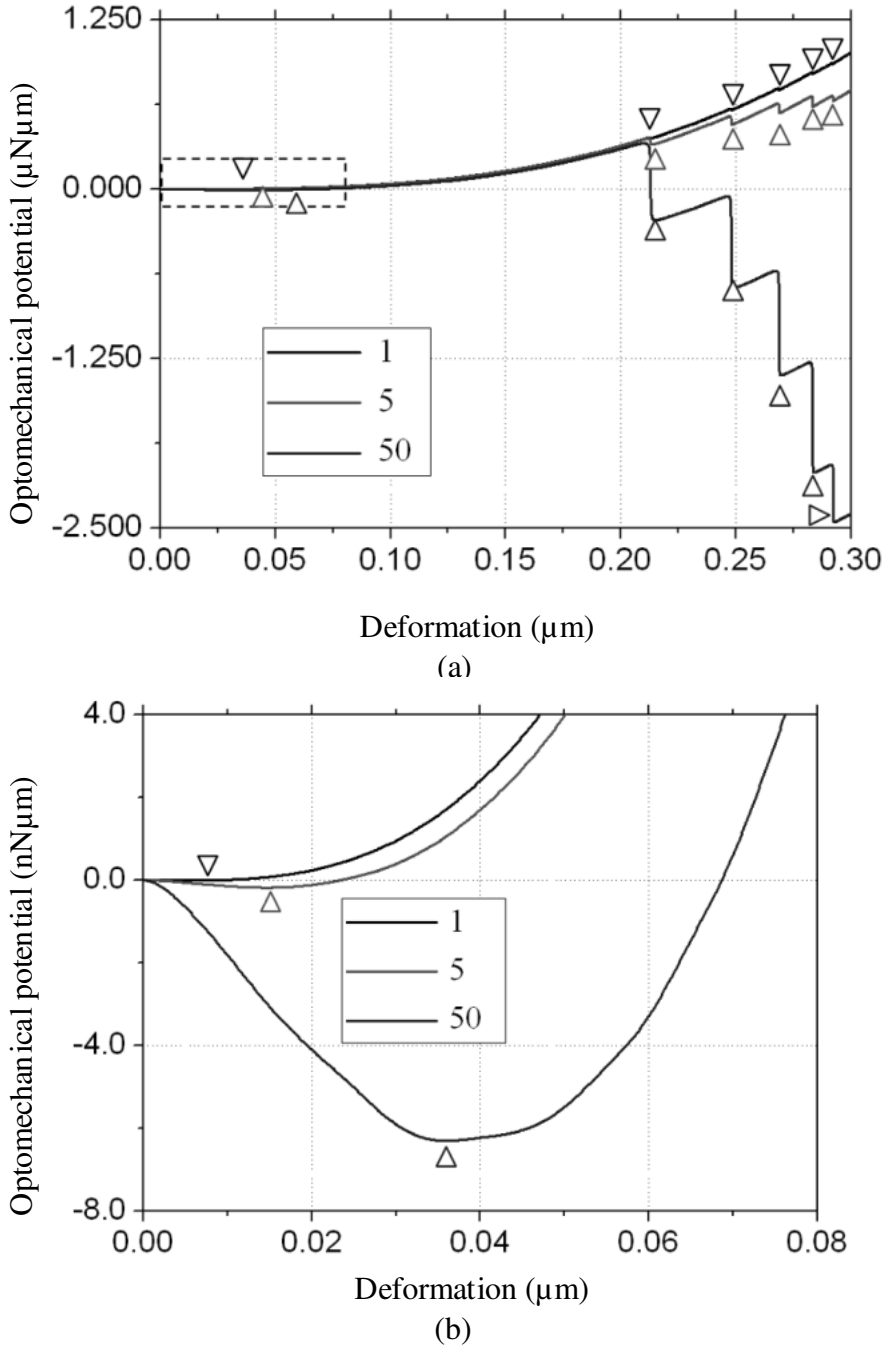

Figure 5.13: (a) the curves of optomechanical potential versus deformation at P_{in} =1, 5, and 50 mW; and (b) the magnified view of the curves corresponding to the area highlighted by dash rectangle in (a).

When control laser has input power of 50mW, there are 11 crossing points between the curve of optical force at λ_c = 1.50061 μm and the curve of the mechanical force. When λ_c is increased to 1.50064 μm, the number of crossing points is increased to 13. However, the wavelength neither reduces nor increases the number of crossing points.

To find out the stable points among these crossing points, Eq. (5.24) is used to determine the local minimums. The curves of optomechanical potential versus deformation at P_{in} = 1, 5 and 50 mW are plotted in Fig. 5.13 (a). The magnified view of the curves for deformation in a different range is shown in Fig. 5.13 (b). It can be seen that there are 6 local minima on each potential curve as indicated by triangles, which correspond to 6 stable points. Compared to the 11 crossing points as shown in Fig. 5.12 (a), the number of points is decreased. The other five crossing points correspond to the 5 local maxima on the curve of the optomechanical potential as shown in Fig. 5.13 (a), which means these points are not stable points. In the other words, when ring 1 is stopped at these 5 points and has a very small deviation, and then the forces of the system drive ring 1 away these points.

The locations of the crossing points are also affected by the wavelength besides the input power. When the input power is fixed at 50 mW, the curves of optomechanical potential versus deformation at λ_c = 1.50061, 1.50062 and 1.50063 μm are plotted in Fig. 5.14 (a). The magnified view of the curves for deformation in a different range is shown in Fig. 5.14 (b).

However, the case with the 6 stable points is still very complicated for the further analysis. Assuming the tuning process always starts from the original state, which

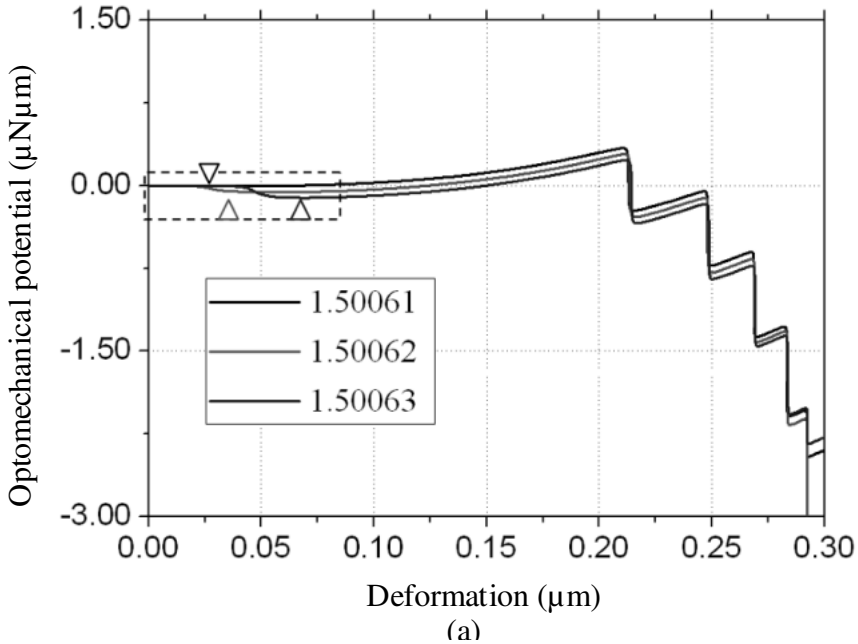

Figure 5.14: (a) the curves of optomechanical potential versus deformation at λc = 1.50061, 1.50062 and 1.50063 μm; and (b) the magnified view of the curves corresponding to the area highlighted by dash rectangle in (a).

means $\Delta G|_{t=0}=0$ and $\Delta \dot{G}|_{t=0}=0$, thus, ring 1 does not has additional energy to pass through the potential barrier between the first and the second stable point when the input power is not very high (i.e. P_{in} = 1, 5 and 50 mW). The maximum input power $P_{in}|_{\max}$ will be discussed in the next section. When the input power is in the range from 0 to $P_{in}|_{\max}$, the first crossing point is the only stable point that ring 1 can reach and stop at there. The deformation corresponds to the first crossing point is the final deformation. For instance, when λ_c has value of 1.50061μm, the final deformation is 6.0 nm at P_{in} = 1 mW, 14.7 nm at P_{in} = 5 mW and 35.9 nm at P_{in} = 50 mW; When the control laser has input power of 50mW, the final deformation is 35.9 nm at λ_c = 1.50061μm, 57.6 nm at λ_c = 1.50062μm and 69.2 nm at λ_c = 1.50063μm.

In this section, the stable points are obtained from Eq. (5.22) based on the graphing method and judged by the second derivative test of the optomechanical potential (i.e. Eq. (5.24)). When the tuning process starts from the original state and the input power is in the range from 0 to $P_{in}|_{\max}$, the final deformation is finalized at the first stable point.

5.2.4 Tuning ratio and tuning range

By using the obtained final deformation, e.g. ΔG_f = 69.2 nm at P_{in} = 50 mW, λ_c = 1.50063μm, the final optical field buildup, B_{1f}, the final transmittivity, T_f and the final group delay, t_{Df} can be determined based on the contour plots in Figs. 5.8 – 5.10. There is a large tuning between B_{1f} & $B_{1o,}$ T_f & t_{Df}, T_o and t_{Do} as shown in Fig. 5.15 (a – c). For instance, when the probe wavelength is 1.50148μm, the optical field buildup is tuned

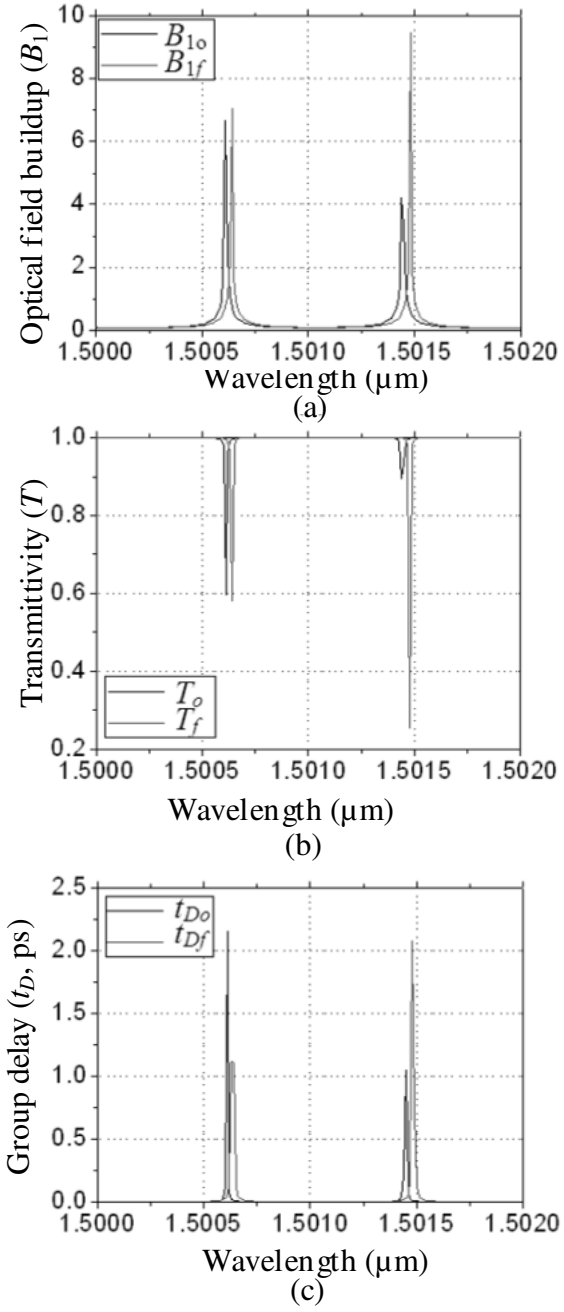

Figure 5.15: The wavelength response of (a) the original and final optical field buildup; (b) the original and final transmittivity; and (c) the original and final group delay when ΔG_f = 69.2 nm at P_{in} = 50 mW, λ_c = 1.50063μm.

from 0.57 to 9.49, which means that the energy stored in ring 1is increased 276.2 $((9.49/0.57)^2 - 1)$ times. The transmittivity is tuned from 0.998 to 0.255, which means that 74.6% of the transmitted energy is switched off. The group delay is tuned from 0.01 to 2.07 ps, which means that the light speed is slowed down 207 times.

In order to optimize the design of the tunable CRIT system, the tuning ratio is introduced to describe the responsibility of the designed device and the tuning capability of the control light.

As analyzed in section 5.2.4, the tuning ratio can be separated into two parts. The first expression, $\partial X/\partial \Delta G_f$, is the X's change ratio versus deformation (X presents B_1, T, or t_D) and the second expression, $\partial \Delta G_f/\partial P_{in}$, is deformation caused per input power unit. $\partial X/\partial \Delta G_f$ can be obtained from the contour plots in Figs. 5.8-5.10. $\partial \Delta G_f/\partial P_{in}$ can be calculated by the graphing method as shown in Fig. 5.12. The curves of the final deformation (ΔG_f) versus input power (P_{in}) at G_o = 300, 200 and 100 nm and corresponding control wavelength λ_c = 1.50061, 1.50154 and 1.50124 μm are plotted in Fig. 5.16. It can be seen that the corresponding maximum power $P_{in}|_{max}$ = 139, 57 and 4 mW respectively, which means that the final deformation equals to the original gap ($\Delta G_f = G_o$) when the input power is larger than the maximum power. The tuning range bands of final deformation are 58.6, 19.3 and 4.2 nm at G_o = 300, 200 and 100 nm respectively. When the original gap is decreased, the maximum power decreases. It is because of the great increase of the optical force as shown in Fig. 5.11 (b). The corresponding final deformation tuning range is decreased, due to the optical field buildup changes faster at a small gap area than at a large gap area, as shown in Fig. 5.8 (a).

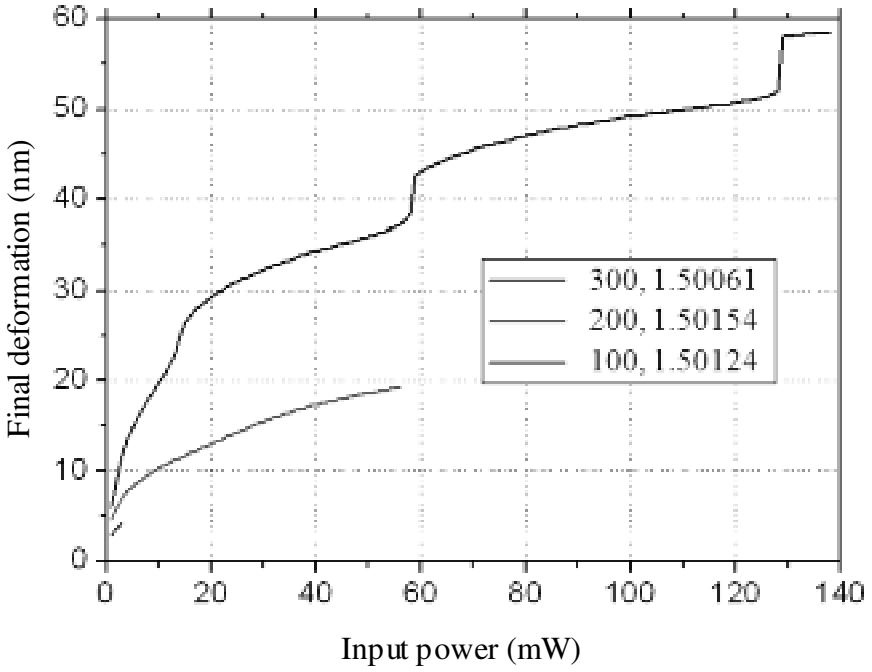

Figure 5.16: the curves of the final deformation versus input power at G_o = 300, 200 and 100 nm, and corresponding control wavelength λ_c = 1.50061, 1.50154 and 1.50124 μm.

The final deformation change per input power unit times B_1's change ratio equals the tuning ratio of the optical field buildup in ring 1. When the input power is increased, the tuning ratio of the optical field buildup increases firstly, and reaches maximum values at P_{in} = 6 mW, thereafter, decreases as shown in Fig. 5.17 (a). It can be seen that the tuning ratio reaches 4.1×10^4 per W when the original gap is 300 nm (G_o = 300 nm), the control wavelength is 1.50061 μm (λ_c = 1.50061 μm), the input power is 6 mW (P_{in} = 6 mW), and the probe wavelength is 1.50144 μm (λ_p = 1.50144 μm). When the original gap is decreased to 200 nm (G_o = 200 nm), the tuning ratio is decreased and the

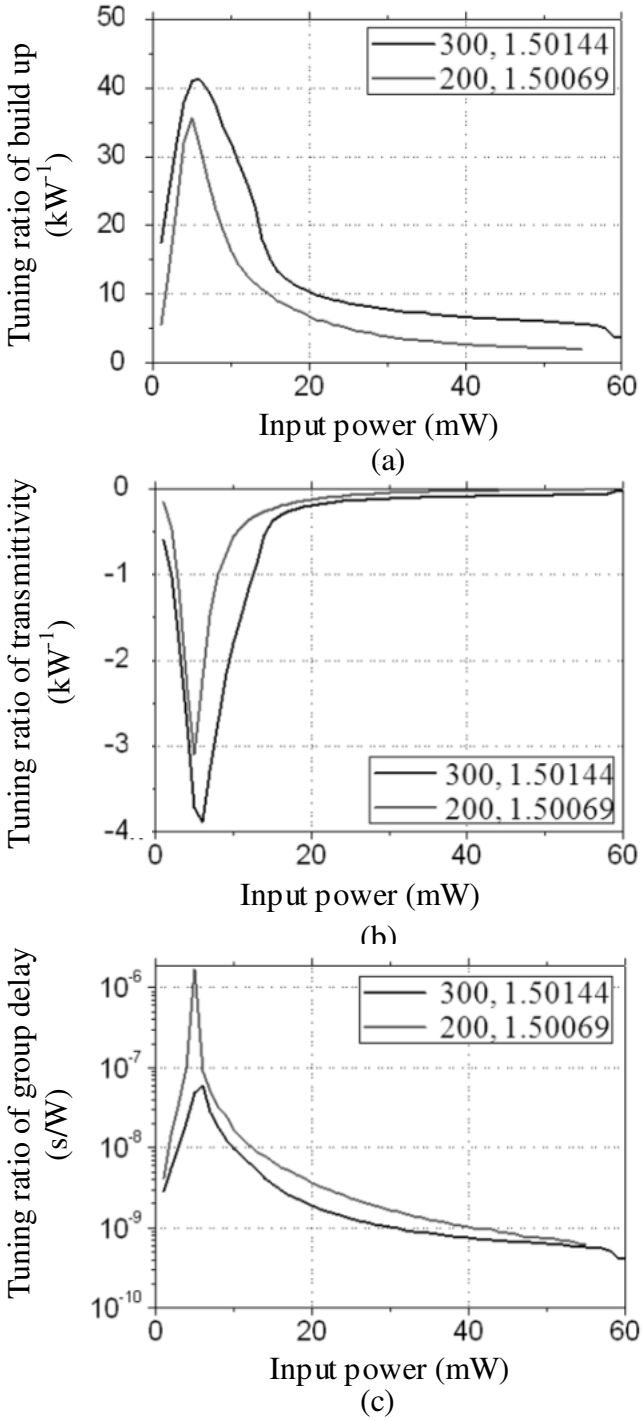

Figure 5.17: the curve of (b) the optical field buildup tuning ratio; (c) the transmittivity tuning ratio; (d) the group delay tuning ratio versus the input power at G_o = 300 and 200 nm, the corresponding probe wavelength λ_p = 1.50144 and 1.50069 μm.

corresponding λ_c = 1.50154 μm and λ_p = 1.50069 μm.

The final deformation change per input power unit times T's change ratio equals the tuning ratio of the transmittivity. When the input power is increased, the tuning ratio of the transmittivity increases firstly, and reaches maximum values at P_{in} = 5 mW, thereafter, decreases as shown in Fig. 5.17 (b). Here, only the amplitude of the tuning ratio is considered, and the negative tuning ratio indicates that when the input power is increased, the transmittivity is decreased. It can be seen that the tuning ratio of the transmittivity reaches -3.6×10^3 per W when the original gap is 300 nm (G_o = 300 nm), control wavelength is 1.50061 μm (λ_c = 1.50061 μm), input power is 5 mW (P_{in} = 5 mW), and the probe wavelength is 1.50144 μm (λ_p = 1.50144 μm). When the original gap is decreased to 200 nm (G_o = 200 nm), the amplitude of the tuning ratio is decreased, and the corresponding λ_c = 1.50154 μm and λ_p = 1.50069 μm.

The final deformation change per input power unit times t_D's change ratio equals the tuning ratio of the group delay. When the input power is increased, the tuning ratio of the group delay is increased firstly, and reaches maximum values at P_{in} = 5 mW, thereafter, decreases as shown in Fig. 5.17 (c). It can be seen that the tuning ratio of reaches 1.7 μsW^{-1} when the original gap is 200 nm (G_o = 200 nm), control wavelength is 1.50154 μm (λ_c = 1.50154 μm), input power is approximate to 5 mW ($P_{in} \approx$ 5 mW), and the probe wavelength is 1.50069 μm (λ_p = 1.50069 μm). When the original gap is increased to 300 nm (G_o = 300 nm), the tuning ratio is decreased, and the corresponding λ_c = 1.50061 μm and λ_p = 1.50144 μm.

Based on the tuning ratios shown in Fig. 5.17, the efficient input power range of control laser ranges from 0 to 20 mW, which means that the larger original gap caused

larger tuning range become an unattractive feature. On the other hand, the optical force is negligible when the original gap is larger than 300 nm. Thus, for the tuning of energy storage in ring 1 and the transmittivity tuning, the original gap should approximate to 300 nm for larger tuning ratio. But for the group delay tuning, the original gap should be smaller than 200 nm.

5.3 Fabrication processes

The tunable CRIT system is fabricated using the silicon nanophotonic fabrication processes which include photolithography, wet and dry etching, chemical vapor deposition (CVD) and sputtering deposition. The reactive ion etching (RIE) is used for the etching technology, which has merits of high selectivity, anisotropy, simple and CMOS compatible process.

The silicon-on-insulator (SOI) wafer is used for fabrication, which consists of a top silicon layer, a buried oxide layer (SiO_2) and a silicon substrate layer as shown in Fig. 5.18 (a). The top silicon layer with thickness of 220 nm is used as the structure layer. The bus waveguide, the ring resonators, and the spokes are both fabricated by the top silicon layer. The oxide layer has thickness of 2 μm, which is partially removed by wet chemical etching using HF. The remained oxide layer has three functions. The first function is to support the unreleased ring and the bus waveguide. The second function of the remained pedestal is to support the released ring through the spokes. And the last function is to act as the substrate, which has attractive optical force with the released and prevent light penetrating into the silicon substrate. The silicon substrate has thickness of 500 μm, and its main function is for handling.

The silicon nanophotonic fabrication processes flow is shown in Fig. 5.18. The hard mask (e.g. silicon oxide) is deposited on the top of the SOI wafer, and the photoresist layer is coated for lithography fabrication as shown in Fig. 5.18 (b). Using photolithography method, the hard mask with the designed patterns is remained on the top as shown in Fig. 5.18 (c). Thereafter, the hard mask etching technology is applied

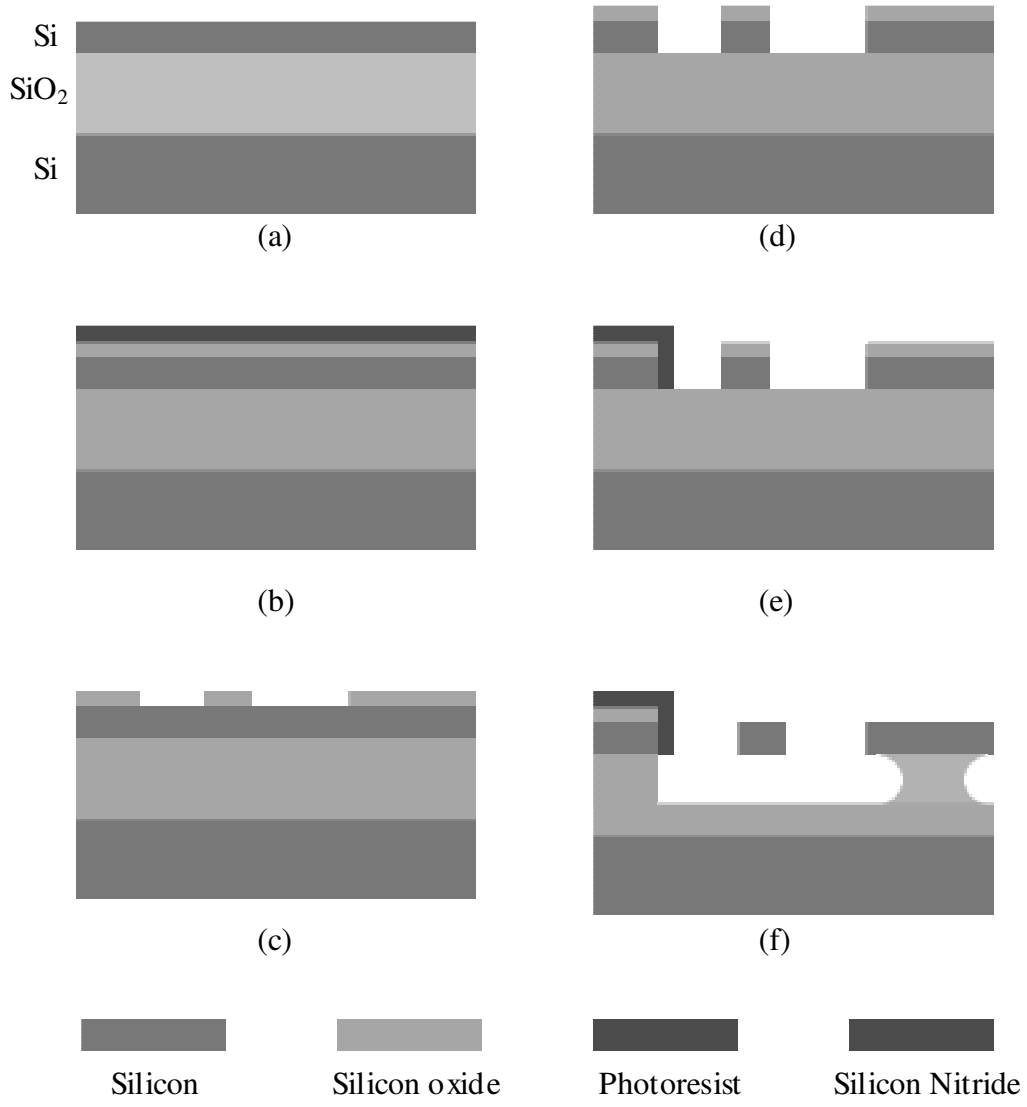

Figure 5.18: The schematic of the fabrication processes flow.

to remove the uncovered silicon. After this step, the designed rings and waveguides are fabricated as shown in Fig. 5.18 (d). A thin SiN layer (1 nm) is deposited on the unreleased parts for protection as shown in Fig. 5.18 (e). After the wet etching in HF, a partial of the silicon oxide layer is removed as shown in Fig. 5.18 (f). The gap between the released ring and the remained silicon oxide is controlled by the etching time.

5.4 Experimental results and discussions

In this section, the tuning experimental results of the CRIT system using optical force are demonstrated and discussed.

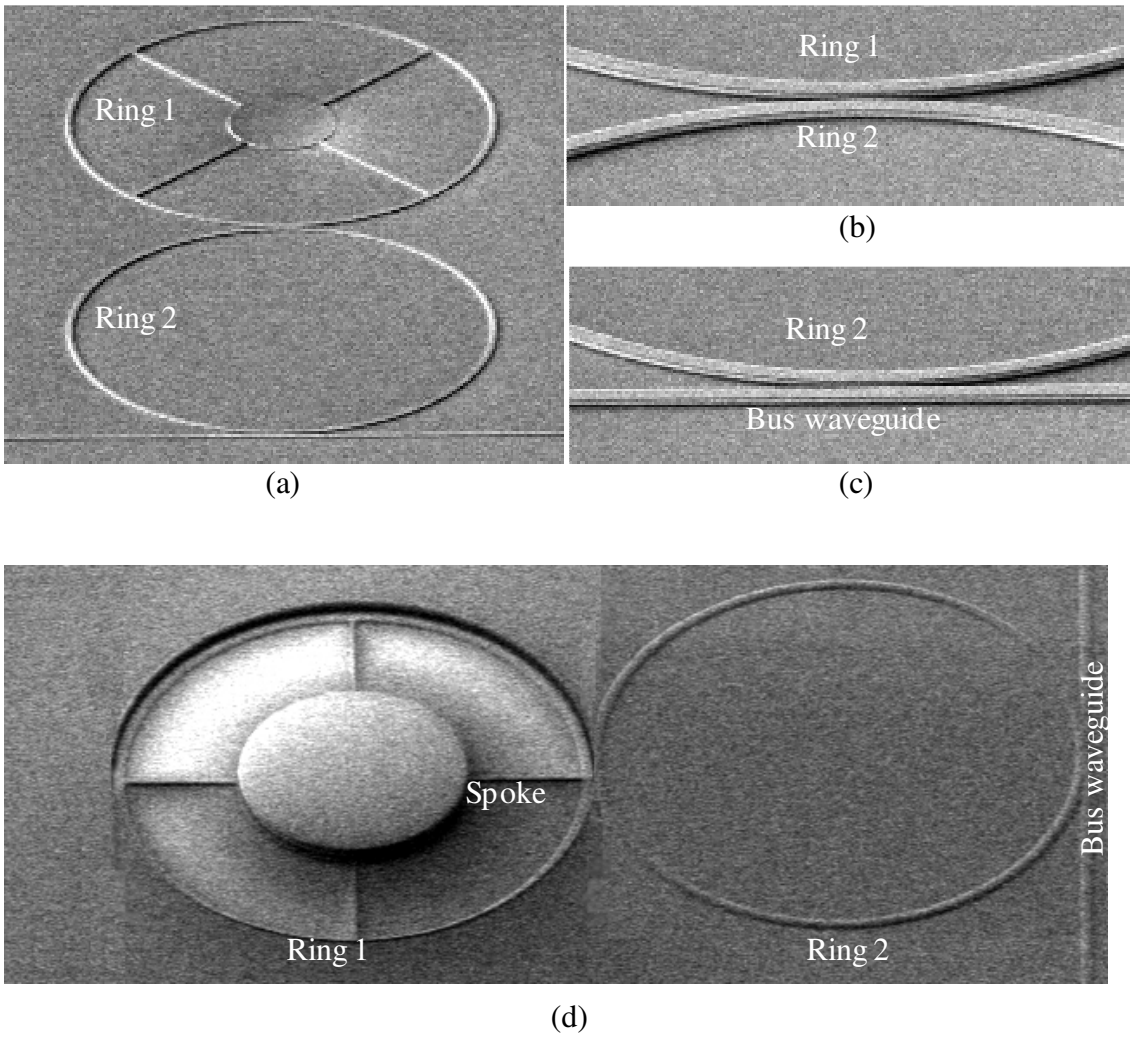

Figure 5.19: The SEM image of (a) the CRIT system without released ring; (b) ring-ring coupling region; (c) ring-waveguide coupling region; and (d) the tunable CRIT system.

5.4.1 Tunable CRIT system

The tunable CRIT system is fabricated by RIE fabrication process, and consists of a bus waveguide, a released ring resonator and a fixed ring resonator as shown in Fig. 5.19. The fabricated rings have a radius of 50 μm, a width of 0.45μm and a height of 0.22 μm. The spokes have a height of 0.22 μm, a width of 0.5 μm and a length of 40 μm. The bus waveguide has a width of 0.45μm and a length of 3mm. The ring-ring gap and the ring-waveguide gap are 200 nm.

In the experimental setup, the automatic fiber alignment system is used for light input and output. This equipment can do the alignment between the tapered fiber and the on chip bus waveguide. In experiments, one tapered fiber is used for light input and the other tapered fiber is used for output detection. Others equipments, such as optical spectrum analyzer (OSA), superluminescence light emitting diode (SLED), tunable laser, power meter are also used in the experiments.

5.4.2 Transmittivity measurement

As mentioned in the section 5.1.2, the transmittivity (T) illustrates the transmission of the tunable CRIT system. In order to characterize the tunable CRIT system, the transmittivity of the single ring resonator is measured. The single ring resonator has absorption peak when the collected phase is equal to $2m\pi$ (i.e. $\beta L = 2m\pi$). This results the optical path is equal to m times wavelength (i. e. $N_{eff}L = m\lambda$), and the free

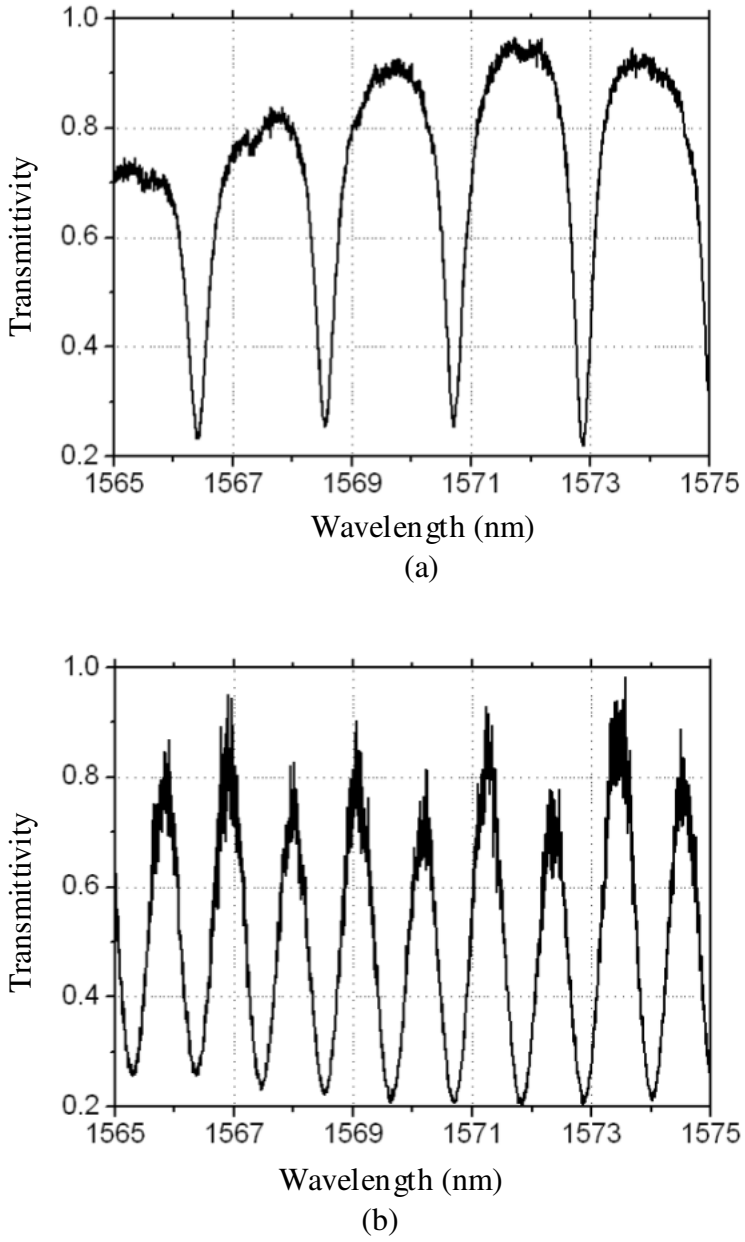

Figure 5.20 The transmittivity of (a) the single ring resonator with one bus waveguide; and (b) the unreleased double coupled ring resonator.

spectrum range (FSR) can be expressed as

$$FSR = \frac{\lambda^2}{2\pi R N_{eff}} \tag{5.27}$$

where R is the radius of the ring resonator. The transmittivity of the single ring resonator is shown in Fig. 5.20 (a). The probe light is the SLED which has central wavelength of 1570 nm and bandwidth of 100 nm. It can be seen that the single ring resonator has absorption peaks at 1566.41, 1568.55, 1570.71 and 1572.89 nm, and the FSRs in between of them are 2.14, 2.16 and 2.18 nm respectively. The Q-factor of the absorption peak is 4.5×10^3.

For the unreleased double coupled ring resonator, i.e., the tunable CRIT system before wet etching in HF, the transmittivity is shown in Fig. 5.20 (b). It shows that each absorption peak of the single ring resonator is degenerated into two symmetric peaks when there are two identical rings are coupled, which is coincide with the conclusion in numerical simulation. The Q-factor is decreased to 2.6×10^3 due to the longer optical path caused higher propagation loss on the rings.

After the wet etching, the degenerated peaks of tunable CRIT system become asymmetric as shown in Fig. 5.21, due to the difference between the coupled ring resonators. The theoretical analysis has been discussed in the section 5.2.2.

5.4.3 Measurement results

Through an optical coupler, the control light and the probe light are both coupled into the bus waveguide by the tapered fiber. The probe light is still the SLED, which has power of 2μW/nm, and the control light is the tunable laser, which has output power

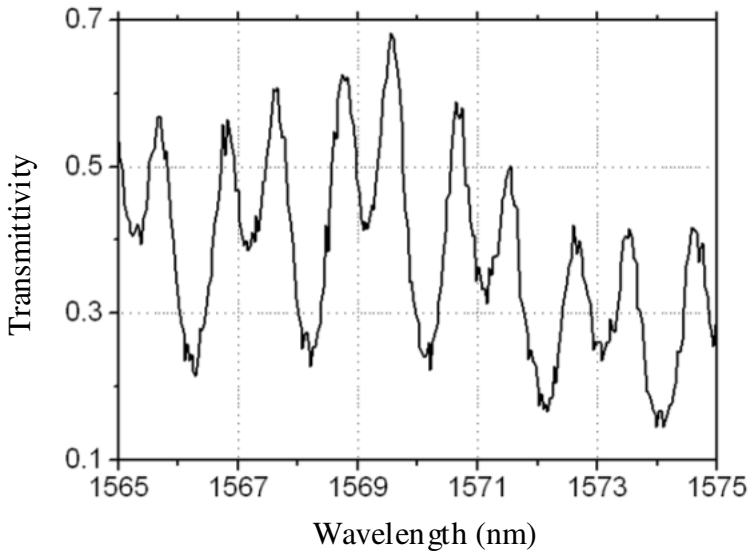

Figure 5.21: The transmittivity of the tunable CRIT system.

varying from 1 mW to 10 mW, linewidth of 0.05 nm, and wavelength tuning resolution of 0.01 nm. Compared to the power of the control laser, the power of SLED is negligible. Firstly, the control laser is chosen at a resonant wavelength, i.e. at this wavelength the system has highest absorption, but this wavelength is out of the detection region, e.g. from 1565 nm to 1575 nm. For instance, the transmittivity at wavelength of 1584.11 nm has local minimum as 0.22, which means that the control laser can use this wavelength.

When the control laser has wavelength of 1584.11 nm, the transmittivity of the CRIT system is tuned by the power of the control laser correspondingly, as shown in Fig. 5.22 (a). It can be seen that the absorption peaks have a redshift when the power of the control laser is increased from 0 to 10 mW, and the transmittivity is varied, e.g. from 0.28 to 0.61 at the wavelength of 1570 nm. However, the variation of the transmittivity is wavelength dependent as shown in Fig. 5.22 (b). When the wavelength is equal to 1569 nm and the input power is increased, the transmittivity increases firstly, reaches

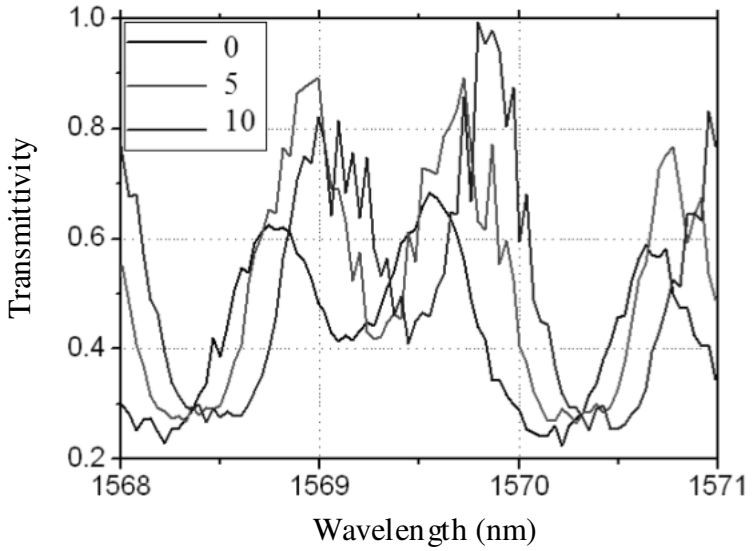

(a)

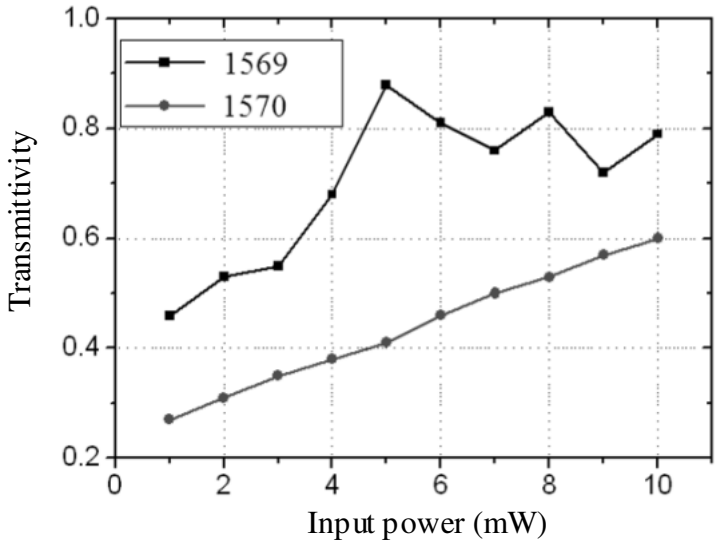

(b)

Figure 5.22: The curves of the transmittivity versus (a) the wavelength with input powers of 0, 5 and 10 mW; and (b) the input power at wavelength of 1569 and 1570 nm.

maximum value at P_{in} = 5 mW, thereafter, decreases. The tuning ratio of the transmittivity can be calculated based on the results, e.g. 1.7×10^2 W^{-1} at the wavelength of 1569 nm and input power of 4.5 mW. When the wavelength is equal to 1570 nm, to increase the input power, the transmittivity is increased.

5.5 Summary

A tunable ring-resonators-based CRIT system, which is driven by optical force between the ring resonator ant the substrate, is designed, analyzed, simulated, fabricated and demonstrated in this chapter. The tunable CRIT system consists of a bus waveguide and two coupled ring resonators, in which one is the released ring and the other is the fixed ring. The optical force between the released ring and the substrate is produced by the input power, which corresponds to different final deformations, changes the optical field buildup, shifts the transmission spectrum, and varies the group delay. Numerical results show that the tuning ratio of optical field buildup reaches 4.1×10^{4} W^{-1}, the tuning ratio of transmittivity reaches -3.6×10^{3} W^{-1} when the original gap is 300 nm, and the tuning ratio of group delay reaches 1.7 $\mu s W^{-1}$ when the original gap is 200 nm. The experimental results show that the fabricated tunable CRIT system is tuned by the input power through the optical force. A tuning ratio of the transmittivity with value of 1.7×10^{2} W^{-1} at λ = 1569 nm and P_{in} = 4.5 mW is achieved. This optical force based tunable CRIT system has potential applications in optical switch, optical storage and slow light areas.

CHAPTER 6

CONCLUSIONS AND RECOMMENDATIONS

6.1 Conclusions

In this PhD thesis, the nano-opto-mechanical systems (NOMS) is explored and two NOMS devices are designed, theoretically analyzed and numerically simulated. The *angular momentum generator* (AMG) is designed for nanoparticle trapping and rotation. The *tunable coupled-resonator-induced* (CRIT) *system* is designed for the tuning of the optical field buildup, the transmittivity and the group delay.

The AMG consisting of a ring resonator, a waveguide and a group of nano-rods is designed, theoretically analyzed and numerically simulated. The nanorod's effects on light coupling are discussed firstly. A nanorod between the waveguide and the ring increases the coupling coefficient, and affects the circulating light intensity inside the ring. Then, the generation of angular momentum is theoretically analyzed and numerically simulated. The theoretical analysis and the numerical results show that a series of l-order ROFs are generated when different resonant wavelengths are coupled into the generator. The order number of the generated ROFs is equal to the difference between n and N ($l = |n - N|$). Except the 0-order ROF, other ROFs have angular momenta but no linear momenta along the axis of rotation. The rotation direction is opposite to the light circulation direction when $n < N$, and they are same when $n > N$. Finally, the generation efficiency, the effects of nanorod on generation, and the 3D optical field distribution are discussed. The generation efficiency is affected by the wavelength, the number of rods as well as the refractive index. The number and the

diameter as well as the locations of these nanorods have an optimized value to achieve the highest generation efficiency. The maximum amplitude of generated fields could be 10-fold higher than that of the input field. The angular momentum generator overcomes the complication of linear momentum to the rotation of the small particles and provides a compact and flexible platform to study the rotational behaviors in micro-scale.

Then, *the optical force, the optical potential and the optical torque* of the generated ROF are derived, theoretically analyzed, numerically simulated and discussed. The optical force includes two terms. The first term is represented by the divergence of the Maxwell stress tensor, and the second term is the change of energy flux, which can be represented by the time derivative of the Poynting vector. The numerical results show that the first term is 6-order of magnitude higher than the second term. Thus, in most cases, the second term is negligible. The generated ROF as well as the corresponding optical force are affected by the existence of the nano-rotor. Compared to the ROF without the nano-rotor, the maximum values of E_x, E_z, H_y and S_T are enlarged, the space between two neighboring radial maxima of E_x, E_z and H_y are decreased, and the gradient of E_x, E_z, H_y and S_T along the y-axis are increased. The maximum optical force is also increased and the force distributions are changed due to the existence of the nano-rotor. Different angular orders of the generated ROF are associated with the different resultant force values and distributions. When l is increased from 0 to 3, the maximum resultant force in the xz-plane at $y = 0$ μm is decreased. The resultant force tends to push a small particle to the regions with highest light intensity, and the region is usually a circle. When the angular order is increased, the radius of the circle is increased, e.g. 213nm at $l = 0$, 181 nm at $l = 1$, 358 nm at $l = 2$ and 380 nm at $l = 3$. At $l = 2$, the circle is degenerated

into four individual regions due to the backscattering. The optical potential is calculated based on the resultant force, and the minimum optical potential has smallest value at l = 0, i.e. the corresponding optical field has highest particle trapping capability.

The optical torques are analyzed and discussed in the different objects, i.e. spherical nano-particle, nano-wire and nano-rotor. The optical torque drives the nano-particle to rotate in clockwise direction and it is located on the circle with radius from 0 to 220 nm, and in anticlockwise direction from 220 to 440 nm. For nano-wire, the optical torque drives it to rotate in clockwise direction when its length is in the range from 0 to 600 nm and 1120 nm to 1200 nm, and rotate in anticlockwise direction from 600 nm to 1120 nm. When the nano-wire has a length of 880 nm, the nano-wire is driven with the highest efficiency. For the nano-rotor, when l = 1 and the radius is approximately 0.44 μm, there is a maximum total optical torque on it. When the designed nano-rotor has radius of 0.5 μm, the 3-order ROF has the highest driving efficiency. However, the 3-order ROF becomes inefficient to drive a small nano-rotor with radius less than 0.3 μm. But for the 1-order ROF, the threshold radius is decreased to 0.1 μm. The 2-order ROF has driving capability in between of the 1- and 3-order ROF.

Finally, the *tunable ring-resonators-based CRIT system*, which is driven by optical force between the ring resonator and the substrate, is designed, theoretically analyzed, numerically simulated, fabricated and demonstrated. The tunable CRIT system consists of a bus waveguide and two coupled ring resonators, in which one is the released ring and the other is the fixed ring. The optical force between the released ring and the substrate is produced by the input power, which corresponds to different final

deformations, changes the optical field buildup, shifts the transmission spectrum, and varies the group delay. Numerical results show that the tuning ratio of optical field buildup reaches 4.1×10^{4} W^{-1}, the tuning ratio of transmittivity reaches -3.6×10^{3} W^{-1} when the original gap is 300 nm, and the tuning ratio of group delay reaches 1.7 $\mu s W^{-1}$ when the original gap is 200 nm. The experimental results show that the fabricated tunable CRIT system is successfully tuned by the input power through the optical force. A tuning ratio of the transmittivity with value of 1.7×10^{2} W^{-1} at $\lambda = 1569$ nm and $P_{in} = 4.5$ mW is achieved. The optical force based tunable CRIT system has potential applications in optical switch, optical storage and slow light etc.

6.2 Recommendations

The recommendations for future research are summarized as follows:

(a) In the analysis of the working principles of the AMG, the scattering lights from the group of nano rods are majorly considered with the phases. However, the amplitudes of the scattering light also affect the generation efficiencies. Therefore, an accurate theoretical description of the scattering light from the nano rods is desired. This theoretical mode should involve the shapes, the material properties and the locations of the nanoparticle. Based on the theoretical mode, the intensity of generated ROF at arbitrary point can be predicted. Furthermore, the shape and the material properties of the nano rods can also be optimized by using this theoretical mode.

(b) The multi-scattering effect is ignored in the theoretical analysis of the AMG. However, when the number of nano rods is large enough, the distance between two neighboring nanorods is smaller than the light wavelength. The effect of multi-scattering becomes significant, which is same as the Bragg grating effect. The higher generation efficiency of the AMG might be obtained under this condition. In addition, the generation efficiency discussed in this thesis is majorly in the 2D plane (xz – plane). The 3D distribution of the optical field is affected by the radius of the optical ring resonator in the AMG. Therefore, the radius of the ring can be further optimized for desired 3D optical field distributions.

(c) The optical force distribution, the optical potential and the optical torque of the generated ROFs have been discussed in this thesis. However, for some specific applications, these information is not sufficient, e.g., the rotation of the adenosine-5'-triphosphate (ATP). Further theoretical analysis and experimental testing are recommended to be carried out in the biological area. It is because the designed AMG has potential application in vivo experiments due to its high integratibility.

(d) The tunable ring-resonators-based CRIT system is achieved in this PhD thesis. However, the ring-resonators-based CRIT is only one of CRIT systems. There are lots of other systems which have obvious CRIT, such as coupled two spheres, coupled two nano cantilever oscillators, one mechanical oscillator coupled with one optical resonator. Further optical tuning CRIT can be designed in these systems.

(e) Due to multiple stability points, the tunable ring-resonators-based CRIT system can be used to study the thermo-quantum effects. The vibration caused by the thermo effect at the nano scale is uncertain. Therefore, the thermo effect on the tunable CRIT system can be measured by these stability points, which correspond to several discrete energy levels.

AUTHOR'S PUBLICATIONS

Journal papers

1. Y. F. Yu, Y. H. Fu, X. M. Zhang, A. Q. Liu, T. Bourouina, T. Mei, Z. X. Shen and D. P. Tsai, "Pure angular momentum generator using a ring resonator", Opt. Express, Vol. 18, Issue 21, 2010.
2. L. A. G. Lin, A. Q. Liu, Y. F. Yu, C. Zhang, C. S. Lim, S. H. Ng,P. H. Yap and H. J. Gao, "Cell Compressibility Studies Utilizing Non-Contact Hydrostatic Pressure Measurements on Single Living Cells in a Micro-chamber". App. Phys. Lett., 92(233901), 2008.
3. Q. Liu, H. J. Huang, L. K. Chin, Y. F. YU and X. C. Li, "A Review: Label-Free Detection with Micro-Opto-Fluidic-System (MOFS)", J. Anal. Bioanal. Chem., 391(7), 2443-2452, 2008.
4. Y. F. YU, A. Q. Liu, L. K. Chin, H. Cai and T. Bourouina, "Coupled-resonator-induced transparency (CRIT) tuning via optical force", Phys. Rev. Lett., 2011 (submitted).
5. Y. F. YU, A. Q. Liu, L. K. Chin, H. Cai, and T. Bourouina, "Nanoparticle trapping and rotation by using of rotating optical field (ROF)", Nano letters, 2011 (submitted).

Conference papers

1. Y. F. Yu, V. Kanna, T. Bourouina, S. H. Ng, P. H. Yap and A.Q. Liu. "An on-chip glass sphere resonator for label-free detection". 23th IEEE International Conference on Micro-Electro-Mechanical Systems (MEMS), 2010.

2. Y. F. Yu, T. Bourouina, S. H. Ng, P. H. Yap and A. Q. Liu. "A single droplet carrier with optical detector". 13th International Conference on Miniaturized Systems for Chemistry and Life Sciences (uTAS), 2009.
3. Y. F. Yu, T. Bourouina and A. Q. Liu, "On-chip droplet enhanced fluorescence emission for low concentration protein measurement", The 15th International Conference on Solid-State Sensors, Actuators and Microsystems (Transducers), 2009.
4. Y. F. Yu, T. Bourouina, and A. Q. Liu, "A micro-fluidic-optical switch using multi-droplet resonators array", The 15th International Conference on Solid-State Sensors, Actuators and Microsystems (Transducers), 2009.
5. Y. F. Yu, T. Bourouina, C. S. Lim, M. K. Chin and A. Q. Liu, "High sensitivity sessile droplet resonator for low concentration protein detection", 12th International Conference on Miniaturized Systems for Chemistry and Life Sciences (uTAS), 2008.

Bibliography

1. A. Q. Liu and X. M. Zhang, "A review of MEMS external-cavity tunable lasers," J. Micromech. Microeng. **17**, R1-R13 (2007).
2. X. M. Zhang, Q. W. Zhao, A. Q. Liu, J. Zhang, J. H. Lau, and C. H. Kam, "Asymmetric tuning schemes of MEMS dual-shutter VOA," J. Lightwave Technol. **26**, 569-579 (2008).
3. X. M. Zhang, A. Q. Liu, C. Lu, and D. Y. Tang, "MEMS variable optical attenuator using low driving voltage for DWDM systems," Electron. Lett. **38**, 382-383 (2002).
4. H. Cai, X. M. Zhang, C. Lu, A. Q. Liu, and E. H. Khoo, "Linear MEMS variable optical attenuator using reflective elliptical mirror," IEEE Photonics Technol. Lett. **17**, 402-404 (2005).
5. H. G. Craighead, "Nanoelectromechanical systems," Science **290**, 1532-1535 (2000).
6. V. R. Almeida, R. R. Panepucci, and Ieee, *Nano-Opto-Electro-Mechanical devices based on Silicon Slot-Waveguides Structures*, 2009 Sbmo/Ieee Mtt-S International Microwave and Optoelectronics Conference (Ieee, New York, 2009), pp. 550-553.
7. M. Li, W. H. P. Pernice, C. Xiong, T. Baehr-Jones, M. Hochberg, and H. X. Tang, "Harnessing optical forces in integrated photonic circuits," Nature **456**, 480-U428 (2008).
8. G. S. Wiederhecker, L. Chen, A. Gondarenko, and M. Lipson, "Controlling photonic structures using optical forces," Nature **462**, 633-636 (2009).
9. F. Marquardt, A. A. Clerk, and S. M. Girvin, "Quantum theory of optomechanical cooling," J. Mod. Opt. **55**, 3329-3338 (2008).
10. M. Blencowe, "Nanomechanical quantum limits," Science **304**, 56-57 (2004).

11. P. H. Jones, F. Palmisano, F. Bonaccorso, P. G. Gucciardi, G. Calogero, A. C. Ferrari, and O. M. Marago, "Rotation Detection in Light-Driven Nanorotors," ACS Nano **3**, 3077-3084 (2009).
12. N. Koumura, E. M. Geertsema, A. Meetsma, and B. L. Feringa, "Light-driven molecular rotor: Unidirectional rotation controlled by a single stereogenic center," J. Am. Chem. Soc. **122**, 12005-12006 (2000).
13. L. M. Tong, V. D. Miljkovic, and M. Kall, "Alignment, Rotation, and Spinning of Single Plasmonic Nanoparticles and Nanowires Using Polarization Dependent Optical Forces," Nano Letters **10**, 268-273 (2010).
14. M. Liu, T. Zentgraf, Y. Liu, G. Bartal, and X. Zhang, "Light-driven nanoscale plasmonic motors," Nat Nano **5**, 570-573 (2010).
15. B. E. Little, S. T. Chu, H. A. Haus, J. Foresi, and J. P. Laine, "Microring resonator channel dropping filters," J. Lightwave Technol. **15**, 998-1005 (1997).
16. B. E. Little, J. S. Foresi, G. Steinmeyer, E. R. Thoen, S. T. Chu, H. A. Haus, E. P. Ippen, L. C. Kimerling, and W. Greene, "Ultra-compact Si-SiO2 microring resonator optical channel dropping filters," IEEE Photonics Technol. Lett. **10**, 549-551 (1998).
17. L. K. Chin, A. Q. Liu, C. S. Lim, X. M. Zhang, J. H. Ng, J. Z. Hao, and S. Takahashi, "Differential single living cell refractometry using grating resonant cavity with optical trap," App. Phys. Lett.**91**, 3 (2007).
18. K. J. Vahala, "Optical microcavities," Nature **424**, 839-846 (2003).
19. J. M. Gerard, B. Sermage, B. Gayral, B. Legrand, E. Costard, and V. Thierry-Mieg, "Enhanced spontaneous emission by quantum boxes in a monolithic optical microcavity," Phys. Rev. Lett. **81**, 1110-1113 (1998).

20. Y. Akahane, T. Asano, B. S. Song, and S. Noda, "High-Q photonic nanocavity in a two-dimensional photonic crystal," Nature **425**, 944-947 (2003).
21. O. Painter, R. K. Lee, A. Scherer, A. Yariv, J. D. O'Brien, P. D. Dapkus, and I. Kim, "Two-dimensional photonic band-gap defect mode laser," Science **284**, 1819-1821 (1999).
22. M. Cai, O. Painter, K. J. Vahala, and P. C. Sercel, "Fiber-coupled microsphere laser," Opt. Lett. **25**, 1430-1432 (2000).
23. A. C. Tamboli, E. D. Haberer, R. Sharma, K. H. Lee, S. Nakamura, and E. L. Hu, "Room-temperature continuous-wave lasing in GaN/InGaN microdisks," Nat. Photonics **1**, 61-64 (2007).
24. H. Y. Zhu, I. M. White, J. D. Suter, M. Zourob, and X. D. Fan, "Integrated refractive index optical ring resonator detector for capillary electrophoresis," Anal. Chem. **79**, 930-937 (2007).
25. A. M. Armani, R. P. Kulkarni, S. E. Fraser, R. C. Flagan, and K. J. Vahala, "Label-free, single-molecule detection with optical microcavities," Science **317**, 783-787 (2007).
26. A. N. Oraevsky, "Whispering-gallery waves," Quantum Electronics **32**, 377-400 (2002).
27. R. Symes, R. M. Sayer, and J. P. Reid, "Cavity enhanced droplet spectroscopy: Principles, perspectives and prospects," Phys. Chem. Chem. Phy. **6**, 474-487 (2004).
28. Y. H. Ja, "Generalized theory of optical fiber loop and ring resonators with multiple couplers .1. Circulating and output fields," App. Opt. **29**, 3517-3523 (1990).
29. L. F. Stokes, M. Chodorow, and H. J. Shaw, "All-single-mode fiber resonator," Opt. Lett. **7**, 288-290 (1982).

30. Y. H. Ja, "Optical fiber loop resonators with double couplers," Opt. Commun. **75**, 239-245 (1990).
31. Y. H. Ja, "Generalized theory of optical fiber loop and ring resonators with multiple couplers .2. general-characteristics," App. Opt. **29**, 3524-3529 (1990).
32. A. W. Snyder, "Coupled-mode theory for optical fibers," Journal of the Optical Society of America **62**, 1267-1277 (1972).
33. A. L. Jones, "Coupling of optical fibers and scattering in fibers," J. Opt. Soc. Am. **55**, 261-& (1965).
34. L. Xiao and T. A. Birks, "High finesse microfiber knot resonators made from double-ended tapered fibers," Opt. Lett. **36**, 1098-1100 (2011).
35. X. Jiang, Y. Chen, G. Vienne, and L. Tong, "All-fiber add-drop filters based on microfiber knot resonators," Opt. Lett. **32**, 1710-1712 (2007).
36. Z. Y. Zhang, M. Dainese, L. Wosinski, and M. Qiu, "Resonance-splitting and enhanced notch depth in SOI ring resonators with mutual mode coupling," Opt. Express **16**, 4621-4630 (2008).
37. D. X. Xu, M. Vachon, A. Densmore, R. Ma, S. Janz, A. Delâge, J. Lapointe, P. Cheben, J. H. Schmid, E. Post, S. Messaoudène, and J.-M. Fédéli, "Real-time cancellation of temperature induced resonance shifts in SOI wire waveguide ring resonator label-free biosensor arrays," Opt. Express **18**, 22867-22879 (2010).
38. T. Wang, Z. Y. Zhang, F. F. Liu, Y. Tong, J. Wang, Y. Tian, M. Qiu, and Y. K. Su, "Modeling of quasi-grating sidewall corrugation in SOI microring add-drop filters," Opt. Commun. **282**, 3464-3467 (2009).
39. J. P. Guo, M. J. Shaw, G. A. Vawter, P. Esherick, G. R. Hadley, C. T. Sullivan, and ieee, "High-Q integrated on-chip micro-ring resonator," in *2004 Ieee Leos Annual*

Meeting Conference Proceedings, Vols 1 and 2 (Ieee, New York, 2004), pp. 745-746.

40. A. Gondarenko, J. S. Levy, and M. Lipson, "High confinement micron-scale silicon nitride high Q ring resonator," Opt. Express **17**, 11366-11370 (2009).
41. Q. Xu, D. Fattal, and R. G. Beausoleil, "Silicon microring resonators with 1.5-?m radius," Opt. Express **16**, 4309-4315 (2008).
42. P. Rabiei, W. H. Steier, C. Zhang, and L. R. Dalton, "Polymer micro-ring filters and modulators," J. Lightwave Technol. **20**, 1968-1975 (2002).
43. D. K. Armani, T. J. Kippenberg, S. M. Spillane, and K. J. Vahala, "Ultra-high-Q toroid microcavity on a chip," Nature **421**, 925-928 (2003).
44. T. Aoki, B. Dayan, E. Wilcut, W. P. Bowen, A. S. Parkins, T. J. Kippenberg, K. J. Vahala, and H. J. Kimble, "Observation of strong coupling between one atom and a monolithic microresonator," Nature **443**, 671-674 (2006).
45. A. M. Armani, D. K. Armani, B. Min, K. J. Vahala, and S. M. Spillane, "Ultra-high-Q microcavity operation in H2O and D2O," App. Physics Lett. **87**, 3 (2005).
46. S. Lin, E. Schonbrun, and K. Crozier, "Optical Manipulation with Planar Silicon Microring Resonators," Nano Letters **10**, 2408-2411 (2010).
47. R. Waldhäusl, B. Schnabel, P. Dannberg, E.-B. Kley, A. Bräuer, and W. Karthe, "Efficient Coupling into Polymer Waveguides by Gratings," Appl. Opt. **36**, 9383-9390 (1997).
48. C. Manolatou, M. J. Khan, S. H. Fan, P. R. Villeneuve, H. A. Haus, and J. D. Joannopoulos, "Coupling of modes analysis of resonant channel add-drop filters," IEEE J. Quantum Electron. **35**, 1322-1331 (1999).

49. M. T. Hill, H. J. S. Dorren, T. de Vries, X. J. M. Leijtens, J. H. den Besten, B. Smalbrugge, Y. S. Oei, H. Binsma, G. D. Khoe, and M. K. Smit, "A fast low-power optical memory based on coupled micro-ring lasers," Nature **432**, 206-209 (2004).

50. J. Wang, Y. C. Zhang, A. Malacarne, M. Yao, L. Poti, and A. Bogoni, "SOA Fiber Ring Laser-Based Three-State Optical Memory," IEEE Photonics Technol. Lett. **20**, 1697-1699 (2008).

51. L. Y. Mario, S. Darmawan, and M. K. Chin, "Asymmetric Fano resonance and bistability for high extinction ratio, large modulation depth, and low power switching," Opt. Express **14**, 12770-12781 (2006).

52. K. Djordjev, S. J. Choi, and P. D. Dapkus, "Microdisk tunable resonant filters and switches," IEEE Photonics Technol. Lett. **14**, 828-830 (2002).

53. J. E. Heebner, R. W. Boyd, and Q. H. Park, "Slow light, induced dispersion, enhanced nonlinearity, and optical solitons in a resonator-array waveguide," Phys. Rev. E **65**, 036619 (2002).

54. J. Wang, Y. Zhang, J. Zhang, Y. Cai, X. Zhang, and P. Yuan, "Simultaneous observation of superluminal and slow light propagation in a nested fiber ring resonator," Opt. Express **18**, 13180-13186 (2010).

55. J. V. Hryniewicz, P. P. Absil, B. E. Little, R. A. Wilson, and P. T. Ho, "Higher order filter response in coupled microring resonators," IEEE Photonics Technol. Lett. **12**, 320-322 (2000).

56. L. Y. M. Tobing, P. Dumon, R. Baets, and M. K. Chin, "Boxlike filter response based on complementary photonic bandgaps in two-dimensional microresonator arrays," Opt. Lett. **33**, 2512-2514 (2008).

57. M. T. Hill, S. Anantathanasarn, Y. Zhu, Y. S. Oei, P. J. van Veldhoven, M. K. Smit, and R. Notzel, "InAs-InP (1.55-mu m region) quantum-dot microring lasers," IEEE Photonics Technol. Lett. **20**, 446-448 (2008).

58. K. Totsuka, N. Kobayashi, and M. Tomita, "Slow Light in Coupled-Resonator-Induced Transparency," Phys. Rev. Lett. **98**, 213904 (2007).

59. J. Scheuer, G. T. Paloczi, J. K. S. Poon, and A. Yariv, "Coupled Resonator Optical Waveguides: Toward the Slowing and Storage of Light," Opt. Photon. News **16**, 36-40 (2005).

60. F. N. Xia, L. Sekaric, and Y. Vlasov, "Ultracompact optical buffers on a silicon chip," Nat. Photonics **1**, 65-71 (2007).

61. M. L. Gorodetsky, A. D. Pryamikov, and V. S. Ilchenko, "Rayleigh scattering in high-Q microspheres," J. Opt. Soc. Am. B-Opt. Phys. **17**, 1051-1057 (2000).

62. A. Mazzei, S. Goetzinger, L. D. Menezes, G. Zumofen, O. Benson, and V. Sandoghdar, "Controlled coupling of counterpropagating whispering-gallery modes by a single Rayleigh scatterer: A classical problem in a quantum optical light," Phys. Rev. Lett. **99**(2007).

63. B. E. Little, J. P. Laine, and S. T. Chu, "Surface-roughness-induced contradirectional coupling in ring and disk resonators," Opt. Lett. **22**, 4-6 (1997).

64. M. Fujita and T. Baba, "Microgear laser," App. Phys. Lett. **80**, 2051-2053 (2002).

65. V. M. N. Passaro, F. De Leonardis, and G. Z. Mashanovich, "Investigation of coupling conditions in microgear resonators," Opt. Express **15**, 797-808 (2007).

66. B. E. Little, S. T. Chu, and H. A. Haus, "Second-order filtering and sensing with partially coupled traveling waves in a single resonator," Opt. Lett. **23**, 1570-1572 (1998).

67. M. Fujita and T. Baba, "Proposal and finite-difference time-domain simulation of whispering galley mode microgear cavity," IEEE J. Quantum Electron. **37**, 1253-1258 (2001).

68. J. G. Zhu, S. K. Ozdemir, Y. F. Xiao, L. Li, L. N. He, D. R. Chen, and L. Yang, "On-chip single nanoparticle detection and sizing by mode splitting in an ultrahigh-Q microresonator," Nat. Photonics **4**, 46-49 (2010).

69. D. D. Smith, H. R. Chang, and K. A. Fuller, "Whispering-gallery mode splitting in coupled microresonators," J. Opt. Soc. Am. B-Opt. Phys. **20**, 1967-1974 (2003).

70. S. Yang and V. N. Astratov, "Spectroscopy of coherently coupled whispering-gallery modes in size-matched bispheres assembled on a substrate," Opt. Lett. **34**, 2057-2059 (2009).

71. L. Tobing, P. Dumon, R. Baets, D. C. S. Lim, and M. K. Chin, "The transmission properties of one-bus two-ring devices," IEICE Trans. Electron. E91C, 167-172 (2008).

72. W. H. P. Pernice, M. Li, K. Y. Fong, and H. X. Tang, "Modeling of the optical force between propagating lightwaves in parallel 3D waveguides," Opt. Express **17**, 16032-16037 (2009).

73. J. P. Gordon, "Radiation Forces and Momenta in Dielectric Media," Phys. Rev. A **8**, 14 (1973).

74. S. Gigan, H. R. Bohm, M. Paternostro, F. Blaser, G. Langer, J. B. Hertzberg, K. C. Schwab, D. Bauerle, M. Aspelmeyer, and A. Zeilinger, "Self-cooling of a micromirror by radiation pressure," Nature **444**, 67-70 (2006).

75. Y. Harada and T. Asakura, "Radiation forces on a dielectric sphere in the Rayleigh scattering regime," Opt. Commun. **124**, 529-541 (1996).

76. H. Y. Jaising and O. G. Helleso, "Radiation forces on a Mie particle in the evanescent field of an optical waveguide," Opt. Commun. **246**, 373-383 (2005).

77. A. Ashkin, J. M. Dziedzic, J. E. Bjorkholm, and S. Chu, "Observation of a single-beam gradient force optical trap for dielectric particles," Opt. Lett. **11**, 288-290 (1986).

78. K. T. Gahagan and G. A. Swartzlander, "Optical vortex trapping of particles," Opt. Lett. **21**, 827-829 (1996).

79. M. Padgett, J. Courtial, and L. Allen, "Light's orbital angular momentum," Phys. Today **57**, 35-40 (2004).

80. X. D. He, P. Xu, J. Wang, and M. S. Zhan, "Rotating single atoms in a ring lattice generated by a spatial light modulator," Opt. Express **17**, 21007-21014 (2009).

81. M. Siler, T. Cizmar, M. Sery, and P. Zemanek, "Optical forces generated by evanescent standing waves and their usage for sub-micron particle delivery," Appl. Phys. B-Lasers Opt. **84**, 157-165 (2006).

82. M. L. Povinelli, M. Loncar, M. Ibanescu, E. J. Smythe, S. G. Johnson, F. Capasso, and J. D. Joannopoulos, "Evanescent-wave bonding between optical waveguides," Opt. Lett. **30**, 3042-3044 (2005).

83. A. H. J. Yang and D. Erickson, "Optofluidic ring resonator switch for optical particle transport," Lab on a Chip **10**, 769-774 (2010).

84. D. Erickson, X. Serey, Y.-F. Chen, and S. Mandal, "Nanomanipulation using near field photonics," Lab on a Chip **11**, 995-1009 (2011).

85. X. Serey, S. Mandal, and D. Erickson, "Comparison of silicon photonic crystal resonator designs for optical trapping of nanomaterials," Nanotechnology **21**(2010).

86. M. L. Povinelli, S. G. Johnson, M. Loncar, M. Ibanescu, E. J. Smythe, F. Capasso, and J. D. Joannopoulos, "High-Q enhancement of attractive and repulsive optical

forces between coupled whispering-gallery-mode resonators," Opt. Express **13**, 8286-8295 (2005).

87. M. Li, W. H. P. Pernice, and H. X. Tang, "Ultrahigh-frequency nano-optomechanical resonators in slot waveguide ring cavities," App. Phys. Lett. **97**(2010).
88. A. Ashkin, "History of optical trapping and manipulation of small-neutral particle, atoms, and molecules," IEEE Journal Of Selected Topics In Quantum Electronics **6**, 841-856 (2000).
89. D. G. Grier, "A revolution in optical manipulation," Nature **424**, 810-816 (2003).
90. A. Ashkin, "Atomic-Beam Deflection by Resonance-Radiation Pressure," Phys. Rev. Lett. **25**, 1321 (1970).
91. T. W. Hansch and A. L. Schawlow, "Cooling of gases by laser radiation," Opt. Commun. **13**, 68-69 (1975).
92. S. Chu, J. E. Bjorkholm, A. Ashkin, and A. Cable, "Experimental observation of optically trapped atoms," Phys. Rev. Lett. **57**, 314 (1986).
93. A. Ashkin and J. M. Dziedzic, "Optical trapping and manipulation of viruses and bacteria," Science **235**, 1517-1520 (1987).
94. P. Mangeol, D. Cote, T. Bizebard, O. Legrand, and U. Bockelmann, "Probing DNA and RNA single molecules with a double optical tweezer," Eur. Phys. J. E **19**, 311-317 (2006).
95. K. Svoboda and S. M. Block, "Force and velocity measured for single kinesin molecules," Cell **77**, 773-784 (1994).
96. C. Huang and L. Zhu, "Enhanced optical forces in 2D hybrid and plasmonic waveguides," Opt. Lett. **35**, 1563-1565 (2010).

97. M. Eichenfield, C. P. Michael, R. Perahia, and O. Painter, "Actuation of micro-optomechanical systems via cavity-enhanced optical dipole forces," Nat. Photonics **1**, 416-422 (2007).

98. D. Van Thourhout and J. Roels, "Optomechanical device actuation through the optical gradient force," Nat Photon **4**, 211-217 (2010).

99. M. Li, W. H. P. Pernice, and H. X. Tang, "Tunable bipolar optical interactions between guided lightwaves," Nat. Photonics **3**, 464-468 (2009).

100. M. Eichenfield, R. Camacho, J. Chan, K. J. Vahala, and O. Painter, "A picogram- and nanometre-scale photonic-crystal optomechanical cavity," Nature **459**, 550-U579 (2009).

101. P. Measor, S. Kühn, E. J. Lunt, B. S. Phillips, A. R. Hawkins, and H. Schmidt, "Hollow-core waveguide characterization by optically induced particle transport," Opt. Lett. **33**, 672-674 (2008).

102. A. H. J. Yang and D. Erickson, "Stability analysis of optofluidic transport on solid-core waveguiding structures," Nanotechnology **19**(2008).

103. V. G. Shvedov, A. V. Rode, Y. V. Izdebskaya, A. S. Desyatnikov, W. Krolikowski, and Y. S. Kivshar, "Giant Optical Manipulation," Phys. Rev. Lett. **105**, 118103 (2010).

104. D. Kleckner and D. Bouwmeester, "Sub-kelvin optical cooling of a micromechanical resonator," Nature **444**, 75-78 (2006).

105. T. J. Kippenberg, H. Rokhsari, T. Carmon, A. Scherer, and K. J. Vahala, "Analysis of radiation-pressure induced mechanical oscillation of an optical microcavity," Phys. Rev. Lett. **95**(2005).

106. S. Weis, R. Riviere, S. Deleglise, E. Gavartin, O. Arcizet, A. Schliesser, and T. J. Kippenberg, "Optomechanically Induced Transparency," Science **330**, 1520-1523 (2010).

107. L. Allen, M. W. Beijersbergen, R. J. C. Spreeuw, and J. P. Woerdman, "Orbital angular-momentum of light and the transformation of laguerre-gaussian laser modes," Phys. Rev. A **45**, 8185-8189 (1992).

108. A. Ashkin, and J. M. Dziedzic, "Observation of Resonances in the Radiation Pressure on Dielectric Spheres," Phys. Rev. Lett. **38**, 5 (1977).

109. J. H. Poynting, "The wave motion of a revolving shaft, and a suggestion as to the angular momentum in a beam of circularly polarised light," Proc. R. soc. Lond. Ser. A-Contain. Pap. Math. Phys. Character **82**, 560-567 (1909).

110. R. A. Beth, "Mechanical detection and measurement of the angular momentum of light," Phys. Rev. **50**, 115-125 (1936).

111. A. T. O'Neil, I. MacVicar, L. Allen, and M. J. Padgett, "Intrinsic and Extrinsic Nature of the Orbital Angular Momentum of a Light Beam," Phys. Rev. Lett. **88**, 053601 (2002).

112. S. H. Simpson and S. Hanna, "Optical angular momentum transfer by Laguerre-Gaussian beams," J. Opt. Soc. Am. A-Opt. Image Sci. Vis. **26**, 625-638 (2009).

113. V. V. Kotlyar, V. A. Soifer, and S. N. Khonina, "Rotation of multimode Gauss-Laguerre light beams in free space," Tech. Phys. Lett. **23**, 657-658 (1997).

114. G. A. Turnbull, D. A. Robertson, G. M. Smith, L. Allen, and M. J. Padgett, "Generation of free-space Laguerre-Gaussian modes at millimetre-wave frequencies by use of a spiral phaseplate," Opt. Commun. **127**, 183-188 (1996).

115. S. N. Khonina, V. V. Kotlyar, V. A. Soifer, M. Honkanen, J. Lautanen, and J. Turunen, "Generation of rotating Gauss-Laguerre modes with binary-phase diffractive optics," J. Mod. Opt. **46**, 227-238 (1999).

116. J. E. Curtis, B. A. Koss, and D. G. Grier, "Dynamic holographic optical tweezers," Opt. Commun. **207**, 169-175 (2002).

117. S. Franke-Arnold, L. Allen, and M. Padgett, "Advances in optical angular momentum," Laser Photon. Rev. **2**, 299-313 (2008).

118. Y. Igasaki, F. H. Li, N. Yoshida, H. Toyoda, T. Inoue, N. Mukohzaka, Y. Kobayashi, and T. Hara, "High efficiency electrically-addressable phase-only spatial light modulator," Opt. Rev. **6**, 339-344 (1999).

119. Y. Torii, N. Shiokawa, T. Hirano, T. Kuga, Y. Shimizu, and H. Sasada, "Pulsed polarization gradient cooling in an optical dipole trap with a Laguerre-Gaussian laser beam," Eur. Phys. J. D **1**, 239-242 (1998).

120. S. Franke-Arnold, J. Leach, M. J. Padgett, V. E. Lembessis, D. Ellinas, A. J. Wright, J. M. Girkin, P. Ohberg, and A. S. Arnold, "Optical ferris wheel for ultracold atoms," Opt. Express **15**, 8619-8625 (2007).

121. S. H. Simpson and S. Hanna, "Rotation of absorbing spheres in Laguerre-Gaussian beams," J. Opt. Soc. Am. A-Opt. Image Sci. Vis. **26**, 173-183 (2009).

122. H. He, M. E. J. Friese, N. R. Heckenberg, and H. Rubinsztein-Dunlop, "Direct Observation of Transfer of Angular Momentum to Absorptive Particles from a Laser Beam with a Phase Singularity," Phys. Rev. Lett. **75**, 826 (1995).

123. M. E. J. Friese, T. A. Nieminen, N. R. Heckenberg, and H. Rubinsztein-Dunlop, "Optical alignment and spinning of laser-trapped microscopic particles," Nature **394**, 348-350 (1998).

124. K. Volke-Sepulveda, V. Garces-Chavez, S. Chavez-Cerda, J. Arlt, and K. Dholakia, "Orbital angular momentum of a high-order Bessel light beam," J. Opt. B-Quantum Semicl. Opt. **4**, S82-S89 (2002).

125. D. D. Smith, H. Chang, K. A. Fuller, A. T. Rosenberger, and R. W. Boyd, "Coupled-resonator-induced transparency," Phys. Rev. A **69**(2004).

126. Y. Zhang, S. Darmawan, L. Y. M. Tobing, T. Mei, and D. H. Zhang, "Coupled resonator-induced transparency in ring-bus-ring Mach-Zehnder interferometer," J. Opt. Soc. Am. B **28**, 28-36 (2011).

127. Y.-F. Xiao, X.-B. Zou, W. Jiang, Y.-L. Chen, and G.-C. Guo, "Analog to multiple electromagnetically induced transparency in all-optical drop-filter systems," Phys. Rev. A **75**, 063833 (2007).

128. C. L. G. Alzar, M. A. G. Martinez, and P. Nussenzveig, "Classical analog of electromagnetically induced transparency," Am. J. Phys. **70**, 37-41 (2002).

129. Y. S. Joe, A. M. Satanin, and C. S. Kim, "Classical analogy of Fano resonances," Phys. Scr. **74**, 259-266 (2006).

130. A. E. Miroshnichenko, S. Flach, and Y. S. Kivshar, "Fano resonances in nanoscale structures," Rev. of Modern Physics **82**, 2257-2298 (2010).

131. A. E. Çetin and Ã. E. MÃ¼stecaplÄ±oÄŸlu, "Electrically tunable Dicke effect in a double-ring resonator," Phys. Rev. A **81**, 043812 (2010).

132. D. D. Smith, N. N. Lepeshkin, A. Schweinsberg, G. Gehring, R. W. Boyd, Q. H. Park, H. Chang, and D. J. Jackson, "Coupled-resonator-induced transparency in a fiber system," Opt. Commun. **264**, 163-168 (2006).

133. Y. C. Chung, D. G. Kim, and N. Dagli, "Reflection properties of coupled-ring reflectors," J. Lightwave Technol. **24**, 1865-1874 (2006).

134. P. Rabiei and W. H. Steier, "Tunable polymer double micro-ring filters," IEEE Photonics Technol. Lett. **15**, 1255-1257 (2003).

135. S. Q. Feng, X. S. Luo, S. W. Du, and A. W. Poon, "Electro-optical tunable time delay and advance in a silicon feedback-microring resonator," Opt. Lett. **36**, 1278-1280 (2011).

136. A. Yariv, "Universal relations for coupling of optical power between microresonators and dielectric waveguides," Electron. Lett. **36**, 321-322 (2000).

137. Y. M. Landobasa, S. Darmawan, and M. K. Chin, "Matrix analysis of 2-D microresonator lattice optical filters," IEEE J. Quantum Electron. **41**, 1410-1418 (2005).

138. C. S. Ma, Y. Z. Xu, X. Yan, Z. K. Qin, and X. Y. Wang, "Optimization and analysis of series-coupled microring resonator arrays," Opt. Commun. **262**, 41-46 (2006).

139. H. C. v. d. Hulst, *Light scattering by small particles* (Dover Publications, Inc., New York, 1981).

140. Y. F. Yu, Y. H. Fu, X. M. Zhang, A. Q. Liu, T. Bourouina, T. Mei, Z. X. Shen, and D. P. Tsai, "Pure angular momentum generator using a ring resonator," Opt. Express **18**, 21651-21662 (2010).

141. S. Darmawan and M. K. Chin, "Critical coupling, oscillation, reflection, and transmission in optical waveguide-ring resonator systems," J. Opt. Soc. Am. B-Opt. Phys. **23**, 834-841 (2006).

142. S. G. Jennings, R. G. Pinnick, and J. B. Gillespie, "Relation between absorption coefficient and imaginary index of atmospheric aerosol constituents," Appl. Opt. **18**, 1368-1371 (1979).

143. W. H. P. Pernice, M. Li, and H. X. Tang, "Theoretical investigation of the transverse optical force between a silicon nanowire waveguide and a substrate," Opt. Express **17**, 1806-1816 (2009).

144. Z. Bor, K. Osvay, B. Racz, and G. Szabo, "Group refractive-index measurement by michelson interferometer," Opt. Commun. **78**, 109-112 (1990).

145. C. Xiong, W. H. P. Pernice, M. Li, and H. X. Tang, "High performance nanophotonic circuits based on partially buried horizontal slot waveguides," Opt. Express **18**, 20690-20698 (2010).